KEK Proceedings 2014-6
October 2014
R

# Proceedings of the Twenty-First EGS Users' Meeting in Japan

**August 4 - 5, 2014.**

**KEK, Tsukuba, Japan**

**Edited by**

**Y. Namito, H. Hirayama and S. Ban**

**High Energy Accelerator Research Organization**

**High Energy Accelerator Research Organization (KEK), 2014**

KEK Reports are available from:

High Energy Accelerator Research Organization (KEK)
1-1 Oho, Tsukuba-shi
Ibaraki-ken, 305-0801
JAPAN

Phone: +81-29-864-5137
Fax: +81-29-864-4604
E-mail: irdpub@mail.kek.jp
Internet: http://www.kek.jp

# FOREWARD

The Twenty-first EGS Users' Meeting in Japan was held at High Energy Accelerator Research Organization (KEK) from August 3 to 4. The meeting has been hosted by the Radiation Science Center. More than 100 participants attended the meeting.

The meeting was divided into two parts. Short course on EGS was held at the first half of the workshop using EGS5 code. In the later half, 10 talks related EGS were presented. The talk covered the wide fields, like the medical application and the calculation of various detector responses *etc.* These talks were very useful to exchange the information between the researchers in the different fields.

Finally, we would like to express our great appreciation to all authors who have prepared manuscript quickly for the publication of this proceedings.

Yoshihito Namito
Hideo Hirayama
Syuichi Ban
Radiation Science Center
KEK, High Energy Accelerator Research Organization

## CONTENTS

# The joint distribution of the angular and lateral deflections due to multiple Coulomb scattering with ionization loss

**K. Okei[†], T. Nakatsuka[‡] and Y. Kirihara[✠]**

[†]*Kawasaki Medical School, Kurashiki 701-0192, Japan*

[‡]*Okayama Shoka University, Okayama 700-8601, Japan*

[✠]*RIKEN Harima Institute, Sayo 679-5148, Japan*

**Abstract**

The joint probability density function $f(\theta_x, l_x)$ of the deflection angle $\theta_x$ and the lateral displacement $l_x$ with ionization loss under Molière's multiple Coulomb scattering theory is obtained using FFT (Fast Fourier Transform). The conditional distribution $f(l_x|\theta_x)$ obtained from the joint distribution is compared with that from the Monte Carlo method which has been developed by us and the distributions are validated each other.

## 1 Introduction

Molière's theory [1, 2, 3] is widely used in Monte Carlo codes such as EGS or GEANT3 [4, 5, 6] to simulate the multiple Coulomb scattering of high energy charged particles. However, because the joint probability density function of the deflection angle $\theta_x$ and the lateral displacement $l_x$ under the Molière theory is not known, the Monte Carlo particle transport step must be approximate.

To address this problem, we have developed the method to generate random deviates $\theta_x$ and $l_x$ which follow the joint distribution $f(\theta_x, l_x)$ under the ionization process [7]. This Monte Carlo sampling method gives better angular distribution than Molière's theory in the very small step size case [8]. We also have computed the FFT (Fast Fourier Transform) solution of $f(\theta_x, l_x)$ from its Fourier transform $\tilde{f}(\zeta, \eta)$ which can be obtained analytically [9, 10]. The FFT computed joint distribution can also be expressed in series expansion as same as the Molière angular distribution [11].

Since the numerical solution with FFT has been computed only under the fixed energy process so far, in this paper, we show the numerical joint distribution with ionization loss.

## 2 The joint distribution of the angular and lateral deflections

### 2.1 The Fourier transform of the joint distribution

If we assume continuous energy loss by ionization with a constant rate $\varepsilon$ per unit of radiation length, the incident charged particles of energy $E_0$ lose their energy as $E = E_0 - \Delta E = E_0 - \varepsilon t$ and the Fourier transform of the projected joint distribution $\tilde{f}$ is

$$\ln 2\pi\tilde{f}(\zeta,\eta) = \int_0^1 \frac{K^2 t(\zeta+\eta tu)^2}{4\Omega(E+\varepsilon tu)^2} \ln \frac{K^2(\zeta+\eta tu)^2}{4e^{\Omega}(E+\varepsilon tu)^2} \mathrm{d}u \tag{1}$$

where $t$ is the step size, $\zeta$ and $\eta$ are the Fourier variables corresponding to the deflection angle $\theta_x$ and the lateral displacement $l_x$ respectively, and $K$ and $\Omega$ are the scattering constants [12]. The integration (with the help of `Mathematica` [13]) gives us

$$
\begin{aligned}
\ln 2\pi\tilde{f}(\zeta,\eta) = \frac{K^2 t/(E_0 E)}{4\Omega(E_0-E)^3}\Bigg\{ & -2(E_0-E)(E\cdot\eta t-\zeta\cdot\varepsilon t)^2 \\
& -(E_0-E)(E\cdot\eta t-\zeta\cdot\varepsilon t)\left[E_0\zeta\ln\frac{K^2\zeta^2}{4e^{\Omega}E^2}-E(\eta t+\zeta)\ln\frac{K^2(\eta t+\zeta)^2}{4e^{\Omega}E_0^2}\right] \\
& -(E_0-E)E_0E\eta t\left[\zeta\ln\frac{K^2\zeta^2}{4e^{\Omega}E_0E}-(\eta t+\zeta)\ln\frac{K^2(\eta t+\zeta)^2}{4e^{\Omega}E_0E}+\frac{E_0+E}{E_0-E}\eta t\ln\frac{E_0}{E}\right] \\
& -E_0E\eta t(E\cdot\eta t-\zeta\cdot\varepsilon t)\left[\ln\frac{(E\cdot\eta t-\zeta\cdot\varepsilon t)^2}{E^2(\eta t)^2}\ln\frac{K^2\zeta^2}{4e^{\Omega}E_0E}-\ln\frac{(E\cdot\eta t-\zeta\cdot\varepsilon t)^2}{E_0^2(\eta t)^2}\ln\frac{K^2(\eta t+\zeta)^2}{4e^{\Omega}E_0E}\right. \\
& \left.-4\mathrm{Li}_2\left(-\frac{E_0-E}{E\cdot\eta t-\zeta\cdot\varepsilon t}\zeta\right)+4\mathrm{Li}_2\left(-\frac{E_0-E}{E\cdot\eta t-\zeta\cdot\varepsilon t}(\eta t+\zeta)\right)\right]\Bigg\} \qquad (2)
\end{aligned}
$$

where $\mathrm{Li}_2(z)$ denotes the dilogarithm function [14],

$$
\begin{aligned}
\mathrm{Li}_2(z) &= \sum_{k=1}^{\infty}\frac{z^k}{k^2} \\
&= -\int_0^z\frac{\log(1-t)}{t}\,\mathrm{d}t
\end{aligned}
$$

and we compute $\Re(\mathrm{Li}_2(z))$ in the case $z>1$.

### 2.2 The joint distribution

We used the FFTW library [15] to obtain the joint distribution $f(\theta_x, l_x)$ from its Fourier transform $\tilde{f}(\zeta,\eta)$. Figure 1 shows the contour plots of the joint distribution calculated for 200 MeV electrons incident on iron for $\Delta E/E_0 = 0.1$ (top), 0.5 (middle), and 0.9 (bottom). To see the transition of the distribution shape according to the energy loss, $\theta_x$ is scaled by the Molière's scaling angle $\theta_{\mathrm{M},0} = \chi_c\sqrt{B}$ calculated with the initial energy $E_0$ ($\chi_c$ and $B$ have their usual meaning) and $l_x$ is scaled by $\theta_{\mathrm{M},0}t/\sqrt{3}$. We can see that the distribution getting broader as $\Delta E$ becomes large, but the broadening of $l_x$ distribution is relatively smaller than that of $\theta_x$ distribution.

The conditional distributions of $l_x$ given some $\theta_x$s obtained from the FFT and from our Monte Carlo method [7] are compared in figure 2. It is seen that the agreement of all the distributions is very well.

## 3 Summary

The joint probability density function of the deflection angle and the lateral displacement with ionization loss under Molière's multiple Coulomb scattering theory is computed using FFT. The distributions obtained from FFT and from the Monte Carlo method agree very well and the validity of both the FFT and Monte Carlo methods is confirmed. The numerical solution would be useful to test Monte Carlo transport algorithms or to determine suitable parameters of simulations.

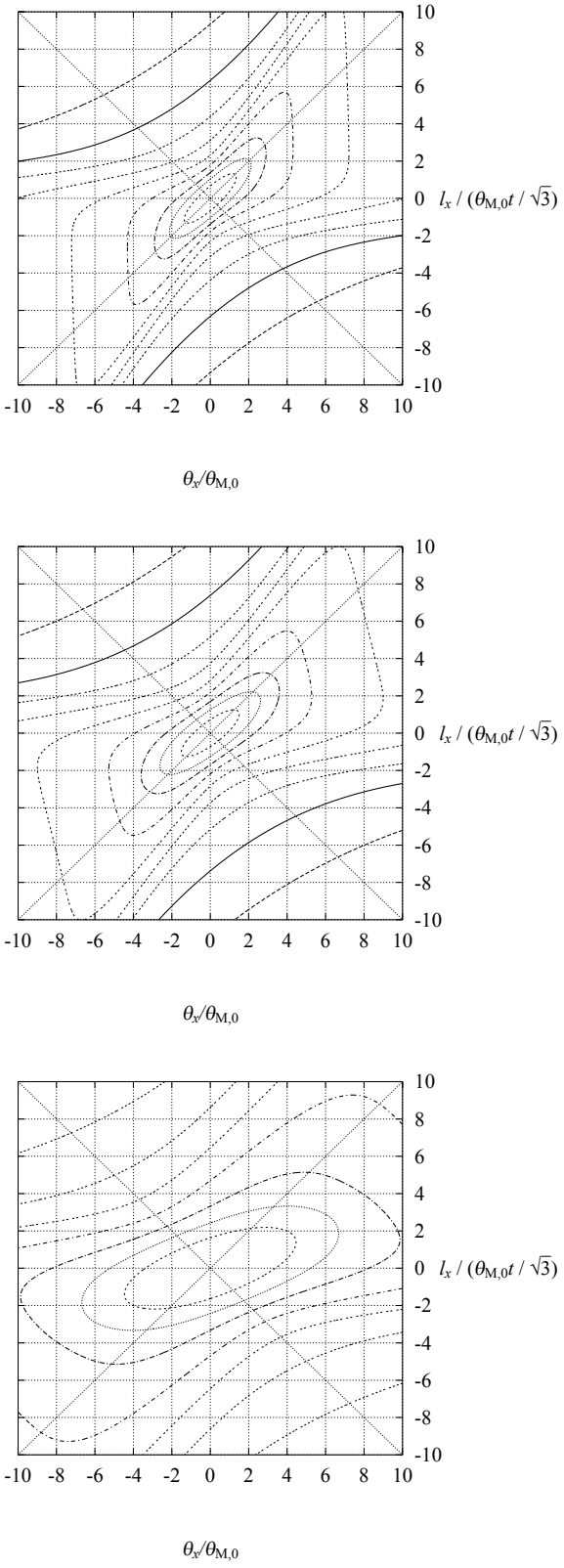


Figure 1: The joint distribution for $\Delta E/E_0 = 0.1$ (top), 0.5 (middle), and 0.9 (bottom).

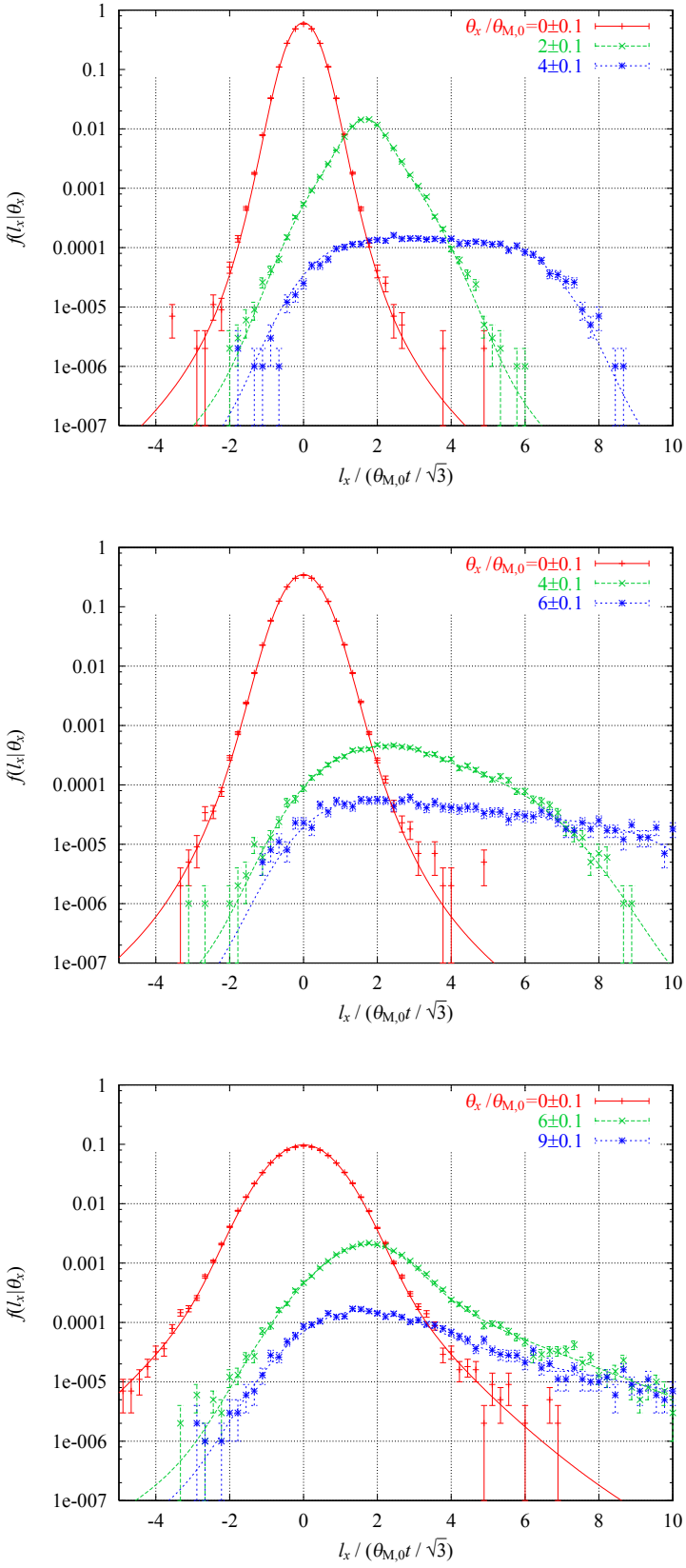


Figure 2: The conditional distribution of $l_x$ given $\theta_x$ for $\Delta E/E_0 = 0.1$ (top), 0.5 (middle), and 0.9 (bottom).

## References


[1] G. Molière, Z. Naturforsch. **2a**, 133 (1947).

[2] G. Molière, Z. Naturforsch. **3a**, 78 (1948).

[3] H.A. Bethe, Phys. Rev. **89**, 1256 (1953).

[4] W. R. Nelson, H. Hirayama, and D. W. O. Rogers., *SLAC-265*, (1985)

[5] H. Hirayama et al., *SLAC-R-730*, (2005)

[6] GEANT Detector Description and Simulation Tool, CERN Program Library Long Writeup, PHYS325 (1993).

[7] K. Okei and T. Nakatsuka, *Proc. 3rd International Workshop on EGS*, KEK Proceedings 2005-7, 57 (2005).

[8] K. Okei, T. Nakatsuka, and N. Takahashi, *Proc. 13th EGS Users' Meeting in Japan*, KEK Proceedings 2006-4, 28 (2006).

[9] T. Nakatsuka, K. Okei and N. Takahashi, *Proc. 13th EGS Users' Meeting in Japan*, KEK Proceedings 2006-4, 18 (2006).

[10] K. Okei and T. Nakatsuka, *Proc. 14th EGS Users' Meeting in Japan*, KEK Proceedings 2007-5, 26 (2007).

[11] T. Nakatsuka and K. Okei, *Proc. 15th EGS Users' Meeting in Japan*, KEK Proceedings 2008-7, 1 (2008).

[12] T. Nakatsuka and J. Nishimura, *Phys. Rev.* E **78**, (2008) 021136

[13] `http://www.wolfram.com/`

[14] `http://en.wikipedia.org/wiki/Spence's_function`

[15] `http://www.fftw.org/`

# Relationship between electron-beam spot size and X-ray spot size in transmission X-ray source

**Junichiro Tottori**

*Core Technology Division, Nikon Corporation, Kanagawa, 244-8533, Japan*
*e-mail: Junichiro.Tottori@nikon.com*

**Abstract**

A relationship between electron-beam spot size and X-ray spot size was calculated using Electron-Gamma Shower 5 (EGS5). A linear relationship between electron beam's diameter and X-ray's one was obtained in EGS5 simulation. Furthermore, ratios of diameter (X-ray / Electron beam) of simulations were compared with those of experiments and it was found that the ratios of EGS5's results are similar to ones of the experimental results.

## 1. Introduction

There are some methods to make X-ray transmission image blur small in X-ray apparatus. One of the methods is to make a spot size of the X-ray source small. In this method, the spot size is determined by electron beam, because X-ray is generated by incident electron beam in a heavy metal. Incident electrons are scattered in the heavy metal, therefore the spot size of X-ray is not equal to that of electron beam. The purpose of this study is to clarify the relationship between electron-beam spot size and X-ray spot size.

## 2. Numerical Simulation

### 2.1 Calculation model using EGS5

Electron beam is focused on a tungsten target, X-ray is generated in the target, and X-ray through the target is detected at detector plane 1 (Figure1). The detector plane is placed at 1 mm from an incident surface of the target. A spatial profile of electron beam at the surface is Gaussian profile and a half angle of the focused electron beam is 30 mrad. There are two variables in this model. The first is Full Width of Half Maximum (FWHM) of Gaussian profile, it has three values: 0.1, 0.2, and 0.3 μm. The second is an accelerating voltage it has four values: 30, 60, 120, and 160 kV. We chose these parameters individually, focused electron beam on the target, and recorded transmitted X-ray's data (energy, position, direction cosine, and so on) at the plane. Calculation options in this model are shown in Table 1. A significant option is *ibrdst*. This option determines about a scattering angle of bremsstrahlung. Where ibrdst = 0, it is fixed at a constant value, otherwise ibrdst = 1, it is sampled in a calculation.

### 2.2 Calculation of Line Spread Function (LSF)

To verify our calculation as more reliable, we estimated X-ray blur by using two methods, one is knife edge method and the other is source image method.

2-2-1. Method A: Calculation edge profile

The source blur was calculated using the knife edge image. Figure 2 shows numerical set up of the calculation. Electron beam is focused on the target and the transmitted X-ray is propagated to a detector plane 2. There is a knife edge between the target and the detector plane 2 to block a part of the transmitted X-ray. The knife edge and the detector plane 2 are placed at 1 mm and at 700 mm from incident surface of the target, respectively. The transmitted X-ray's data was obtained in 2.1. A propagation equation is

$$\begin{pmatrix} x' \\ y' \\ z' \end{pmatrix} = \begin{pmatrix} x \\ y \\ z \end{pmatrix} + \frac{d}{w} \begin{pmatrix} u \\ v \\ w \end{pmatrix} . \qquad \text{eq.1}$$

Where ($x'$, $y'$, $z'$) is an X-ray position after propagation, ($x$, $y$, $z$) is an X-ray position at the detector plane 1, ($u$, $v$, $w$) is a direction cosine of X-ray at the detector plane 1, and $d$ is a z element of a propagation distance. We calculate X-ray intensity profile at the detector plane 2.

2-2-2. Method B: Calculation source image

A calculation model of the method B is shown in Figure 3. The detector plane 1 is placed at 1 mm from the target. X-ray is propagated from the detector plane 1 back to the target and we calculated an intensity profile (x-y plane) at $z = z_0$. We integrated the intensity profile of $z_0$ plane along y-direction. We stored the integrated profiles along z axis and compared FWHMs of the profiles at each z plane. Finally, we obtained the LSF which has the smallest FWHM.

## 2.3 Numerical results

Calculation results of method A is shown in Figure 4. In Figure 4, the voltage is 120 kV and the FWHM of electron beam is 0.2 μm. In Figure 4, x values are reduced to 1 / 700 for expressing the blur at the target surface. Three lines are plotted in Figure 4, a solid line is a normalized intensity, a dashed line is a fitting curve of the solid line, and a dashed-dotted line is the LSF. A fitting function is

$$I = \sum_{i=1}^{3} w_i(x) \frac{A_i}{2} erfc\left(x / \sqrt{2}\sigma_i\right) + I_0 . \qquad \text{eq.2}$$

Where $w_i$ is a weight function, $A_i$ is an amplitude, $\sigma_i$ is a standard deviation, $I_0$ is an offset, and

$$erfc(x) = \frac{2}{\sqrt{\pi}} \int_x^{\infty} e^{-t^2} dt . \qquad \text{eq.3}$$

After the fitting, we calculate the LSF with

$$\mathrm{LSF} = \sum_{i=1}^{3} \frac{A_i}{\sqrt{2\pi}\sigma_i} e^{-\frac{x^2}{2\sigma_i^2}} . \qquad \text{eq.4}$$

In this paper, the X-ray's diameter is defined as the FWHM of the LSF. In Figure 4, the diameter is 0.31 μm.

Figure 5(a) shows a LSF map near the incident surface calculated with method B. A vertical coordinate of Figure 5(a) is a depth from the surface and a color bar means normalized intensity values of X-ray; a high intensity is a light color and a low intensity is a dark one. Numerical conditions (the accelerating voltage and the FWHM of the electron beam) are same as Figure 4. In Figure 5(a), an area of high intensity and narrow bandwidth exists near the incident surface. A LSF at the surface is shown in Figure 5(b) and its diameter is 0.30 μm.

Figure 6 shows a comparison of the results of the method A with that of the method B. In Figure 6, solid lines mean the results of method A, and dashed ones mean those of method B. FWHMs of X-ray LSF in method A are same as those in method B. The numerical result is reasonable because both method A and B show same result. FWHM relationship between X-ray and electron beam is shown in Figure 7. In Figure 7, X-ray FWHMs and electron-beam FWHMs lie in a straight line at each accelerating voltage. Therefore, it shows linear relationships between X-ray

FWHM and electron-beam FWHM.

# 3. Experiments

## 3.1 Experimental set up

We examined the accuracy of numerical results by experiments. The experimental set up is shown in Figure 8(a), where $l_a$ is a length from the electron beam's incident surface to a Line and Space chart and $l_b$ is a length from the surface to a flat panel detector. X-ray from a source propagates to the chart. The chart has three rectangle slits along y direction, and the slit size is 5 μm × 25 μm. X-ray through the chart is detected at the flat panel detector. In Figure 8(a), a ratio of $l_b$ divided by $l_a$ is 2000, therefore the chart is imaged 2000 times at the detector.

## 3.2 Calculation LSF from experimental results

The LSF was calculated using a detected X-ray image. A calculation area which is shown in Figure 8(b) was set in the image, and we integrated the intensity profile along y-direction. The intensity profile of the image is shown in Figure 9, a lateral coordinate of Figure 9 is reduced to 1 / 2000 for expressing the image in the chart scale. In Figure 9, a solid line is normalized calculation intensity, and a dashed line is fitting curve of the solid line. A fitting function is

$$I = \frac{1}{2}\sum_{j=-1}^{j=1}\sum_{i=1}^{i=3} w_i(x)A_i\left\{-erfc\left(\frac{1}{\sqrt{2}\sigma_i}\left((x-2aj)+\frac{a}{2}\right)\right)+erfc\left(\frac{1}{\sqrt{2}\sigma_i}\left((x-2aj)-\frac{a}{2}\right)\right)\right\}+I_0 . \quad \text{eq.5}$$

Where $a$ is a line width and other parameters are same as eq.2. The LSF was calculated with eq.4. Figure 10 is the LSF of Figure 9. In Figure 10, the higher the voltage is, the larger a skirt of the LSF is.

## 3.3 Comparison of simulations with experiments

Ratios of the FWHMs are shown in Figure 11. The ratio is a value that the X-ray FWHM is divided by the electron-beam FWHM. Although the ratios of the simulation are a little smaller than the experimental one in each voltage, the simulation results have same behaver as the experimental ones. The ratio is almost constant when the accelerating voltage is more than a certain voltage (In Figure 11. it is about 80 kV.), and the ratio decreases below the voltage.

# 4. Conclusions

It was obtained that there are the linear relationships between the electron-beam diameter and the transmitted X-ray one, and these relationships are not changed in the range of voltages we used. The diameter's ratios of electron beam and the X-ray calculated using EGS5 are similar to the experimental results.

# Acknowledge

We are deeply grateful to Ph.D. Hirayama (KEK). His advice and comments has been a great help in our simulation.

# References

1) H. Hirayama, Y. Namito, A. F. Bielajew, S. J. Wilderman, and W. R. Nelson, "THE EGS5 CODE SYSTEM", SLAC-R-730 (2005).

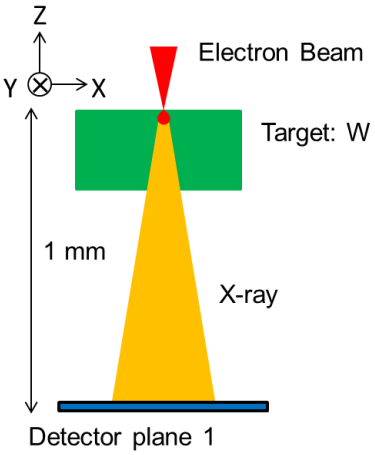


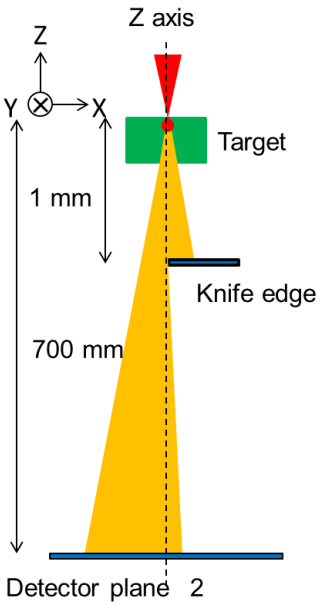


**Figure 1.** Calculation model in EGS5. **Figure 2.** Calculation model of method A.

**Table 1.** Calculation options in EGS5

| EGS5 options | PEGS options |
|---|---|
| iphter = 1 | irayl = 1 |
| iedgefl = 1 | ibound = 1 |
| iauger = 1 | incoh = 1 |
| iraylr = 1 | icprof = -3 |
| ipolar = 1 | impact = 6 |
| inchor = 1 | ae = 0.521 |
| iprofr = 1 | ue = 0.001 |
| inpacr = 1 | ap = 20.521 |
| ibrdst = 1 | up = 20.000 |

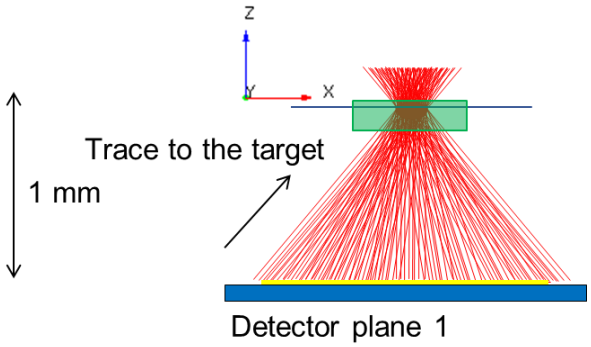


**Figure 3.** Calculation model in method B.

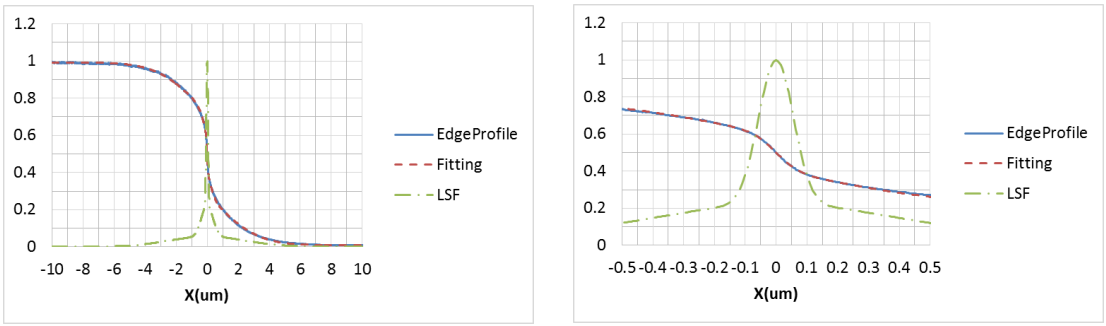


**(A)** **(B)**

**Figure 4.** Numerical results of method A.
(A) Intensity profile and LSF in wide range (-10 μm to 10 μm).
(B) Intensity profile and LSF in narrow range (-0.5 μm to 0.5 μm).

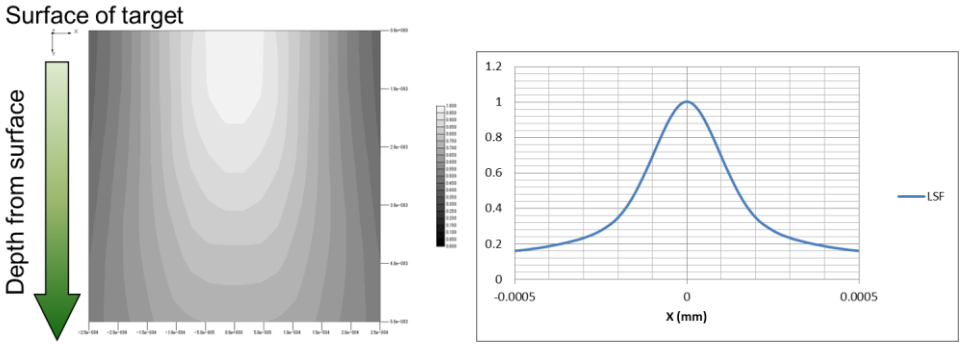


**Figure 5.** Numerical results of method B.
(a) LSF map about depth of the target. (b) LSF of the surface.

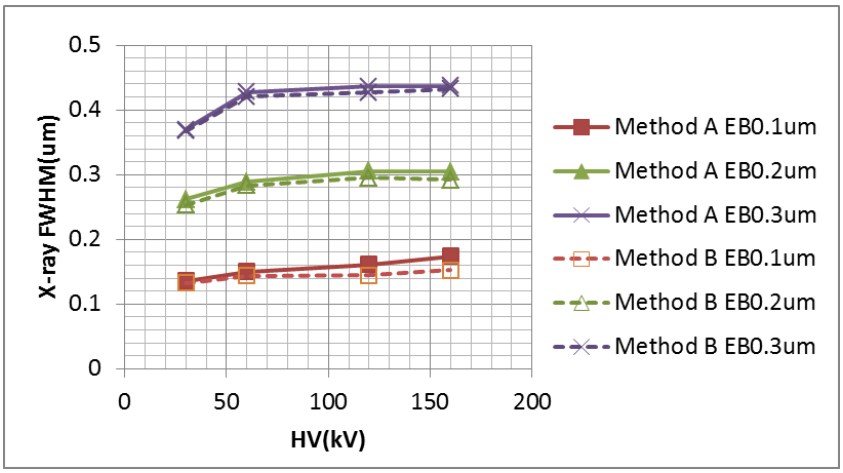


**Figure 6.** Numerical results of method A and B.

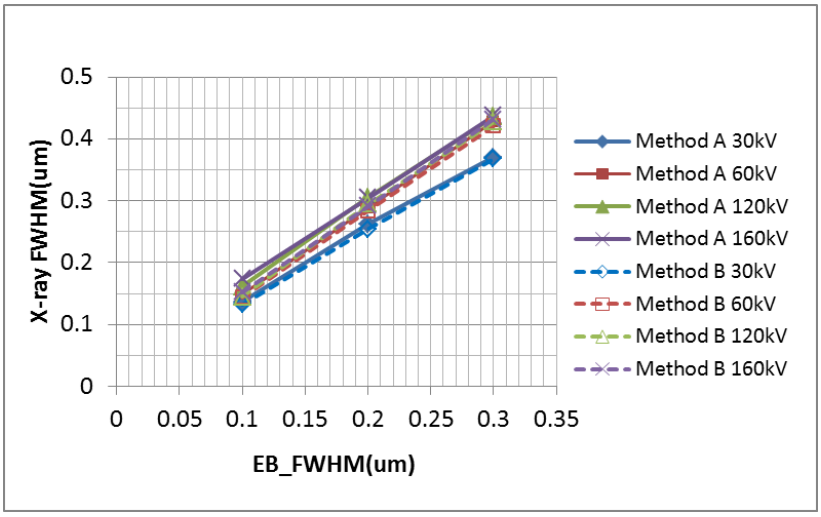


**Figure 7.** Comparison among FWHM, X-ray and electron beam.

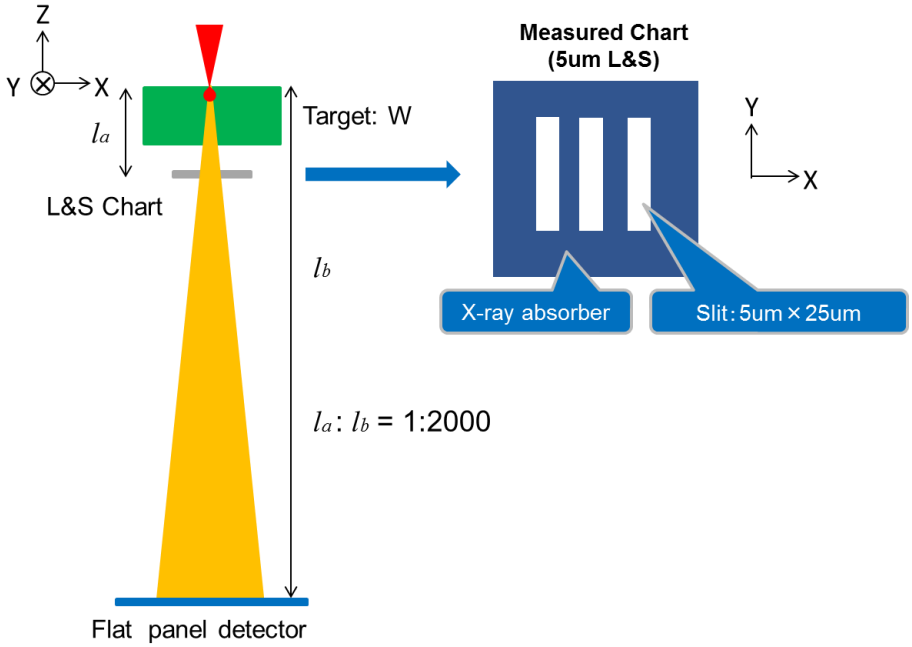


**Figure 8(a).** Experimental set up.

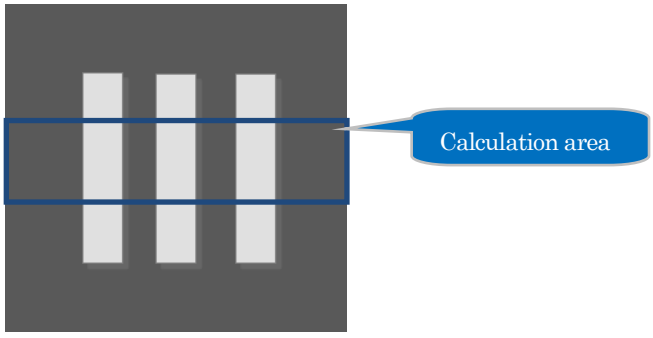


**Figure 8(b).** X-ray image and Calculation area

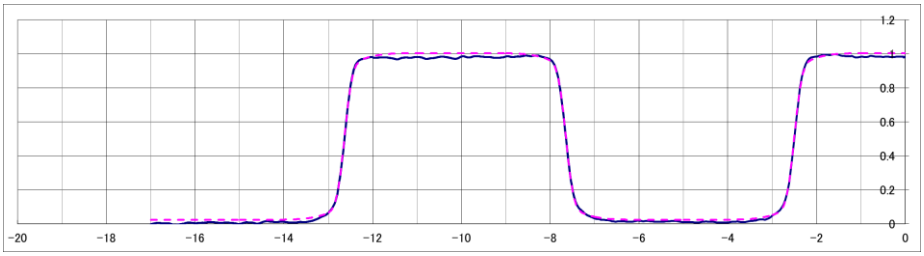


(a)

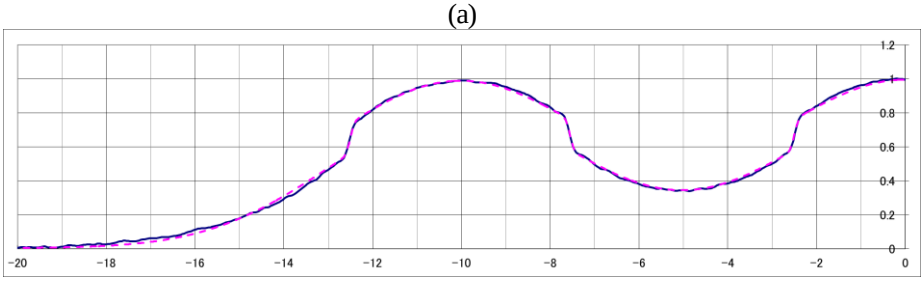


(b)

**Figure 9.** Experimental results. Intensity profile (a) 30 kV, (b) 120 kV.

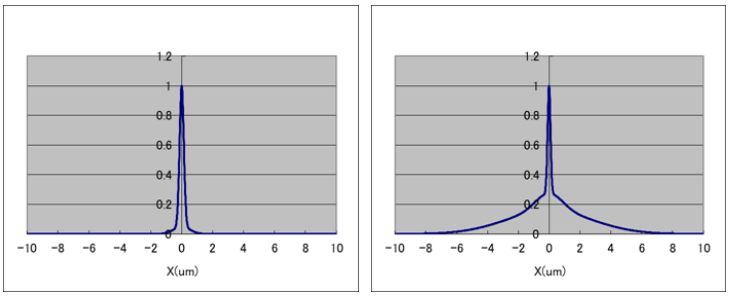


**Figure 10.** LSF of Figure 8. (a) 30 kV, (b) 120 kV.

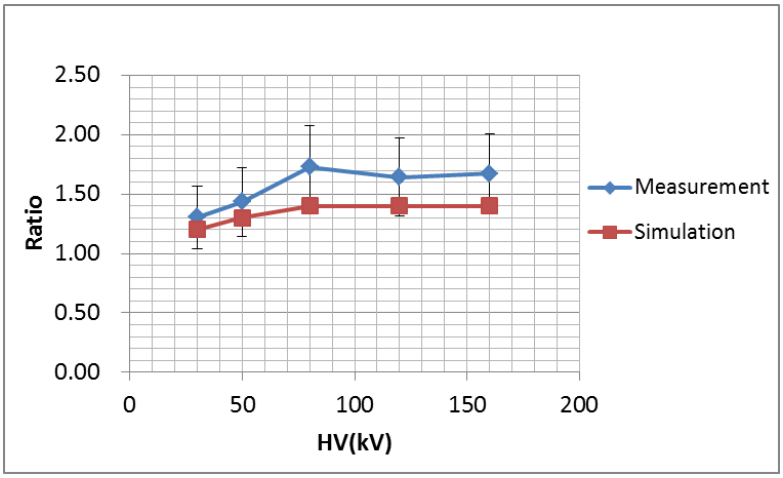


**Figure 11.** Ratio of FWHMs (X-ray / Electron beam).

# AN EXAMINATION OF DIFFERENCES IN ABSORBED DOSE PROFILE BETWEEN MEASUREMENT AND CALCULATION IN X-RAY COMPUTED TOMOGRAPHY

**M. Inoue[1], S. Koyama[2], N. Kakuta[3], and T. Haba[4]**

*[1]Department of Radiological Technology, Graduate School of Medicine, Nagoya University*
*1-1-20 Daiko-Minami, Higashi-ku, Nagoya 461-8673, Japan*
*[2]Brain & Mind Research Center*
*1-1-20 Daiko-Minami, Higashi-ku, Nagoya 461-8673, Japan*
*[3]Department of Radiological Technology, School of Health Science, Nagoya University*
*1-1-20 Daiko-Minami, Higashi-ku, Nagoya 461-8673, Japan*
*[4]Radiology and Radiation Oncology, Fujita Health University Hospital*
*1-98 Dengakugakubo, Kutsukake-cho, Toyoake, Aichi 470-1192, Japan*
*e-mail: inoue.masaki@a.mbox.nagoya-u.ac.jp*

**Abstract**

Multidetector X-ray computed tomography technology is developing rapidly. As the number of detectors increases, the spread of the X-ray beam width along the rotation axis increases. In our previous measurement and calculation using the Electron Gamma Shower ver. 5 Monte Carlo simulation, the maximum absorbed dose position shifted from the surface to a deeper region in a cylindrical poly(methyl methacrylate) phantom as the X-ray beam width spread. However, there were some differences between the measurement and the calculation. In this study, we focus on the X-ray tube angle and examine these differences. The results indicate that the form of the absorbed dose profile varied greatly and the maximum dose position changed if the initial irradiation angle of the X-ray tube changed.

## 1. Introduction

The computed tomography dose index (CTDI) is generally used to evaluate the radiation dose in X-ray computed tomography (CT). The radiation doses are measured at the periphery (3, 6, 9, and 12 o'clock positions) and the center of a cylindrical poly(methyl methacrylate) phantom using a CT ionization chamber 100 mm in length inserted into the phantom; the results are denoted by $CTDI_{100,p}$ and $CTDI_{100,c}$ respectively. The absorbed dose is usually highest at the surface of the phantom and the lowest at its center. An index called the weighted CTDI ($CTDI_w$), which represents a mean dose in the phantom, is derived by multiplying a factor that considers the form of the absorbed dose profile.

Our previous research using the Electron Gamma Shower ver. 5 (EGS5) Monte Carlo simulation revealed that the maximum dose position shifted from the phantom surface to a deeper region in several X-ray CT units [1]. Then, we measured the absorbed dose profile using a water phantom developed by hollowing an expanded polystyrene cuboid and inserting a small photodiode dosimeter. We found that the maximum dose position shifted from the phantom surface, as is evident in the calculation result. However, there were some differences between the measured and calculated results. Therefore, in this study, we establish the cause of the differences using EGS5.

To examine the differences, we focus on the differences in the initial irradiation angle of the X-ray tube. In a clinical X-ray CT examination, the X-ray tube starts rotating before irradiation and irradiates a patient when an irradiation-button is pushed. In non-helical CT scanning, the initial irradiation angle of the X-ray tube is constant and does not affect the absorbed dose profile. In helical scanning, the CT bed moves along the rotation axis depending on the helical pitch, which is a factor obtained by dividing the bet moving by the beam width. Because the incident angle of X-rays at a longitudinal position of the detector varies with the initial irradiation angle of the X-ray tube as the helical pitch increases, the absorbed dose profile is seriously affected by the initial irradiation angle of the X-ray tube. In this study, we therefore examine the effects of the initial irradiation angle of the X-ray tube on the dose profile using the EGS5 Monte Carlo simulation.

## 2. Materials and Methods

### 2.1 Previous measurement and simulation of the absorbed dose profile

First, we developed a cylindrical water phantom of polystyrene foam, as shown in Fig. 1(a). We measured the absorbed dose profile by filling the cylindrical part of this phantom with water, sinking a small photodiode dosimeter, and scanning this phantom with a CT scanner (Aquilion 64, Toshiba Medical Systems Corporation, Tochigi, Japan) using the general parameters for clinical abdominal examination (tube voltage of 120 kV, tube current of 200 mA). We used a photodiode dosimeter [Fig. 1(b)] that was developed in our previous research. This semiconductor dosimeter consists of a set of pin silicon photodiodes bonded back-to-back that have a sensitive area of $2.8 \times 2.8$ mm$^2$. Thus, the angular dependence of the dosimeter is dramatically reduced [2]. The scan range of this measurement was set to 100 mm. Because we cannot set the helical pitch to 1.0 in the Aquilion 64 CT scanner, we chose a set of parameters that is closest to a helical pitch of 1.0 (helical pitch of 0.938, beam width of 16 mm).

The calculation was performed using the EGS5 Monte Carlo simulation. The simulation incorporated a geometry that imitated the water phantom used for the measurement and the changes in the energy spectra and dose profiles of the X-ray fan beam due to the beam-shaping filter. The scanning parameters, e.g., the tube voltage, helical pitch, and scan range, were set as in the measurement.

### 2.2 Examination of variation in absorbed dose profile

In helical scanning, because the initial irradiation angle of the X-ray tube is different for each examination, the incident angle at the location of the dosimeter in the phantom also changes. In the measurement, it is difficult to examine the difference in the dose profile using the effect of the initial irradiation angle of the X-ray tube. We therefore examine it using the EGS5 Monte Carlo simulation.

The geometry and fan beam data used for the previous research were incorporated into the simulation. We acquired dose profiles at the initial irradiation angles at 45° intervals starting at 0°. Moreover, to examine the difference in the effect of the initial irradiation angle depending on the helical pitch, we acquired dose profiles at initial irradiation angles of 0°, 90°, 180°, and 270° with helical pitches of 0.5, 0.938, and 2.0.

## 3. Results

### 3.1 Absorbed dose profiles acquired by measurement and calculation

Figure 2 shows the measured and calculated relative absorbed dose profiles. In the measured profile, the maximum absorbed dose position shifted approximately 8 mm from the phantom surface to a deeper region, and the maximum absorbed dose was 7.3% greater than the absorbed dose at the phantom surface. In the calculated profile, however, the maximum absorbed dose position shifted approximately 12 mm from the phantom surface to a deeper

region, and the maximum absorbed dose was 12% greater than the absorbed dose at the phantom surface. Thus, there are some differences between the measured and calculated absorbed dose profiles.

### 3.2 Variation in absorbed dose profile due to differences in the initial irradiation angle of the X-ray tube

Figure 3 shows the relative absorbed dose profile acquired at 15° intervals starting at 0° with a helical pitch of 0.938. This graph indicates that the maximum absorbed dose and maximum absorbed dose position varied greatly with the initial irradiation angle of the X-ray tube. Figure 4 shows the relative absorbed dose profile acquired at 0°, 90°, 180°, and 270° with helical pitches of 0.5, 0.938, and 2.0. This graph indicates that the form of the absorbed dose profile underwent greater changes in the phantom periphery as the helical pitch increased.

## 4. Discussion

The results of this study revealed that the initial irradiation angle markedly affects the maximum absorbed dose position and the symmetry of the absorbed dose profile. The range of the incident angle at the longitudinal position of the dosimeter changes because the CT bed moves more rapidly as the helical pitch increases. Therefore, it was indicated that the initial irradiation angle of the X-ray tube has a greater effect as the helical pitch increases.

The American Association of Physicists in Medicine Task Group 111 (AAPM TG111) recommended that, to reduce the variation in the dose profile at the periphery of a phantom in CTDI measurements, the helical pitch should be set to $p$, which is given by

$$p \leq l/2nT,$$

where $l$ is the longitudinal length of the dosimeter, and $nT$ is the beam width along the rotation axis [3]. In this study, however, we used a small photodiode dosimeter to acquire the maximum absorbed dose position in detail, and we set the helical pitch to 0.938 to reproduce a CTDI measurement using a CT ionization chamber. In our previous measurement, therefore, it is thought that a large variation in the absorbed dose profile at the periphery of the phantom appeared.

Owing to the abovementioned reasons, in the measurement of dose profiles in X-ray CT, it is important that the dosimeter and helical pitch are chosen carefully according to the purpose of the measurement, and the variation in the dose profiles at the periphery of the phantom are evaluated adequately using a Monte Carlo simulation.

## 5. Conclusions

The variation in the absorbed dose profile due to differences in the initial irradiation angle of the X-ray tube was evaluated using EGS5. The form of the absorbed dose profile was found to vary greatly depending on the initial irradiation angle and helical pitch. It is important that the dosimeter and helical pitch are chosen carefully according to the purpose of the measurement.

## References

1) Tomonobu H, Shuji K, Yoshihiro I. Influence of difference in cross-sectional dose profile in a CTDI phantom on X-ray CT dose estimation: a Monte Carlo study. Radiol Phys Technol 2014; 7: 133-140.

2) Takahiko A, Shuji K, Chiyo K. An in-phantom dosimetry system using pin silicon photodiode radiation sensors for measuring organ doses in x-ray CT and other diagnostic radiology, Medical Physics 2002; 29(7): 1504-1510.
3) AAPM REPORT NO.111 Comprehensive Methodology for the Evaluation of Radiation Dose in X-ray Computed Tomography. February 2010

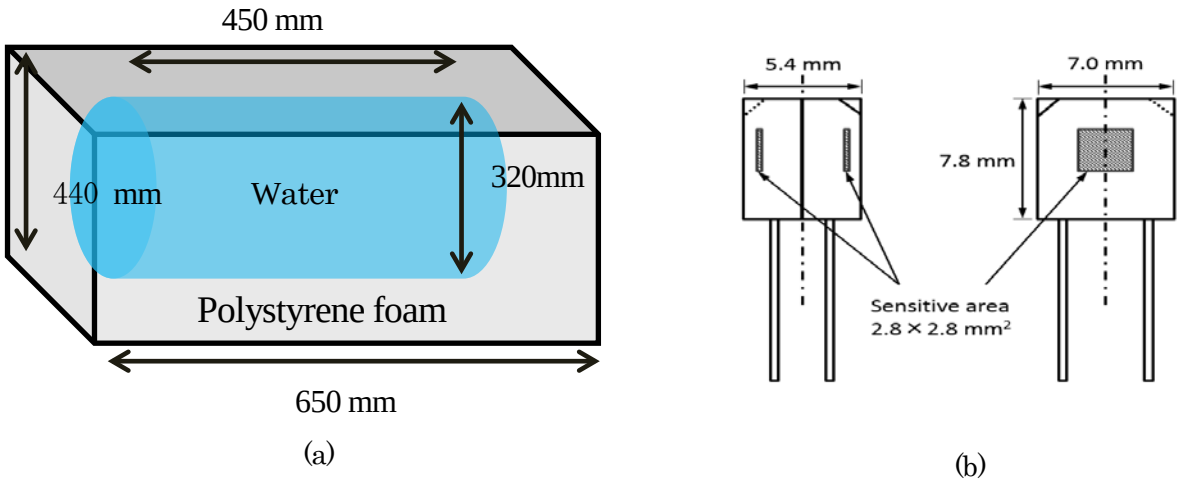


**Figure 1.** The cylindrical water phantom (a) and the photodiode dosimeter we used(b)

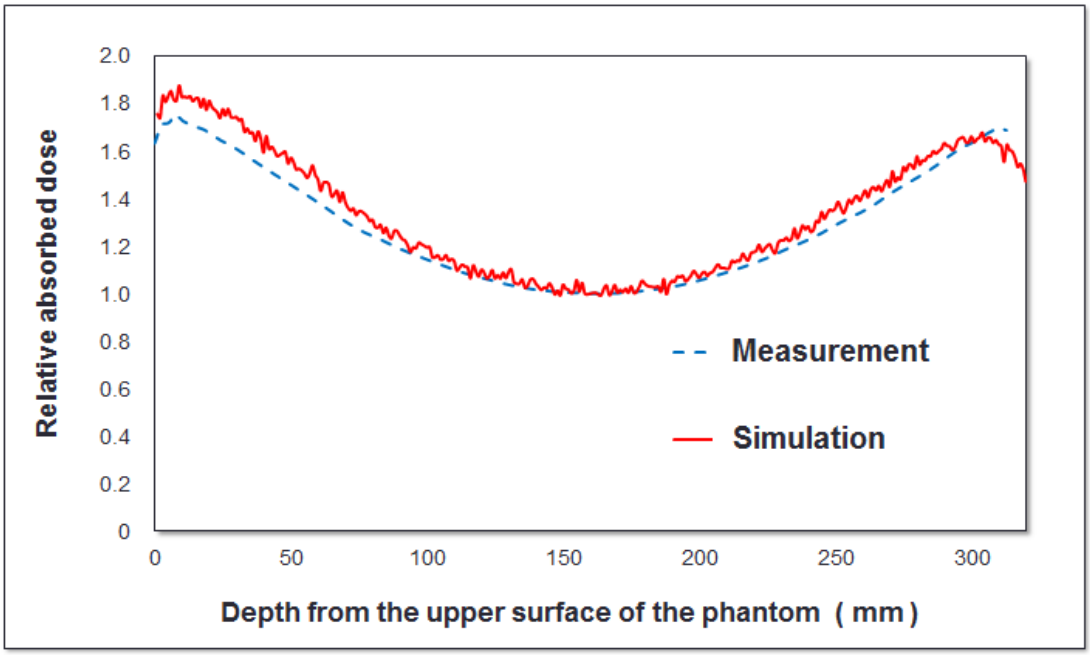


**Figure 2.** The measured and calculated relative absorbed dose profile

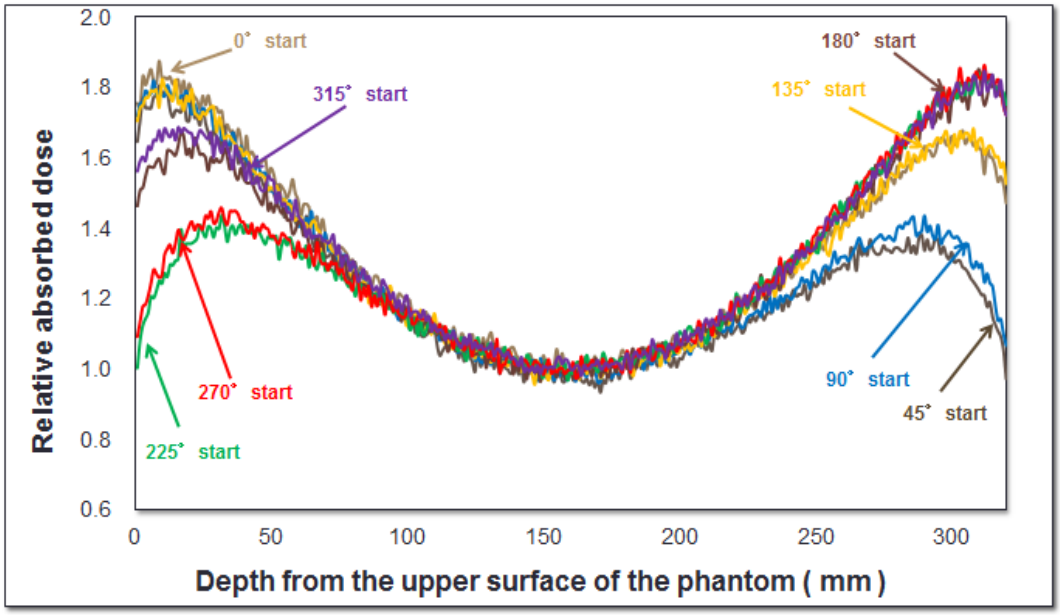


**Figure 3.** The relative absorbed dose profile acquired at 15° intervals starting at 0° with a helical pitch of 0.938

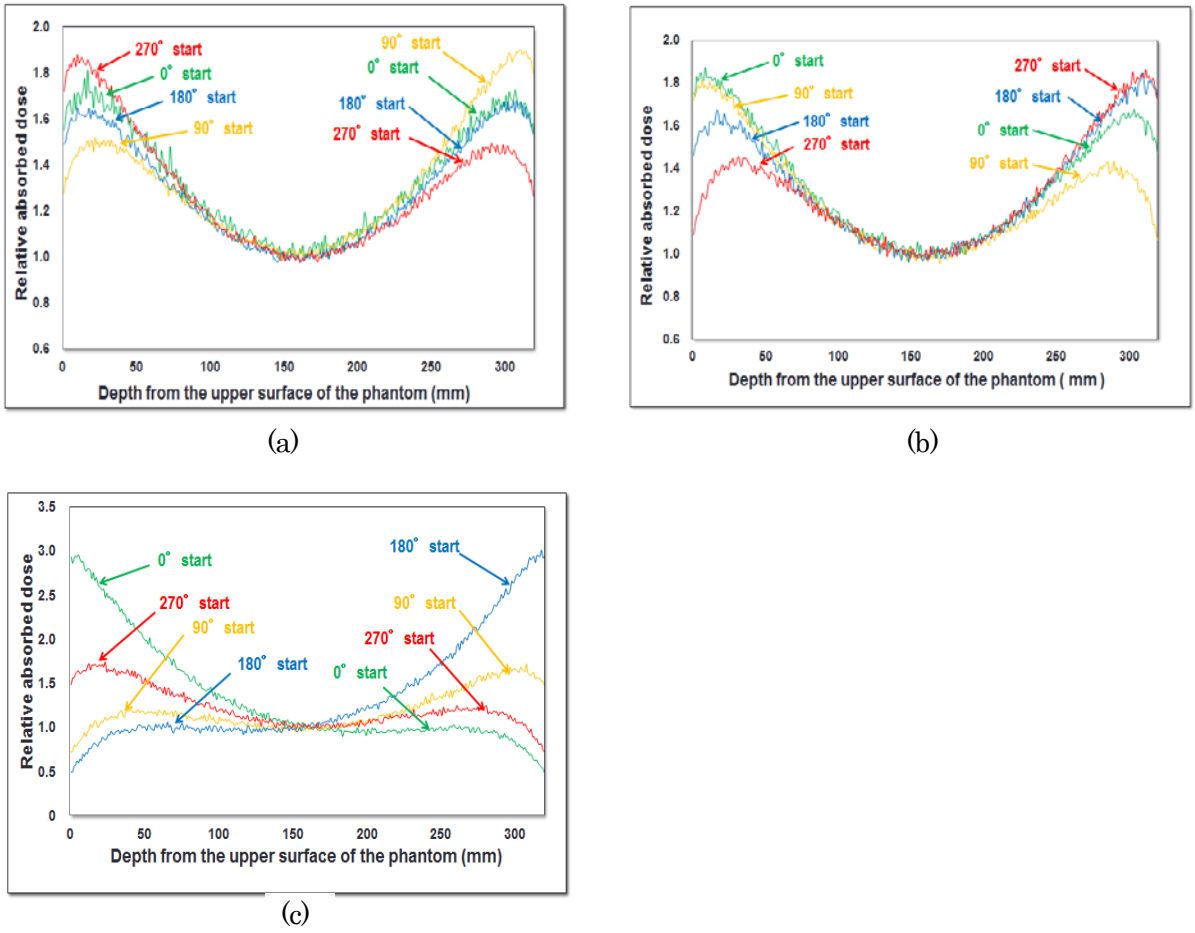


**Figure 4.** The relative absorbed dose profile acquired at 0°, 90°, 180°, and 270° with a helical pitch of 0.5(a), 0.938(b), and 2.0(c)

# THE BENCHMARK TEST OF A SIMULATION CODE FOR EPID IMAGE CONTRAST IMPROVEMENT USING EGS5

**Masatsugu Hariu, Atsushi Myojoyama and Hidetoshi Saitoh**

*Graduate School of Human Health Sciences, Tokyo Metropolitan University,*
*Tokyo, 116-8551, Japan*

**Abstract**

For patient setup of IGRT technique, a MV planar image is compared with a DRR. Then, displacement of patient position will be estimated and set up error will be modified. In case of therapeutic beam, Compton scattering is the main interaction within patient. Therefore, image contrast of the EPID is deteriorated by scattered photon. The MC simulation is quite useful to investigate the behavior of scattered photons within each patient. However, a general purpose MC simulation is time-consuming. Therefore, an original simple MC code, which focused on the Compton interaction, was developed to reduce the processing time. Additionally, an image-processing program was developed to improve image contrast. By using this program, the contribution of scattered photons was cancelled and these scattered photons reused as primary photons on the assumption that Compton scattering did not take place. As a result, usability of proposed contrast improvement was clarified. Furthermore, reliability of the simple MC code was evaluated by the benchmark test using the EGS5.

## 1. Introduction

Image-guided radiation therapy (IGRT) is defined as external beam radiation therapy with positional verification using imaging prior to each treatment fraction [1]. The purpose of IGRT is to help minimize the planning target volume (PTV) margins by reducing the uncertainty in tumor target localization, and to deliver the prescribed dose distribution as accurately as possible [2]. For patient setup of IGRT, a megavoltage (MV) planar image is compared with a digitally reconstructed radiography (DRR). Then, displacement of patient position will be estimated and set up error will be modified. DRR is a reference image produced by tracking beam lines from a virtual source position through the CT data of the patient. On the other hand, a MV planar image using therapeutic beam is acquired by an electronic portal imaging device (EPID) before the dose delivery.

In case of therapeutic beam, contrast of the MV planar image is deteriorated because Compton scattering is dominant within patient and Compton scattered photons impinged on the EPID. Therefore, improvement of contrast can be expected by cancelling the contribution of Compton scattered photons.

The Monte Carlo (MC) simulation is quite useful to investigate the behavior of scattered photons. However, a general purpose MC code is time-consuming for each patient in clinical practice.

In this report, a simple MC code, which focused on the Compton interaction, was developed to reduce the processing time. Improvement of the image contrast was attempted by cancelation of scattered photon's contribution and forecasting of primary photon's contribution. And reliability of the computational algorithm of the simple MC code was confirmed by the benchmark test using the EGS5 [3].

# 2. Materials and Methods

## 2.1 Equipment and Development environment

The EPID (Portal Vision a-S500 on Clinac 21 EX, Varian medical system) was modeled for the simple MC simulation. Fig. 1 shows external view of a Clinac 21EX and EPID and Fig. 2 shows structural drawing of EPID (a-S500). The EPID is composed of 1 mm thick copper plate, 0.4 mm thick terbium-doped gadolinium oxysulfide ($Gd_2O_2S$:Tb) scintillator which converts incident into green light and 1.4 μm amorphous silicon (a-Si) photodiode which converts green light into an electric charge. The matrix of sensitive area is 512 pixel × 384 pixel and each pixel size is 0.784 mm × 0.784 mm.

The simple MC code and image-processing program were developed by Qt 5.2.1 application. Qt programing environment was programed with C++ and several other programming languages can be combined by the "language bindings".

Fig. 1 External view of the Clinac 21EX and EPID

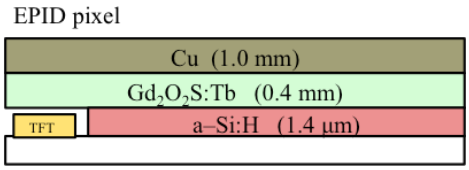


Fig. 2 Structural drawing of EPID's major components

## 2.2 Photon sampling in the MC simulation

The simple MC code was developed to simulate Compton interaction within voxels reconstructed from 3D-CT image. Fig. 3 shows three-dimensional drawing for the photon sampling. In this report, the chest phantom (N-1 LUNGMAN, Kyoto kagaku) was modeled. Geometry of the simulation was the same conditions as actual MV planar imaging. A source to axis distance (SAD) and a source to detector distance (SDD) were 1000 mm and 1400 mm, respectively. In this MC simulation, determination of azimuth angles $\phi$, polar angles $\omega$ and energy of scattered photons was simulated with the Kahn method using the Klein-Nishina equation [4] and the incoherent scattering function [5]. The uniform random numbers was generated using Double precision SIMD-oriented Fast Mersenne Twister (dSFMT) [6].

The energy $E$ and coordinate ($X$, $Y$) of photons impinged on the EPID were sampled. In the EPID, it is estimated that 99.5 % of the total signal is generated by interactions within the copper and scintillation layer [7]. The 0.5 % of the total signal is due to direct interactions with the photodiodes. And it is reported that the signal of the photodiode is proportional to the energy absorption of the scintillator [7, 8, 9]. Therefore, it was assumed that pixel value of the EPID $P$ is proportional to

absorbed dose $D$ of the scintillator. And the $D$ was calculated by using information of photons impinged on the EPID surface as following.

$$P(X,Y) \propto D(X,Y) = \sum_{i=0}^{E_{\max}} E_i \cdot \Phi(E_i) \cdot \left( \frac{\mu_{\mathrm{en}}(E_i)}{\rho} \right) \tag{1}$$

Where $E_i$ and $\Phi(E_i)$ is energy and fluence of $E_i$ of $i$-th photon that impinged on coordinate ($X$, $Y$), and $\mu_{\mathrm{en}}(E_i) / \rho$ is mass energy absorption coefficient of scintillator to photon energy $E_i$.

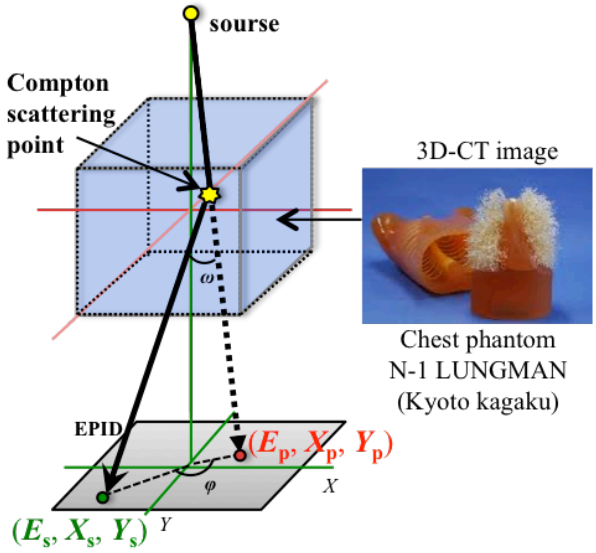


Fig. 3 Three-dimensional drawing for the photon sampling

## 2.3 Contrast improvement

Cancelation of scattered photon's contribution and forecasting of primary photon's contribution improved the image contrast of the EPID. The ratio of absorbed dose by the scattered photons $D_{\mathrm{scatter}}$ to that by the total photons $D_{\mathrm{total}}$ was calculated by using equation (1). Then the pixel value by scattered photons $P_{\mathrm{scatter}}$ was estimated by product of the ratio $D_{\mathrm{scatter}}/D_{\mathrm{total}}$ and pixel value of the original EPID image $P_{\mathrm{raw}}$.

$$P_{\mathrm{scatter}}(X_{\mathrm{s}}, Y_{\mathrm{s}}) = \frac{D_{\mathrm{scatter}}(X_{\mathrm{s}}, Y_{\mathrm{s}})}{D_{\mathrm{total}}(X_{\mathrm{s}}, Y_{\mathrm{s}})} \cdot P_{\mathrm{raw}}(X_{\mathrm{s}}, Y_{\mathrm{s}}) \tag{2}$$

In addition, scattered photons were reused as primary photons on the assumption that Compton scattering did not take place. Absorbed dose by the primary photons to the scintillator $D_{\mathrm{primary}}$ was estimated by energy and fluence of primary photons ($E_{\mathrm{p}}$, $X_{\mathrm{p}}$, $Y_{\mathrm{p}}$) and equation (1). Pixel value by primary photons $P_{\mathrm{primary}}$ was estimated by the following equation.

$$P_{\mathrm{primary}}(X_{\mathrm{p}}, Y_{\mathrm{p}}) = \left( \frac{D_{\mathrm{primary}}(X_{\mathrm{p}}, Y_{\mathrm{p}})}{D_{\mathrm{scatter}}(X_{\mathrm{s}}, Y_{\mathrm{s}})} \right) \cdot P_{\mathrm{scatter}}(X_{\mathrm{s}}, Y_{\mathrm{s}}) \tag{3}$$

Where coordinate ($X_p$, $Y_p$) of primary photons was determined on assumption that Compton scattering did not take place.

Pixel value excluding the scattered photon's contribution $P_\Delta$ was calculated by subtracting $P_{scatter}$ from $P_{raw}$.

$$P_\Delta(X,Y) = P_{\mathrm{raw}}(X,Y) - P_{\mathrm{scatter}}(X,Y) \tag{4}$$

To improve image contrast, the final pixel value $P_{cor}$ was calculated by adding $P_\Delta(X, Y)$ and $P_{primary}(X, Y)$.

,

$$P_{\mathrm{cor}}(X,Y) = P_\Delta(X,Y) + P_{\mathrm{primary}}(X,Y) \tag{5}$$

## 2.4 Benchmark test using the EGS5

The reliability of the simple MC code was confirmed by the comparison of fluence and energy spectrum of scattered photons by the simple MC code with that by the EGS5. Fig. 4 shows the geometrical arrangement of the simulation. As a sampling plane, concentric ring areas $A_i$ were arranged from the center to within a radius of 150 mm at interval of 5 mm. Over the sampling plane, a 30 cm × 30 cm × 30 cm water phantom was arranged 50 mm distant from the plane. Mono energetic photon pencil beams of 0.5, 1, 2, 3, 4, 5, 6 MeV or continuous X-ray of 6 MV were impinged upon the water phantom. For the EGS5 simulation, the cut-off energy of photon (PCUT) was set to 10 keV and electron trajectory was discarded immediately when electron was generated. The history was set to $3\times10^6$ for both simulation. The fluence and energy spectrum of scattered photons were sampled in each ring area $A_i$.

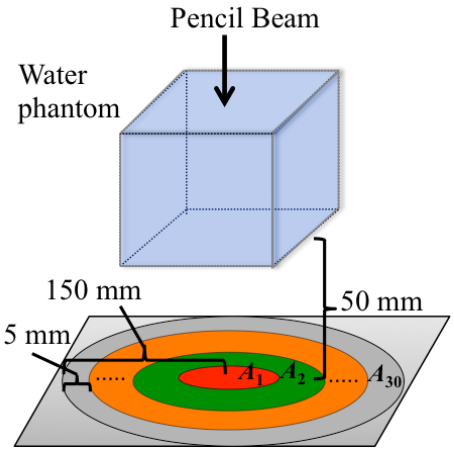


Fig. 4 The geometrical arrangement of the simulation

# 3. Results

## 3.1 Contrast improvement

Fig. 5 shows the image contributed by scattered photon only ($P_{scatter}$). Pixel values of the $P_{scatter}$ image were smoothly increased nearby center of the image.

Fig. 6 shows the image contributed by primary photon ($P_{primary}$), the pixel value of the primary photon was determined on assumption that Compton scattering did not take place.

Fig. 8 shows the contrast-improved image ($P_{cor}$) and Fig. 7 shows original image ($P_{raw}$) for comparison. The spinous process of vertebra and the intervertebral disks in the image $P_{cor}$ were easier to distinguish than the original image $P_{raw}$ in spite of the same window width and window level.

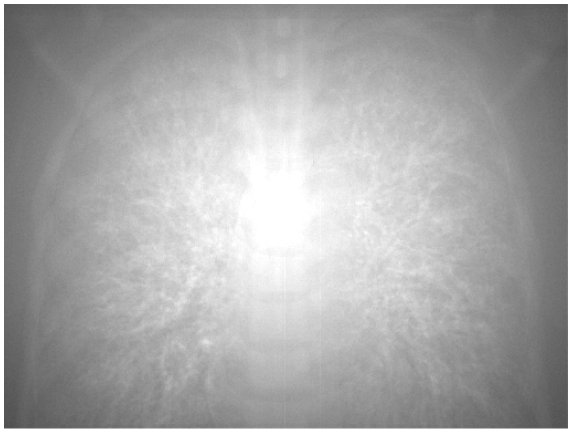

Fig. 5 The image contributed by scattered photons only ($P_{scatter}$).

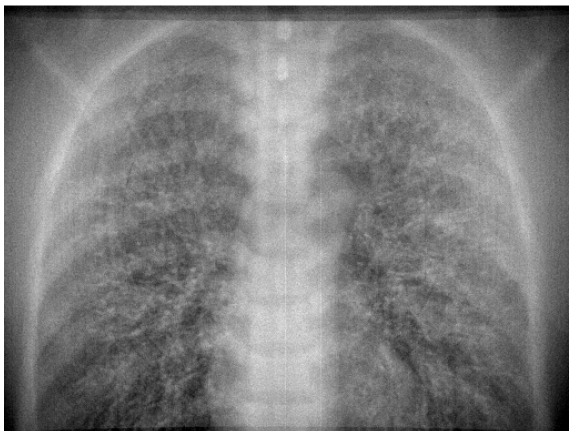

Fig. 6 The image of primary photons on assumption that Compton scattering did not take place ($P_{primary}$).

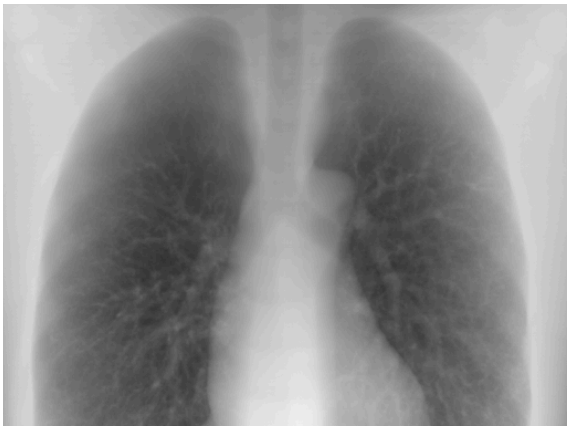

Fig. 7 The original image of EPID ($P_{raw}$)

Fig. 8 The contrast improved image ($P_{cor}$)

## 3.2 Benchmark test using the EGS5

Fig. 9 shows the fluence as a function of distance from the beam center for 6 MeV photon pencil beam as an example. Scattered photon fluence simulated by the simple MC code shows good agreement with that by the EGS5 for all photon energies and sampling areas.

Fig. 10 shows the photon energy spectrum on center circle within a radius of 5 mm as an example. There is no

significant difference between the simple MC code and the EGS5.

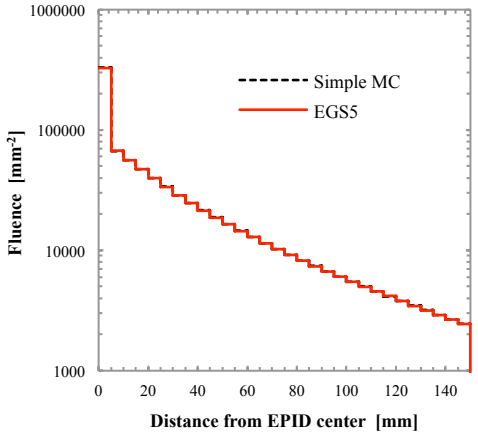


Fig. 9 Scattered photon fluence as a function of distance from the beam center (6 MeV pencil beam)

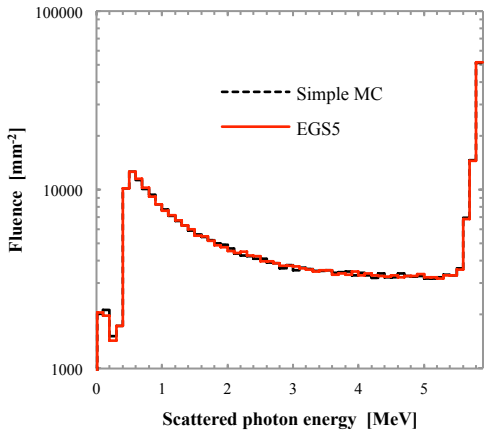


Fig. 10 Scattered photon Energy spectrum on center circle within a radius of 5 mm. (6 MeV pencil beam)

Table 1 shows the comparison of processing time for each simulation. The history was set to $1\times10^{7}$. It was confirmed that processing time was shortened approximately 1/26 by excluding the calculation of electrons in the EGS5. On the other hand, processing time for the simple MC code was similar as for the EGS5 excluding the calculation of electrons. However in spite of the simple MC simulation, $3\times10^{10}$ histories and 20 hours are required for improvement of image contrast. To use this simulation in clinical practice, further speed up must be attempted.

Table 1 Processing time

| EGS5 including electrons [min] | EGS5 excluding electrons [min] | The simple MC code [min] |
|---|---|---|
| 372.0 | 14.5 | 14.1 |

## 5. Conclusions

To improve image contrast of EPID, an original simple MC code and an image-processing program were developed. This MC code was focused on Compton scattered photons to reduce the processing time. In the contrast improvement process, the contribution of scattered photons was cancelled and scattered photons were reused as primary photons on the assumption that Compton scattering did not take place. Consequently, usability of proposed contrast improvement was clarified.

The reliability of the simple MC code was confirmed by the comparison between the simple MC code and the EGS5. And processing time for the simple MC code was evaluated as similar as the EGS5 excluding electrons trajectory.

It is expected that the simple MC code will be faster by implementing on the Graphics Processing Unit (GPU) and the image quality will be more improved using GPU environment.

## References


1) Image Guided Radiation Therapy Guidelines: ATC QA subcommittee report, 2009.
2) C. Coolens, P. Evans, J. Seco, S. Webb, J. Blackall, E. Rietzel, and G. Chen, "The susceptibility of imrt dose distributions to intrafraction organ motion: an investigation into smoothing filters derived from four dimensional computed to- mography data," Medical physics, vol. 33, p. 2809, 2006.
3) H. Hirayama, Y. Namito, A. F. Bielajew, S. J. Wilderman, W. R. Nelson, "The EGS5 Code System, 2005-8, SLAC-R-730", Radiation Science Center Advanced Research Laboratory, High Energy Accelerator Research Organization (KEK), Stanford Linear Accelerator Center, Stan- ford, CA, 2005.
4) Raeside DE: Monte Carlo principles and applications, Phys.Med.Biol.,21(2), pp.181-197, (1976).
5) Hubbell JH, Veigele WJ, Briggs EA, et al. : Atomic form factors, incoherent scattering functions, and photon scattering cross sections, J.Phys.Chem.Ref.Data., 4 (3), pp.471-538, 1975.
6) Mutsuo Saito and Makoto Matsumoto, "A PRNG Specialized in Double Precision Floating Point Number Using an Affine Transition", Monte Carlo and Quasi-Monte Carlo Methods 2008, Springer, 2009, pp. 589 -- 602.
7) C. Kirkby and R. Sloboda. Comprehensive monte carlo calculation of the point spread function for a commercial a-Si EPID. Medical Physics, 32(4) : 1115–1127, March 2005.
8) P. Munro and D. C. Bouius: X-ray quantum limited portal imaging using amorphous silicon flat-panel arrays. Med. Phys. 25 : 689-702 (1998).
9) L. E. Antonuk, Y. El-Mohri, W. Huang, K. W. Jee, J. H. Siewerdsen, M. Maolinbay, V. E. Scarpine, H. Sandler, and J. Yorkston: Initial performance evaluation of an indirect-detection, active matrix flat-panel imager (AMFPI) prototype for megavoltage imaging. Int. J. Radiat. Oncol., Biol., Phys. 42 : 437-454 (1998).

# ABSORBED DOSE CONVERSION FACTOR IN THE FARMER TYPE IONIZATION CHAMBER

**S. TSUJI, N. NARIHIRO[†‡] and M. OITA[‡]**

*Kawasaki Medical School, Kurashiki 701-0192, Japan*

*[†]Kawasaki College of Allied Health Professions, Kurashiki 701-0194, Japan*

*[‡]Okayama University Graduate School of Health Sciences Division of Radiological Technology, Okayama 700-8558, Japan*

**Abstract**

Monte Carlo simulations can be approximated considering the environment of actual measurement in detail. However, it can not be completely corrected by simulations. Because there are some uncertainties on the actual measurement. For example, the amount of charge using the ionization chamber is used to convert the dosimeter measurement of the absorbed dose by the exposure calibration factor for cobalt-60 and the absorbed dose conversion factor. In the simulation, absorbed dose is seeking direct energy per unit mass of water, on the other hand, it is converted to energy per unit mass of water from the charge amount in the air by the exposure calibration factor for cobalt-60 and the absorbed dose conversion factor in actual measurement. We suspect these factors containing uncertainties.

Focusing on the absorbed dose conversion factor, we investigated it by EGS5. We specialized microSelectron-HDR v2 as a radiation source and PTW TN30013 as an ionization chamber.

## 1 Introduction

Brachytherapy using an $^{192}$Ir source is performed based on predetermined treatment plans. Treatment planning systems perform calculations according to the American Association of Physicists in Medicine Task Group No 43 Updated Protocol (AAPM TG-43U1) [1]. Predictions of the absorbed dose based on the TG-43U1 have previously been confirmed in various experiments [2, 3, 4, 5, 6, 7, 8, 9, 10, 11, 12, 13, 14, 15]. Monte Carlo simulations, a type of computer-based simulation, have been used to investigate dose distributions in radiotherapy and have contributed significantly to the development of the TG-43U1 [2]. Absolute dose rates is compared with the EGS5 protocol (hereafter referred to as MC) and actual measurements in Fig. 1.

The absolute dose rates in water delivered to the 0.6 cm$^3$ target volume are shown in Fig. 1 (a), which also compares the dose rate predictions obtained with the MC and the actual measurements. The distance from the source ranged from 2 cm to 15 cm, and both the actual measurements and MC predictions were obtained at 1 cm intervals.

Fig. 1 (b) shows the relative errors of the predictions; i.e., $(\dot{D}_{\mathrm{MC}} - \dot{D}_{\mathrm{mes.}})/\dot{D}_{\mathrm{mes.}}$. The error values are shown relative to the actual measurements. The difference between the MC predictions and the actual measurements was largest at a distance of 2 cm, at which point the relative error was $4.76 \pm 1.90$ %. This error is due to the absorbed dose conversion factor which is converted to energy per unit mass of water from the charge amount in the air. We investigate the absorbed dose conversion factor in the actual measurements by MC and we improve it. We specialized microSelectron-HDR v2 as a radiation source and PTW TN30013 as an ionization chamber.

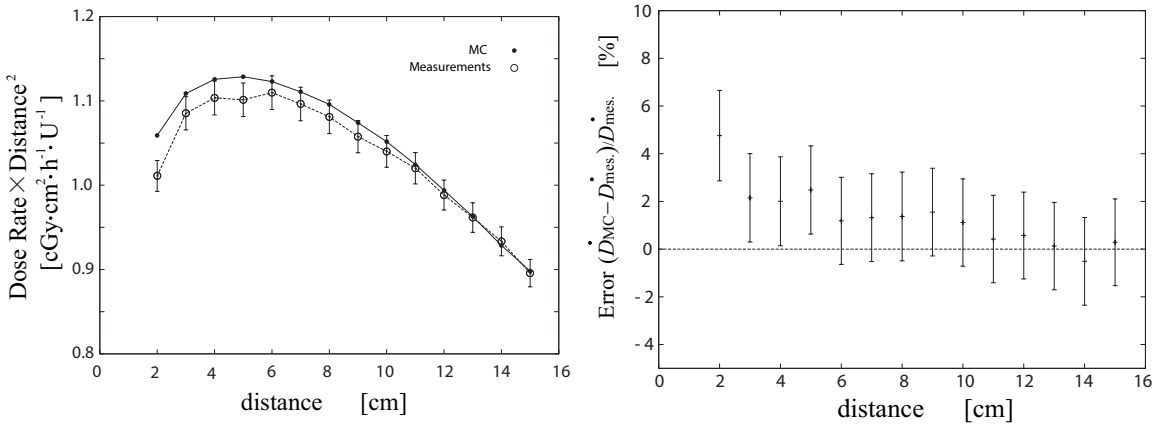


(a) (b)

Figure 1: (a): The absolute dose rates at each distance from the source according to the actual measurements and the predictions of the MC. (b): The relative errors are presented as $(\dot{D}_{\mathrm{MC}} - \dot{D}_{\mathrm{mes.}})/\dot{D}_{\mathrm{mes.}}$. $\dot{D}_{\mathrm{mes.}}$: The measured absolute dose rate. $\dot{D}_{\mathrm{MC}}$: MC absolute dose rate. The error values are relative to the actual measurements.

# 2 Methods

## 2.1 Experimental setup

Fig. 2 shows the setup used for the actual measurements. The microSelectron-HDR system pushed the radiation source out of its container and held it there for a set period. The phantom measured 35 cm × 35 cm × 30 cm, and its walls were 1 cm thick. Water was added to the phantom to a depth of 30 cm. The PTW TN30013 farmer-type ionization chamber and radiation source cable were supported by blocks of PMMA (polymethyl methacrylate).

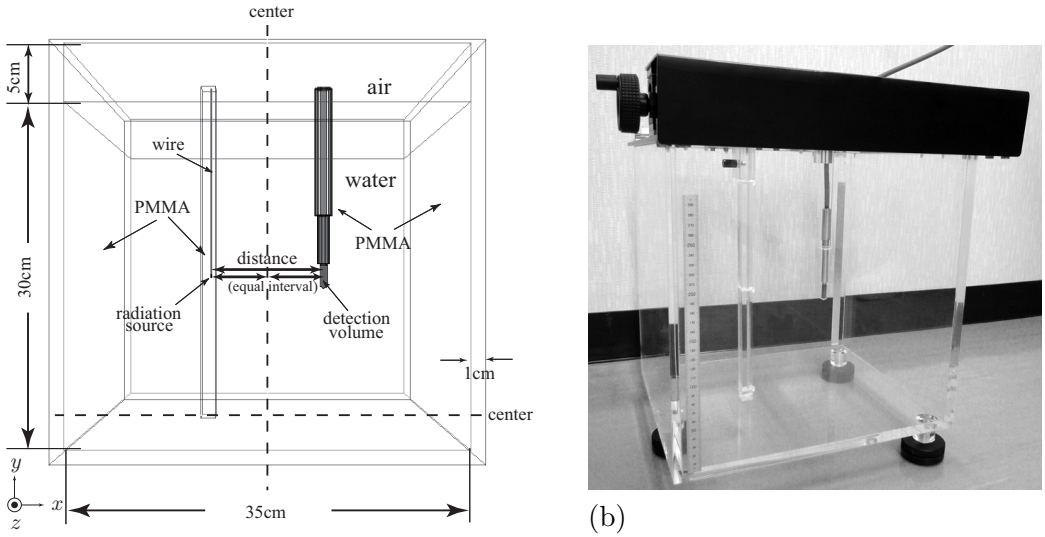


(a) (b)

Figure 2: Setup of the actual measurement system. The distance between the radiation source and the detection volume was measured. The phantom was filled with water to a depth of 30 cm. Above this lay 5 cm of air. The radiation source tube and detector were supported by PMMA blocks. (a): Structure of the simulated phantom produced with CG. (b): A picture of the actual measurement system.

### 2.2 Method of absolute dose rate calculation

PTW TN30013 Farmer-type ionization chamber has a detection volume of 0.6 $cm^3$ for the actual measurements. The ionization chamber was calibrated with a $^{60}$Co beam using the exposure calibration factor for $^{60}$Co ($N_c$). The measured absolute dose rate, $\dot{D}_{\text{mes.}}$, in the detection volume was calculated using the following equation:

$$\dot{D}_{\text{mes.}} = \frac{M \cdot N_c \cdot C_\lambda \cdot k}{\text{radioactivity (MBq)} \cdot \text{observation time (h)} \cdot \Gamma_{\delta=10\text{keV}}}, \tag{1}$$

where the absolute dose rate, $\dot{D}_{\text{mes.}}$, has units of $\mu$Gy·h$^{-1}$·U$^{-1}$; the measured charge, $M$, has units of nC; the exposure calibration factor for $^{60}$Co, $N_c$, has units of C·kg$^{-1}$/nC; the absorbed dose conversion factor, $C_\lambda$, has units of Gy/C·kg$^{-1}$; and the correction factor for air temperature and air pressure, $k$, has dimensionless units. Note, U is a unit of the air kerma strength, 1U=1$\mu$Gy·m$^2$/h. We refer to 0.1091 as the value of the air kerma rate constant, $\Gamma_{\delta=10\text{keV}}$, has units of U ·MBq$^{-1}$ [16]. The absolute dose rate was converted from the amount of charge using these coefficients.

On the other hand, the MC absolute dose rate, $\dot{D}_{\text{MC}}$, in the detection volume was directly calculated using the following equation:

$$\dot{D}_{\text{MC}}(\mu\text{Gy} \cdot \text{h}^{-1} \cdot \text{U}^{-1}) = fc \cdot SV, \tag{2}$$

where $SV$ is dose in water with units of Gy/photon. $fc$ is a constant for air-kerma with units of photons ·U$^{-1}$ · h$^{-1}$. $fc$ is also calculated by MC in the air. The actual measurement results in Fig. 1 use constant value of the absorbed dose conversion factor, $C_\lambda = 37.8$ Gy/C·kg$^{-1}$.

## 3 Investigation and results

### 3.1 The absorbed dose conversion factor in the charged particle equilibrium state

Dose in a material $Z$ in charged particle equilibrium state, $D_Z$ presents the following equation:

$$D_Z = \Psi \cdot (\mu_{en}/\rho)_Z, \tag{3}$$

where $\Psi$ is the energy fluence and $(\mu_{en}/\rho)_Z$ is the mass energy absorption coefficient of the material $Z$ [17]. From equation (3), Dose in water $D_{water}$ shows

$$D_{water} = D_{air} \frac{(\mu_{en}/\rho)_{water}}{(\mu_{en}/\rho)_{air}}, \tag{4}$$

using dose in air $D_{air}$. $D_{air}$ is

$$D_{air} = 33.97X, \tag{5}$$

where $X$ is the exposure with the unit C/kg. $D_{water}$ is

$$D_{water} = 33.97 \cdot \frac{(\mu_{en}/\rho)_{water}}{(\mu_{en}/\rho)_{air}} \cdot X, \tag{6}$$

as a result. Actual measurements use the ionization chamber filled with the air. Equation (5) replesents directly measurements by the ionization chamber. $33.97 \cdot (\mu_{en}/\rho)_{water}/(\mu_{en}/\rho)_{air}$ corresponds to the absorbed dose conversion factor $C_\lambda$. The mass energy absorption coefficient $(\mu_{en}/\rho)_Z$ depends on the incident energy in the detector. We investigate it at each distance from the source using the detector filled with water or air. $1.0 \times 10^9$ photons are shot toward within $\pm$1.5 cm from the center of detector at each distance. The ratio of the mass energy absorption coefficients $(\mu_{en}/\rho)_{water}/(\mu_{en}/\rho)_{air}$ and the absorbed dose conversion factor $C_\lambda$ are shown in Fig. 3.

From our results, the averaged ratio of the mass energy absorption coefficients $(\mu_{en}/\rho)_{water}/(\mu_{en}/\rho)_{air}$ is $1.10964 \pm 0.00002$ and the absorbed dose conversion factor $C_\lambda$ is 37.69 which closes to the conventional value 37.8.

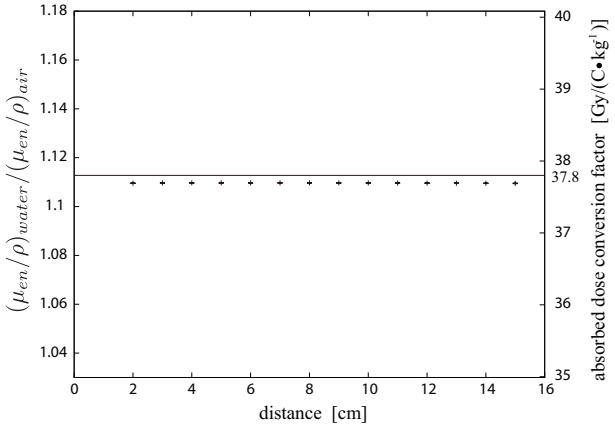


Figure 3: The left and right vertical axes represent the ratio of the mass energy absorption coefficients $(\mu_{en}/\rho)_{water}/(\mu_{en}/\rho)_{air}$ and the absorbed dose conversion factor $C_\lambda$ respectively. The line shows the conventional value 37.8. Plots are averaged $37.69(=C_\lambda)$ and $1.10964(=(\mu_{en}/\rho)_{water}/(\mu_{en}/\rho)_{air})$.

### 3.2 The range in the charged particle equilibrium state

Fig. 3 is the result of only when the charged particle equilibrium is established. We investigate the range in charged particle equilibrium state. As shown in Fig. 4(a), electron energy entering


(a) (b)

Figure 4: (a): $E_E$ Electron energy entering in the detector. $E_L$ Electron energy leaving from the detector. Detection volume is filled with air or water. (b): The electron with $E_E$ had caused bremsstrahlung at A and the generated gamma-ray caused a Compton scattering at B. Dashed line shows a gamma-ray.

($E_{\rm E}$) and leaving ($E_{\rm L}$) the detector are summarized. We take the difference between them. Under the charged particle equilibrium state, the difference is zero with a minimum area. However the detection volume have 0.6 cm$^3$, the difference is not zero in the charged particle equilibrium state. For example, if entering electron ($E_{\rm E}$) had caused bremsstrahlung in the detector and the generated gamma-ray caused a Compton scattering in the detector and the generated electron ($E_{\rm L}$), $E_{\rm E}$ is larger than $E_{\rm L}$ as shown in Fig. 4(b). However the phenomenon shown in Fig. 4(b) is considered to be occurred at a constant regardless of the distance from the source.

The difference between $E_{\rm E}$ and $E_{\rm L}$ is shown in Fig. 5. The detection volume is filled with water or air. MC is done $1.0 \times 10^9$ photons shot toward within $\pm 1.5$ cm from the center of detector at each distance. The differences become constant at the distance 8 cm from the source in the air and 10 cm in the water. From these results, a charged particle equilibrium can be considered from the distance more than 10 cm.

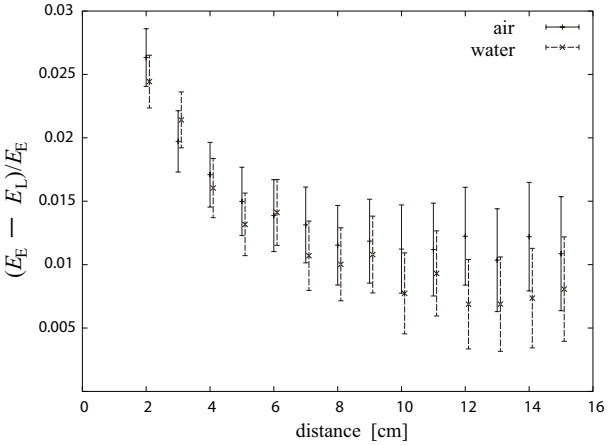


Figure 5: The difference between $E_{\mathrm{E}}$ and $E_{\mathrm{L}}$, $(E_{\mathrm{E}} - E_{\mathrm{L}})/E_{\mathrm{E}}$. Figure shows the results in the detection volume filled with water or air.

### 3.3 The absorbed dose conversion factor in the non-charged particle equilibrium state

In the distance less than 10 cm from the source, equation (6) is not adopted. Therefore, it is reasonable to adapt the following equation,

$$D_{water} = 33.97 \cdot \frac{D_{\mathrm{MC}\,water}}{D_{\mathrm{MC}\,air}} \cdot X, \tag{7}$$

where $D_{\mathrm{MC}\,water}$ and $D_{\mathrm{MC}\,air}$ are doses by MC. $3.0 \times 10^{10}$ gammma-rays was used in $D_{\mathrm{MC}\,air}$ and $1.0 \times 10^{10}$ gamma-rays was used in $D_{\mathrm{MC}\,water}$ each distance (from 2cm to 9 cm). The gamma-rays were emitted $4\pi$ srad direction from the source. The ratio of $D_{\mathrm{MC}\,water}$ to $D_{\mathrm{MC}\,air}$, $D_{\mathrm{MC}\,water}/D_{\mathrm{MC}\,air}$ is shown in Fig. 6.

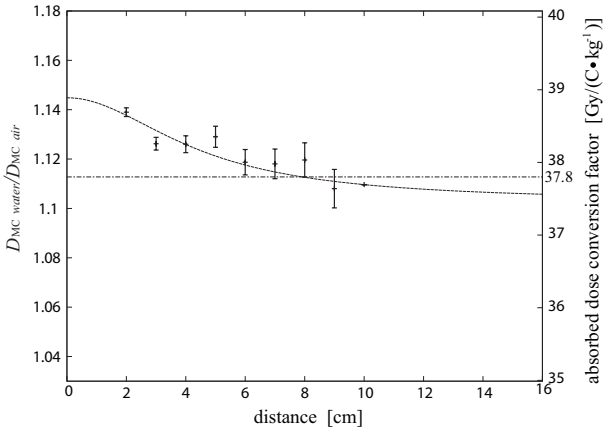


Figure 6: The left and right vertical axes represent the ratio of doses $D_{\mathrm{MC}\,water}/D_{\mathrm{MC}\,air}$ and the absorbed dose conversion factor $C_\lambda$ respectively. At 10 cm, the value is the ratio of the mass energy absorption coefficients $(\mu_{en}/\rho)_{water}/(\mu_{en}/\rho)_{air}$ as shown in Fig. 3. The dash-dotted line shows the conventional value 37.8. The dash line shows fitting function $f(r) = A + B/(x^2 + C)$.

The value at distance 10 cm is only used $(\mu_{en}/\rho)_{water}/(\mu_{en}/\rho)_{air}$ in Fig. 3. Fitting function is mentioned in subsection 3.4.

### 3.4 Fitting function of $D_{\mathrm{MC}\,water}/D_{\mathrm{MC}\,air}$

Following AAPM TG-43U1 [1], when $\theta = 90°$, dose is determined by the geometry function and the radial dose function $g(r)$. The geometry function is proportional to $r^{-2}$ as a distance $r$ away from the source. The radial dose function is for excluding dose fall-off included by the geometry function. Fig. 7 shows the radial dose function by Daskalov using TG-43U1. Fitting function is

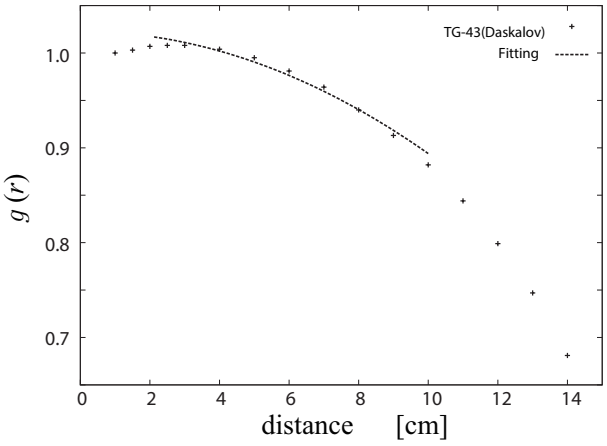


Figure 7: The radial dose functions, $g(r)$ of TG-43U1 (Daskalov) [2]. Dash line is fitted by $ar^2 + b$ from 2 cm to 10 cm.

quadratic function, $g(r) = ar^2 + b$. Following AAPM TG-43U1, $D_{\mathrm{MC}\,water}/D_{\mathrm{MC}\,air}$ is equivalent to $g_{water}/g_{air}$, where $g_{water}$ and $g_{air}$ are the radial dose functions of the water and the air. Therefore the ratio of $D_{\mathrm{MC}\,water}$ to $D_{\mathrm{MC}\,air}$ is

$$f(r) = \frac{D_{\mathrm{MC}\,water}}{D_{\mathrm{MC}\,air}} = \frac{g_{water}}{g_{air}} = \frac{ar^2 + b}{a'r^2 + b'} = A + \frac{B}{r^2 + C} \tag{8}$$

We fit the data in Fig. 6 in equation (8). Finally, the equation is

$$f(r) = 1.1028 + \frac{0.8228}{r^2 + 19.56}, \tag{9}$$

where degrees of freedom (ndf) are 6, the reduced chisquare $\chi^2$/ndf is 1.6204. In summary conclusion, the absorbed dose conversion factor $C_\lambda$ is

$$C_\lambda = 33.97 \cdot \left(1.1028 + \frac{0.8228}{r^2 + 19.56}\right) \quad (2\ \mathrm{cm} \le r < 10\ \mathrm{cm}), \tag{10}$$

$$C_\lambda = 37.69 \quad (10\ \mathrm{cm} < r). \tag{11}$$

## 4 Conclusion

### 4.1 Applied to actual measurement data

The results applied equations (10) or (11) to measurement data are shown in Fig. 8.

The results between MC and actual measurements are good agreement within error bars in Fig. 8 (a). Using constant value of the absorbed dose conversion factor $C_\lambda = 37.8$, the largest difference between the MC predictions and the actual measurements was largest at a distance of 2 cm was $4.76 \pm 1.90$ % in Fig. 1 (b). It was improved $2.46 \pm 3.1$ % in Fig. 8 (b) using the absorbed dose conversion factor $C_\lambda$ in equations (10) or (11). The difference between the MC predictions and the actual measurements are within 2 % as a whole.

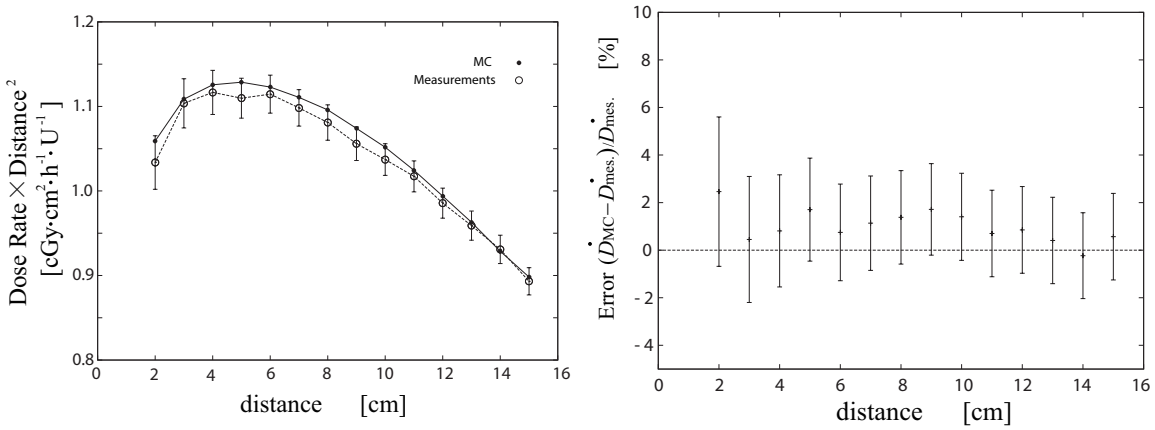


(a) (b)

Figure 8: The measured absolute dose rate is applied by equations (10) or (11). (a): The absolute dose rates at each distance from the source according to the actual measurements and the predictions of the MC. (b): The relative errors are presented as $(\dot{D}_{\mathrm{MC}} - \dot{D}_{\mathrm{mes.}})/\dot{D}_{\mathrm{mes.}}$. $\dot{D}_{\mathrm{mes.}}$: The measured absolute dose rate. $\dot{D}_{\mathrm{MC}}$: MC absolute dose rate. The error values are relative to the actual measurements.

## 5 Acknowledgements

The computations were mainly carried out using the computer facilities at the Research Institute for Information Technology, Kyushu University.

## References

[1] M. J. Rivard, B. M. Coursey, L. A. DeWerd, W. F. Hanson, M. S. Huq, G. S. Ibbott, M. G. Mitch, R. Nath, and J. F. Williamson, "Update of AAPM Task Group No.43 Report: A revised AAPM protcol for brachytherapy dose calculations," Med. Phys. **31**,633-673 (2004).

[2] G. M. Daskalov, E. Löffler, and J. F. Williamson, "Monte Carlo-asided dosimetry of new high dose-rate brachytherapy source," Med. Phys. **25**, 2200-2208 (1998).

[3] D. C. Medich and J. J. Munro III, "Monte Carlo characterization of M-19 high dose rate Iridium-192 brachytherapy source," Med. Phys. **34**, 1999-2006 (2007).

[4] A. Sarfehnia and J. Seuntjensa, "Development of a water calorimetry-based standard for absorbed dose to water in HDR $^{192}$Ir brachytherapy," Med. Phys **37**, 1914-1923 (2010).

[5] A. Sarfehnia, I, Kawrakow and J. Seuntjensa, "Direct measurement of absorbed dose to water in HDR $^{192}$Ir brachytherapy: Water calorimetry, ionization chamber, Gafchromic film, and TG-43," Med. Phys **37**, 1924-1932 (2010).

[6] J. Anctil, B. G. Clark, and C. J. Arsenault, "Experimental determination of dosimetry functions of Ir-192 sources," Med. Phys. **25**, 2279-2287 (1998).

[7] C. S. Melhus and M. J. Rivard, "Approaches to calculating AAPM TG-43 brachytherapy dosimetry parameters for $^{137}$Cs, $^{125}$I, $^{192}$Ir, $^{103}$Pd, and $^{169}$Yb sources," Med. Phys. **33**, 1729-1737 (2006).

[8] D. Baltasyz, S. Giannouliyk, A. Garbiyk, F. Diakonosx, K. Geramaniyk, G. T. Ioannidisyk, A. Tsalpatourosk, N. Uzunogluzk, C. Kolotasy, and N. Zamboglou, "Application of the Monte

Carlo integration (MCI) method for calculation of the anisotropy of $^{192}$Ir brachytherapy sources," Phys. Med. Biol., **43**, 1783-1801 (1998).

[9] F. Ballester, J. Pérez-Calatayud, V. Puchades, J. L. Lluch, M. A. Serrano-Andrés, Y. Limami, F. Lliso, and E. Casal, "Monte Carlo dosimetry of the Buchler high dose rate $^{192}$Ir source," Phys. Med. Biol. **46**, N79-N90 (2001).

[10] C. Gromoll and A. Karg, "Determination of the dose characteristics in the near area of a new type of $^{192}$Ir-HDR afterloading source with a PinPoint ionization chamber," Phys. Med. Biol. **47**, 875-887 (2002).

[11] A. Angelopoulos, P. Baras, L. Sakelliou, P. Karaiskos, and P. Sandilos,"Monte Carlo dosimetry of a new $^{192}$Ir high dose rate brachytherapy source," Med. phys. **27**, 2521-2527 (2000).

[12] P. Karaiskos, A. Angelopoulos, L. Sakelliou, P. Sandilos, C. Antypas, L. Vlachos,and E. Koutsouveli, "Monte Carlo and TLD dosimetry of $^{192}$Ir high dose-rate brachytherapy source," Med. Phys. **25**, 1975-1984 (1998).

[13] K. A. Weaver, V. Smith, D. Huang, C. Barnett, M. C. Schell, and C. Ling, "Dose parameters of $^{125}$I and $^{192}$Ir seed sources,"Med. Phys. **16**, 636-643 (1989)

[14] R. Nath, A. S. Meigooni, and J. A.Meli, "Dosimetry on transverse axes of $^{125}$I and $^{192}$Ir interstitisl brachytherapy sources," Med. Phys. **17**, 1032-1040 (1990)

[15] J. F. Williamson and Z. Li, "Monte Carlo aided dosimetry of the microselectron pulsed and high dose-rate $^{192}$Ir sources," Med. Phys. **22**, 809-819 (1995)

[16] J. Perez-Calatayud, F. Ballester, R. K. Das, L. A. Dewerd, G. S. Ibott, A. S. Meigooni, Z. O. Ouhib, M. J. Riverd, R. S. Sloboda, J. F. Williamson, "Dose calculation for photon-emitting brachytherapy sources with average energy higher than 50keV: Report of the AAPM and ESTRO," Med. Phys. **39**, 2904-2929 (2012)

[17] National Institute of Standards and Technology,
http://physics.nist.gov/PhysRefData/XrayMassCoef/tab3.html,
or http://physics.nist.gov/PhysRefData/XrayMassCoef/tab4.html

# PERTURBATION OF RUTHENIUM 106 BETA-PARTICLE FIELD DUE TO ELECTRODES IN AN EXTRAPOLATION CHAMBER

**M. Kato, T. Kurosawa, and N. Saito**

*National Metrology Institute of Japan, National Institute of Advanced Industrial Science and Technology,*
*Umezono 1-1-1, Tsukuba, Ibaraki 305-8568, Japan*
*e-mail: masahiro-katou@aist.go.jp*

**Abstract**

We have studied how electrodes in an extrapolation chamber effect on beta-particle radiation field from a Ru-106 ophthalmic applicator. The extrapolation chamber is a primary standard detector that determines an absorbed dose rate to water in beta-particle radiation fields. A Monte Carlo method with the EGS5 code was used in this study. Energy spectra of the beta-particles in charge collecting volume of the extrapolation chamber have been calculated for several chamber depths and several materials of the electrodes. The ratio of the mean mass-electronic stopping powers in water to air is derived from the electron energy spectra calculated. Energy deposits in the charge collecting volume have been also calculated for two chamber depths and two materials of the electrodes in order that a correction factor for the difference in backscatter between water and the material of the electrodes has been determined.

.

## 1. Introduction

Brachytherapy, which is defined as intracavitary, interstitial, superficial (including ophthalmic), or intraluminal radiotherapy in the immediate vicinity of one or more sealed or unsealed radioactive sources, has been used since the beginning of 20th century [1]. The application of brachytherapy sources requires adequate dosimetry traceable to the national standard. In recent years, National Metrology Institute of Japan (NMIJ) has been developing the dose standards for brachytherapy sources [2]. A calibration service for I-125 [3] and Ru-106 brachytherapy sources started in 2013 and 2014, respectively, while the dose standards for Ir-192 source is planned to be disseminated in a couple of years. The Ru-106 beta particle sources are widely used as ophthalmic applicators [1]. Accurate dosimetry measurements for the Ru-106 sources have a difficulty because dose rate changes significantly around the point to be measured due to the short distance from the source to the point, and some of the sources have a concave shape. Radiochromic films and thermoluminescence dosemeters are generally used for the dose-rate measurements for the Ru-106 sources [1,4-6]. Because these detectors are not suitable for the absolute measurements, they should be calibrated against some measurement standards. The most suitable standard instrument for the absolute dose measurements in beta-particle radiation fields is an extrapolation chamber [1,7].

In the extrapolation chamber measurement, a discrepancy between the ideal conditions based on a definition of a quantity and actual conditions of the measurement, that is a perturbation of the reference radiation fields by the extrapolation chamber, need to be considered. A Monte Carlo simulation is a well-known method to derive a correction factor for this perturbation effect. In this study, we would like to examine the influence of the electrodes in the

extrapolation chamber on the radiation field. In the beta radiation dosimetry, the backscattering correction factor [7], which corrects for the difference in backscatter between the reference material and the material of the collecting electrode and guard ring, is an important correction factor in the extrapolation chamber measurements. An electron energy spectrum in the charge collecting volume which is usually affected by the electrodes is also important because it is necessary to derive the mean mass-electronic stopping powers required in the ionization chamber measurements [8]. In order to derive the backscattering correction factor and the ratio of the mean mass-electronic stopping powers in water to air, the energy deposits and the electron energy spectra in the charge collecting volume of the chamber are calculated by the EGS5 (Electron Gamma shower 5) code system for several geometrical conditions.

## 2. Materials and Methods

### 2.1 Beta particle source, Ru-106 ophthalmic applicator

In this paper, we study the beta-particle fields for the Ru-106 beta-particle source designed as an ophthalmic applicator (Eckert & Ziegler BEBIG, type COC). Figure 1 shows the picture and schematic diagram of the cross section of the applicator. The source is called as a concave source which shape is a part of a spherical surface. The dimensions of the diameter *D*, radius *R*, and height *h* of the source shown in the figure are provided by the manufacture. The source is made of silver of the 1 mm thickness. The purity of the silver is 0.9999, therefore it regarded as unity in this study. Radioactive ruthenium is uniformly distributed over a depth of 0.1 mm inside the silver. The incident energies of the beta particles for this calculation were determined according to a function reported in ICRU72 [9]. The energy bin of the incident energy was set to 50 keV.

### 2.2 Geometries

Figure 2(a) and (b) are the picture of the extrapolation chamber (C112-C, Applied Engineering Inc.) and its cross section, respectively. The extrapolation chamber is irradiated by the beta-particle radiation from the right side of the figure. The specification of the chamber is listed in Table 1. The entrance window which works as the high voltage electrode is made of polyethylene deposited with aluminum of 6 μm thickness. The collecting electrode and the guard ring which are made of graphite with the density of 1.92 g/cm$^3$ are insulated by polytetrafluoroethylene. The chamber depth that is the distance between the electrodes (the collecting electrode and the guard ring) and the entrance window can be changed by moving the part including the electrodes. The collecting volume, therefore, varies with the chamber depth. This geometrical and material information of the extrapolation chamber was written into the user codes for EGS5. Figure 3(a) shows the position where we intend to determine the absorbed dose to water, while in Figure 3(b) a schematic diagram of the calculation geometry is shown. The reference point of the extrapolation chamber is placed at the position to be measured. The dimension and material of the calculation geometries are summarized in Table 2. The calculation was performed for the chamber depths of 0.2 mm, 0.5mm and 1.5 mm, and for three kinds of the electrodes made of graphite (geometry A), air (geometry B) and water (geometry C).

### 2.3 Calculation method

The user codes used in this study were based on a KEK sample user code, ucphantomcgv.f [10]. The EGS5 code system was run on Cygwin with an operating system Windows Vista or Windows 7. The parameters EDEP (energy deposited) and USTEP (actual transport step) were scored for the dose rate calculation and for the electron energy spectra calculation, respectively. The cutoff energies for the transport calculation of electron (ECUT) and photon (PCUT) in all calculations were set to 521 keV and 10 keV, respectively. The history number was $2\times10^7$ or $1\times10^8$. The option

parameters were set as default.

## 3. Results and Discussion

### 3.1 Electron energy spectra and the ratio of the mean mass-electronic stopping power in water to air

Figure 4 shows the electron energy spectra in the collecting volume calculated for the geometry of the actual extrapolation chamber with the chamber depth of 0.2 mm, 0.5 mm and 1.5 mm (geometry A), and the geometry in which the graphite electrodes are replaced by air electrodes (geometry B). The width of the energy bin in the calculation was 0.07 MeV. The spectral fluence in the low energy region for geometry A, which is larger than that for geometry B, seems to be due to electrons scattered by the electrodes. In the geometry B the shape of the spectra is almost same each other even if the chamber depths are different, while in the geometry A the low energy component in the spectrum of the chamber depth of 1.5 mm is smaller than those of others. This is because the contribution of the scattered electrons is small in the chamber depth of 1.5 mm. Figure 4 also shows an electron energy spectrum measured for a plane Ru-106 source with the window thickness of 50 mg/cm$^2$ reported in the ISO 6980-1 as the solid curve [11]. This spectrum was measured by a semiconductor detector placed on a distance of 10 cm from the Ru-106 source. The measured spectrum would be compared with that for geometry B rather than that for geometry A because the scattered electrons counted in geometry A are not involved in the measured spectrum [11]. The measured spectrum is normalized to the spectrum for geometry B at the maximum. The high energy component of the spectrum for the geometry B is relatively small in comparison with the measured spectrum. This may come from the difference of the window thickness.

We have derived the ratio of the mean mass-electronic stopping power in water to air with a method described in ISO6980-2[7] based on the spectra. The results are summarized in Table 3. The values of the ratio are in the range of 1.0999 to 1.1052 with the uncertainty of 0.007. The ratio obtained from the spectra for geometry A should be used for the determination of the absolute dose values because the geometrical condition are almost identical to the actual geometrical condition of the extrapolation chamber.

### 3.2 Backscattering correction factor of the extrapolation chamber for Ru-106 beta-particle field

The back scattering correction factor for the extrapolation chamber measurement is to correct the difference in backscatter between water and the material of the collecting electrode and guard ring. In order to determine the backscattering correction factor, the energy deposits of the collecting volume in two geometric conditions (geometry A and geometry C) were calculated. The back scattering correction factor is regarded as independent from the chamber depth according to the ISO 6980-2:2004, however, we have calculated the correction factor in two chamber depths. The energy deposit calculated with the geometries for the chamber depth of 0.2 mm and 0.5 mm provides the values of the correction factor as $0.990 \pm 0.006$ and $0.992 \pm 0.004$, respectively. The correction factors for the different chamber depths agree within the uncertainty.

## 4. Conclusions

The influence of the electrodes in the extrapolation chamber on the beta-particle radiation field produced by the Ru-106 has been studied with the EGS5 code system. The spectral fluence of the electron in the charge collecting volume was calculated in the several geometrical conditions. The contribution of the scattered electrons was observed in low energy region of the spectra while the ratio of the mean mass-electronic stopping power in water to air derived based on

the spectral fluence in the several geometrical conditions agree within the uncertainty. The backscattering correction factor of the extrapolation chamber for the Ru-106 radiation fields was determined as 0.990 ± 0.006 or 0.992 ± 0.004 which was also obtained with the calculation in this study.

## References


1) ISO 21439:2009, "Clinical dosimetry – Beta radiation sources for brachytherapy" (2009).
2) M. Kato, T. Kurosawa and N. Saito, "Calculation of dose rate distributions for a ruthenium ophthalmic applicator", KEK Proceedings **24**, 2013-6 (2013).
3) Y. Unno, A. Yunoki, T. Kurosawa, T. Yamada, Y. Sato, Y. Hino, "Measurement of anisotropic angular distributions of photon energy spectra for I-125 brachytherapy sources", Applied Radiation and Isotopes **70**, 2240 (2012).
4) C. G. Soares, "Calibration of ophthalmic applicators at NIST: A revised approach", Med. Phys. **18**, 787-793 (1991).
5) G. Taccini, F. Cavagnetto, G. Coscia, S. Garelli, and A. Pilot, "The determination of dose characteristics of ruthenium ophthalmic applicators using radiochromic film", Med. Phys. **24**, 2034-2037 (1997).
6) C. S. Soares, S. Vynckier, H. Järvinen, W. G. Cross, P. Sipilä, D. Flühs, B. Schaeken, F. A. Mourtada, G. A. Bass, and T. T. Williams, "Dosimetry of beta-ray ophthalmic applicators: Comparison of different measurement methods", Med. Phys. **28**, 1373-1384 (2001).
7) ISO 6980-2:2004, International Organization for Standardization, Nuclear energy – Reference beta-particle radiation – Part 2: Calibration fundamentals related to basic quantities characterizing the radiation field (2004).
8) H. Hirayama, Y. Namito, A.F. Bielajew, S.J. Wilderman and W.R. Nelson,"The EGS5 code System", SLAC-R-730 (2005).
9) ICRU Report 72, "Dosimetry of Beta Rays and Low-Energy Photons for Brachytherapy with Sealed Sources", (Bethesda, MD) 2004.
10) EGS activities at KEK, http://rcwww.kek.jp/research/egs/kek/
11) ISO 6980-1:2006, International Organization for Standardization, Nuclear energy – Reference beta-particle radiation – Part 1: Methods of production (2006).

Table 1 Specification of the extrapolation chamber (C-112C, Oyogiken) used for measuring the absorbed dose rate to water in Ru-106 beta-particle fields.

| Parameter | | Specification of C-112C |
|---|---|---|
| Entrance window | Material | Aluminum evaporated polyethylene |
| | Thickness | 6 μm |
| | Density | 0.80 $g \cdot cm^{-3}$ |
| Collector | Material | Graphite |
| | Density | 1.92 $g \cdot cm^{-3}$ |
| | Thickness | 20 mm |
| | Diameter | 3.99 mm |
| Guard ring | Material | Graphite |
| | Density | 1.92 $g \cdot cm^{-3}$ |
| | Width | 30.81 mm |
| Insulation gap | Material | Polytetrafluoroethylene (Teflon®) |
| | Width of the gap | 0.2 mm |
| | Depth of the gap | 20 mm |
| Range of chamber depth for usual measurements | | 0.2 mm- 1.5mm |

Table 2. The dimension and material of the calculation geometries shown in Figure 3(b) together with those of the actual extrapolation chamber.

| | Chamber depth in mm | Material of electrodes | Material of insulation gap |
|---|---|---|---|
| Actual extrapolation chamber | 0.07 – 10* | Graphite | Polytetrafluoroethylene |
| Geometry A | 0.2, 0.5, 1.5 | Graphite | Polytetrafluoroethylene |
| Geometry B | 0.2, 0.5,1.5 | Air | Air |
| Geometry C | 0.2, 0.5 | Water | Water |

*The chamber depth can be varied in the range shown in this cell, but we usually use the range of 0.2mm-1.5mm for the measurements.

Table 3. The ratio of the mean mass-electronic stopping power in water to air for the Ru-106 radiation field. The standard uncertainty of each value is 0.007.

| | 0.2 mm | 0.5 mm | 1.5 mm |
|---|---|---|---|
| Geometry A | 1.1052 | 1.1051 | 1.1050 |
| Geometry B | 1.1000 | 1.1000 | 1.0999 |

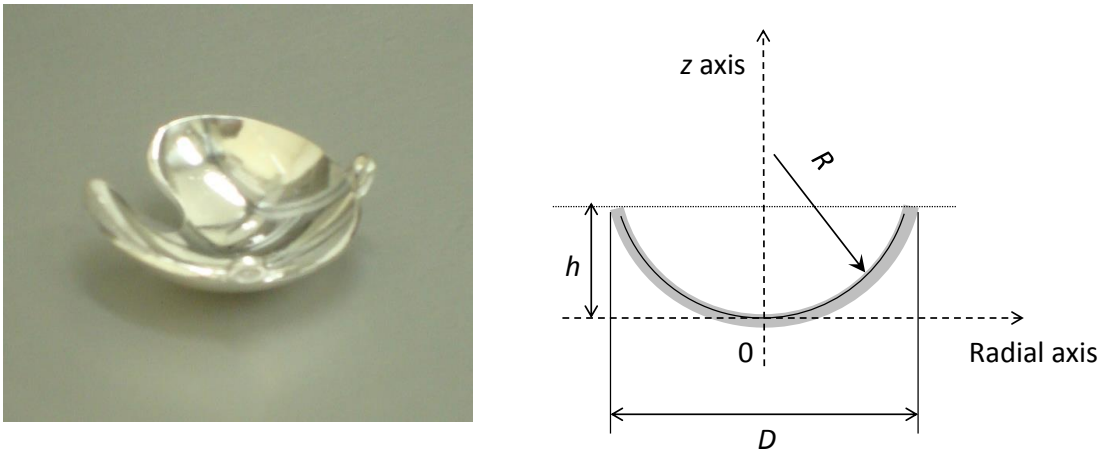


**Figure 1.** Picture of a COC type Ru-106 source (left), and schematic drawing of the cross section (right). The solid curve in the gray colored region in the right figure refers to a radioactive layer. Geometric parameters of the COC type sources are 25.4 mm in diameter *D*, 14 mm in radius *R*, and 7.5 mm in height *h*.

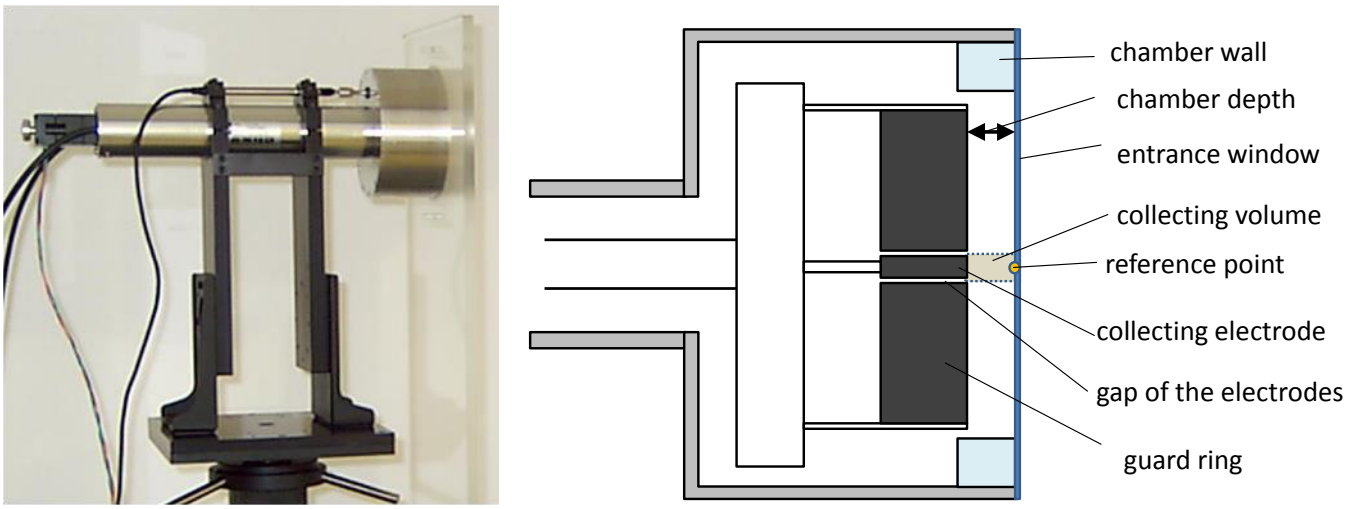


**Figure 2.** Picture of the extrapolation chamber (left), and schematic drawing of the cross section (right). Detail specification of the extrapolation chamber is summarized in Table 1.

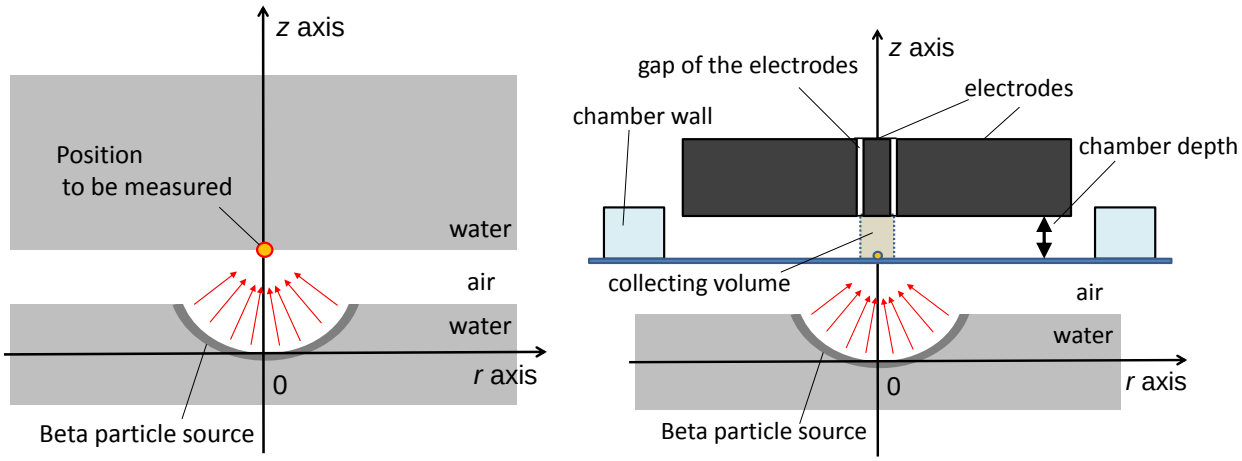


**Figure 3.** (a) Geometry of the position where the absorbed dose to water is determined in the cylindrical coordinate system. The definition ($r$, $z$) of the position is (0 mm, 10.5 mm). (b) Calculation geometry described in the cylindrical coordinate system. The detail of a dimension and material of the calculation geometry are shown in Table 2.

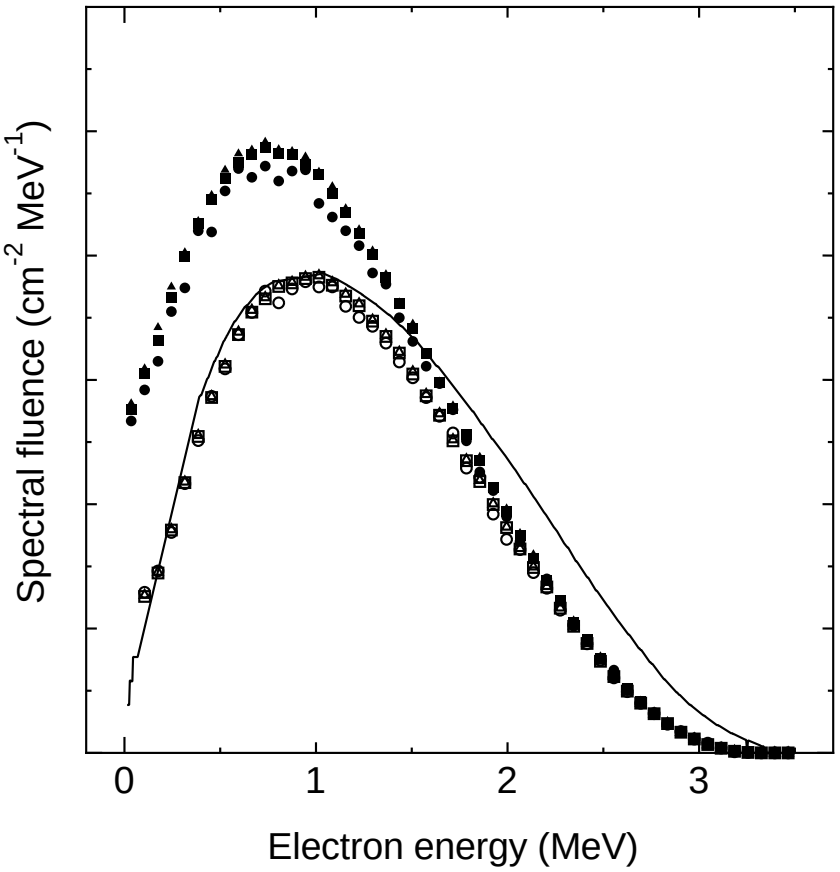


**Figure 4.** Electron energy spectra of the reference beta radiation field calculated in this study.
Solid triangle: geometry A with chamber depth 0.2 mm, solid square: geometry A with chamber depth 0.5 mm, solid circle: geometry A with chamber depth 1.5 mm, open triangle: geometry B with chamber depth 0.2 mm, open square: geometry B with chamber depth 0.5 mm, open circle: geometry B with chamber depth 1.5 mm. The solid curve in (a) refers the electron energy spectrum from a planar Ru-106 source with a window thickness of 50 mg/cm$^2$ and measurement distance of 10 cm [10].

# EVALUATION OF EYE SHIELDS IN ELECTRON BEAM TREATMENT USING MONTE CARLO SIMULATION

**Y. Nakajima[1], N. Kadoya[1], S. Dobashi[1], K. Kishi[2], K. Sato[2], K. Takeda[1], K. Jingu[1]**

*[1]Department of Radiation Oncology, Tohoku University School of Medicine,*
*1-1 Seiryo-machi, Aoba-ku, Sendai, 980-8574, Japan*
*[2]Radiation Technology, Tohoku University Hospital, 1-1 Seiryo-machi, Aoba-ku, Sendai, 980-8574, Japan*
*e-mail: y.nakajima@med.tohoku.ac.jp*

**Abstract**

In electron radiotherapy for the periorbital region, metallic eye shields are used to protect the lens of the eye. Currently used eye shields are made of lead or tungsten. However, there has been little investigation of effective materials and appropriate thickness of the eye shield for protecting the lens and backscattered dose enhancement from the eye shield for each beam energy is not clear. The purpose of this study was to investigate the effectiveness of eye shields for attenuating the beam and to evaluate backscattered dose enhancement from the eye shield using an Electron Gamma Shower ver.5 Monte Carlo code system. To calculate both the transmission and the backscatter dose for 4, 6, and 9 MeV, the eye shields were assumed to be made of lead and tungsten of 1 mm and 2 mm in thickness (width: 1 cm×1 cm), which were placed on a virtual water phantom. For attenuation by the eye shield, at 9 MeV, the relative doses to the lens with lead eye shields of 1 mm and 2 mm in thickness were 51.0% and 23.5%, respectively, whereas those with tungsten eye shields of 1 mm and 2 mm in thickness were 33.5% and 7.2%, respectively. For all energies except 4 MeV, similar results were obtained, indicating that the 2 mm tungsten eye shield provided more attenuation than did the other. For 4 MeV, the 1 mm tungsten eye shield provided more attenuation than did the 2mm tungsten eye shield (21.1% vs 25.2%). The reason for this might be the difference in lateral electron scattering between 4 MeV and other energies, and the lens position in the case of the 2 mm eye shield is 1 mm deeper than that in the case of the 1 mm eye shield. For backscatter dose caused by the eye shield, dose enhancement was 1.25 to 1.5-times larger than that in the absence of eye shields, and lower beam energy caused larger dose enhancement. These results suggested that coating of that eye shield with low atomic number materials is needed to reduce the dose enhancement from backscattered electrons, especially at lower beam energy. In conclusion, in this study, tungsten was shown to be a better material for the eye shield, and optimal thickness of the eye shield might depend on the beam energy.

## 1. Introduction

Tumors that involve the eyelid, such as sebaceous gland carcinoma, squamous cell carcinoma, mucosa-associated lymphoid tissue (MALT) lymphoma, and total skin electron beam therapy for mycosis fungoides, require radiotherapy of the periorbital region using high energy electrons [1-3]. Although electron beam therapy can be used for treating superficial tumors (< 5 cm) [4] due to dose uniformity in the target volume and in minimizing dose to deeper tissue, in the periorbital region, it is a matter of radiation dose to critical organs such as the lens (Figure 1). Therefore, for this treatment, an eye shield is inserted in the eyelid and cornea to protect the lens and cornea and to reduce adverse events

such as the formation of cataracts.

Most of the commercially available shields are made of lead (Pb) or tungsten (W). The density and atomic number of lead are 11.34 g/cm$^3$ and 82, respectively. Tungsten has a higher density (19.3 g/cm$^3$) and lower atomic number (74). Some studies have shown dose characteristics of electron beams with lead and tungsten [5-7]. For study focusing on eye shields, dosimetric evaluation of eye shields with consideration of backscattered electrons in electron beam treatment has been carried out [8], but evaluation of eye shields using Monte Carlo simulation has been rare.

Clinically, to protect the lens from an electron beam, a rigorously designed eye shield is needed. This is because if the eye shield is not suitable for protection, a cataract will form in the lens due to the transmission of an electron beam. Additionally, backscattered dose enhancement from the eye shield causes adverse events near the eyelid (e.g., development of conjunctivitis) [9].

In this study, we investigated the optimal thickness and most appropriate materials of an eye shield for 4, 6 and 9 MeV electron beams using Monte Carlo simulation. We also investigated the dosimetric impact of eye shields that induced backscatter dose.

## 2. Materials and Methods

### 2.1 Simulation Geometry

To determine the optimum thickness and material for eye shields, we carried out simulation of lead and tungsten eye shields of 1 mm and 2 mm in thickness (width: 1 cm×1 cm). We set the geometry of the virtual phantom as shown in Figure 2. The virtual phantom was created from a 20 cm×20 cm×4 cm rectangular water containing a central 1 cm×1 cm×0.1 cm high density region of the eye shield. We assumed 1 mm from the phantom surface, to simulate thickness of the eyelid, followed by a flat piece of either lead or tungsten, followed by a 0.5 mm cornea, followed by a 3 mm anterior chamber, followed by a 4 mm lens. The densities of lead and tungsten were 11.34 and 19.3 g/cm$^3$, respectively.

### 2.2 Calculation condition

All simulations were performed using an Electron Gamma Shower ver.5 Monte Carlo code system. The incident electron beam energies were 4, 6 and 9 MeV. The irradiation field was 6 cm×6 cm, and the distance from the beam source to the surface of the phantom (SSD) was 100 cm. The dose was scored in 2 mm×2 mm×0.5 mm voxels down the central axis. The cutoff energies were set to 10 keV for electrons and 521 keV for photons. The number of photons was $6\times10^8$, and statistical error in center of the phantom ranging from the beam entrance surface to the lens was less than 3.0%.

### 2.3 Evaluation of the lens dose and shielding effect

The dose profile data were taken through the center of the phantom. The profile data were normalized to maximum dose of the water phantom without the eye shield. For shielding capability of each case, dosimetric parameters including maximum dose ($D_{max}$) and mean dose ($D_{mean}$) of the lens were evaluated. $D_{max}$ and $D_{mean}$ were used to determine optimum eye shields for each beam energy.

The transmission and backscatter of eye shields were evaluated by dose correction factor (CF) [10]. CF can be defined as the ratio of dose at the interface of eye shields ($D_i$) and the dose at the same point in a water phantom ($D_h$), according to the equation:

$$CF = D_i / D_h, \qquad (1)$$

CF can be separated into two components: forward dose perturbation factor (FDPF) on the exit side of the eye shields, and backscatter dose perturbation factor (BSDF) [11] at the entrance side of the eye shields.

In this study, FDPF and BSDF were used to evaluate transmission through eye shields and backscatter dose enhancement, relatively.

## 3. Results and discussions

### 3.1 Evaluation of shielding capability

Figure 3 shows the results of comparison of the dose profile data for lead and tungsten eye shields of 1 mm and 2 mm in thickness. The profile data were taken through the center of the phantom. In addition, $D_{max}$ and $D_{mean}$ of the lens are summarized in Table 1. For attenuation by the eye shield, at 9 MeV, the relative doses to the lens with 1 mm and 2 mm lead eye shields were 51.0% and 23.5%, respectively, whereas those of the lens with 1 mm and 2 mm tungsten eye shields were 33.5% and 7.2%, respectively. From the perspective of lens dose, for 6 MeV and 9 MeV were obtained similar result that the 2 mm thickness of tungsten provided more attenuation than the other eye shields. For 4 MeV, 1 mm tungsten eye shield is an optimal eye shield because the mean dose of the lens is lower than that in the case of the 2 mm tungsten eye shield (21.1% vs 25.2%), but the value of FDPF were almost the same for the lead eye shield of the tungsten eye shields of 1 mm and 2 mm in thickness: 0.07, 0.09, and 0.06, respectively (Table 2). This is thought that in the case of a relatively low energy electron beam such as 4 MeV, electrons are scatted more easily and through larger angles [12], and lens dose in the case of a 2 mm eye shield is more affected by lateral electron scatter than is lens dose in the case of a 1 mm eye shield because the lens position is 1 mm deeper than 1 mm eye shield case. Therefore, when a low energy beam is used, although eye shields can reduce the dose, dose deposition of the lens is expected due to lateral scatter from outside of the eye shields (Figure 4). For 6 MeV and 9 MeV, the effect of eye shield thickness is small because there is little lateral scattering of electrons.

Although the tungsten eye shield of 2 mm in thickness has high shielding capability since FDPF was less than 0.15 for all energies, the mean doses of the lens differed depending on the beam energy: 25.2% at 4 MeV, 11.1% at 6 MeV and 7.2% at 9 MeV. Therefore, the effectiveness of eye shields was affected by the beam energy.

### 3.2 Backscatter dose caused by eye shield

Values of BSDF are summarized in Table 3. For 4 MeV, BSDF was approximately 1.5. This result indicated that half again dose enhancement occurred due to electron backscatter on front surface of the eye shield. Similar backscatter effects were seen for 6 and 9 MeV. However, it appears the beam energy was higher to lower BSDF, ranging from 1.20 to 1.39. The results are consistent with the results of a previous study, showing dosimetric evaluation of backscatter dose for eye shields [8]. In additionally, the effect of material and thickness was appeared for lower beam energy. Therefore, this result suggested that protector was needed to cover the normal tissue due to backscatter dose to eyelid is reduce, especially lower beam energy.

## 4. Conclusions

In this study, the optimal material and optimal thickness for eye shields used in electron beam therapy for attenuating the beam to an acceptable amount for each beam energy were determined. The results showed that tungsten is a better material for an eye shield and that the thickness of eye shield required to attenuate the beam was different for each beam energy. For electron beam energy of 4 MeV, a tungsten eye shield of 1 mm in thickness is an effective eye shield, and for 6 MeV, a tungsten eye shield of 2 mm in thickness is an effective eye shield. Tungsten is a better material for an eye shield, and the optimal thickness of the eye shield might depend on the beam energy.

Additionally, dose enhancement on the upstream eyelid occurred due to backscattered electrons from the eye shield. The backscattered dose enhancement is half as large again as the absence of eye shields at a maximum (4 MeV, lead). The backscattered dose enhancement also depended on each beam energy, and lower beam energy caused larger dose enhancement. The results suggested that coating of the eye shield with low atomic number materials is needed to reduce dose enhancement from the backscattered electrons, especially for a lower beam energy.

## References


1) N. Tomita, T. Kodaira, H. Tachibana, T. Nakamura, N. Mizoguchi, and A. Takada, “Favorable outcomes of radiotherapy for early-stage mucosa-associated lymphoid tissue lymphoma.” Radiotherapy and Oncology **90.2**, 231-235 (2009).
2) H. Yamashita, K. Nakagawa, T. Asari, N. Murakami, H. Igaki, and K. Ohtomo, “Radiotherapy for 41 patients with stages I and II MALT lymphoma: a retrospective study.” Radiotherapy and Oncology **87.3**, 412-417 (2008).
3) P. Zhou, A. K. Ng, B. Silver, S. Li, L. Hua, and P. M. Mauch, “Radiation therapy for orbital lymphoma,” Int. J. Radiat. Oncol., Biol., Phys. **63**, 866–871 (2005).
4) F. M. Khan, The Physics of Radiation Therapy, 4th ed. (Lippincott Williams & Wilkins, Philadelphia, 2010).
5) I. J. Das, C. Cheng, R. K. Mitra, A. Kassaee, Z. Tochner, and L. J. Solin, “Transmission and dose perturbations with high-Z materials in clinical electron beams,” Med. Phys. **31**, 3213–3221 (2004).
6) J. C. L. Chow and G. N. Grigorov, “Monte Carlo simulation of backscatter from lead for clinical electron beams using EGSnrc,” Med. Phys. **35**, 1241–1250 (2008).
7) S. Sathiyan, M. Ravikumar, and S. S. Supe. “Measurement of backscattered dose at metallic interfaces using high energy electron beams.” Reports of Practical Oncology & Radiotherapy **11.3**, 117-121 (2006).
8) R. D. Weaver, B. J. Gerbi, and K. E. Dusenbery, “Evaluation of eye shields made of tungsten and aluminum in high-energy electron beams,” Int. J. Radiat. Oncol., Biol., Phys. **41**, 233–237 (1998).
9) K. Isobe, Y. Kagami, K. Higuchi, T. Kodaira, M. Hasegawa, N. Shikama, M. Nakazawa, I. Fukuda, K. Nihei, K. Ito, T. Teshima, Y. Matsuno, and M. Oguchi, “A multicenter phase II study of local radiation therapy for stage IEA mucosa-associated lymphoid tissue lymphomas: a preliminary report from the Japan Radiation Oncology Group (JAROG).” Int. J. Radiat. Oncol., Biol., Phys. **69.4**, 1181-1186 (2007).
10) C. Reft et al., “Dosimetric considerations for patients with HIP prostheses undergoing pelvic irradiation. Report of the AAPM Radiation Therapy Committee Task Group 63,” Med. Phys. **30**, 1162–1182 (2003).
11) I. J. Das and F. M. Khan, “Backscatter dose perturbations at high atomic number interfaces in megavoltage photon beams,” Med. Phys. **16**, 367–375 (1989).
12) W. Strydom, W. Parker, and M. Olivares. "Electron beams: physical and clinical aspects." Podgorsak EB (edn) Radiation oncology physics: a handbook for teachers and students. International Atomic Energy Agency (IAEA), Vienna, 273-299, (2005).

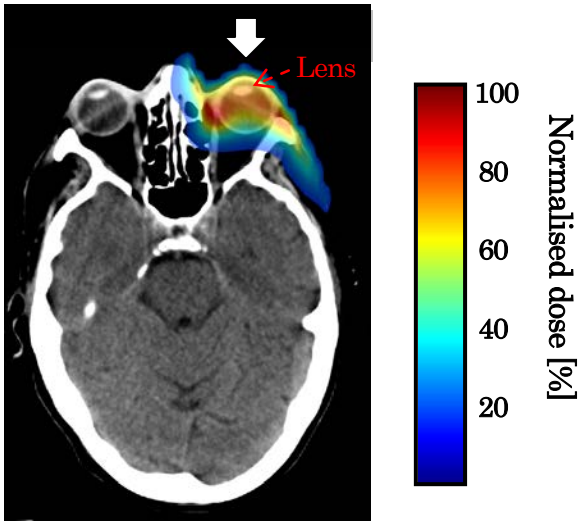


**Figure 1.** Example axial CT image with dose distribution (Energy = 6 MeV, Field size =10 cm×10 cm) for electron beam therapy of the periorbital region without an eye shield. The calculation algorithm was pencil beam algorithm (XiO, Elekta CMS Inc., Maryland Heights, MO). The radiation field is indicated by white arrow.

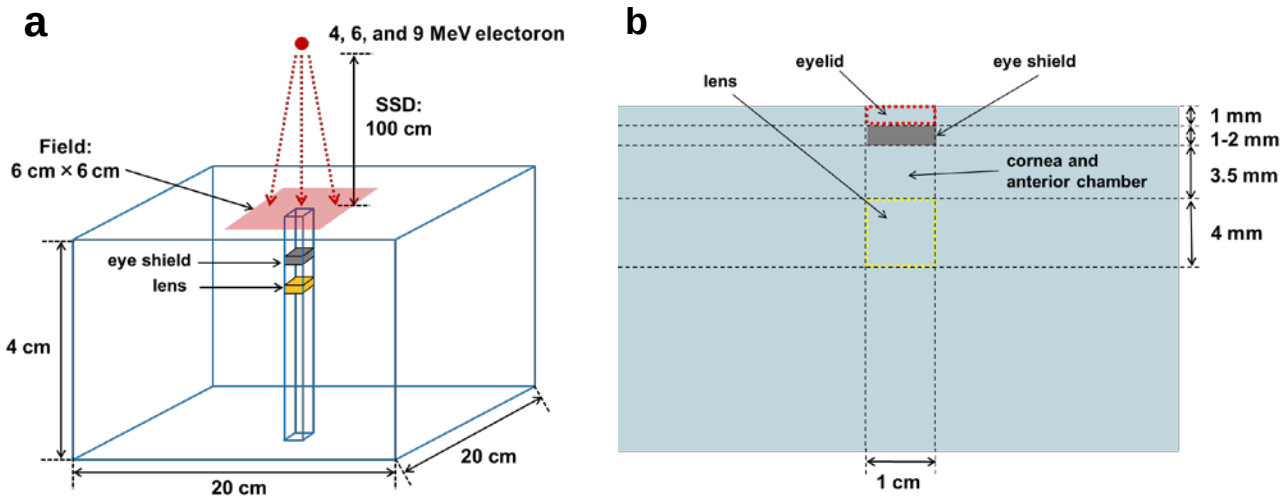


**Figure 2.** Geometry used to calculate the dose profile curves with eye shield. (a) Schematic of virtual phantom. (b) Schematic of cross-section of virtual phantom.

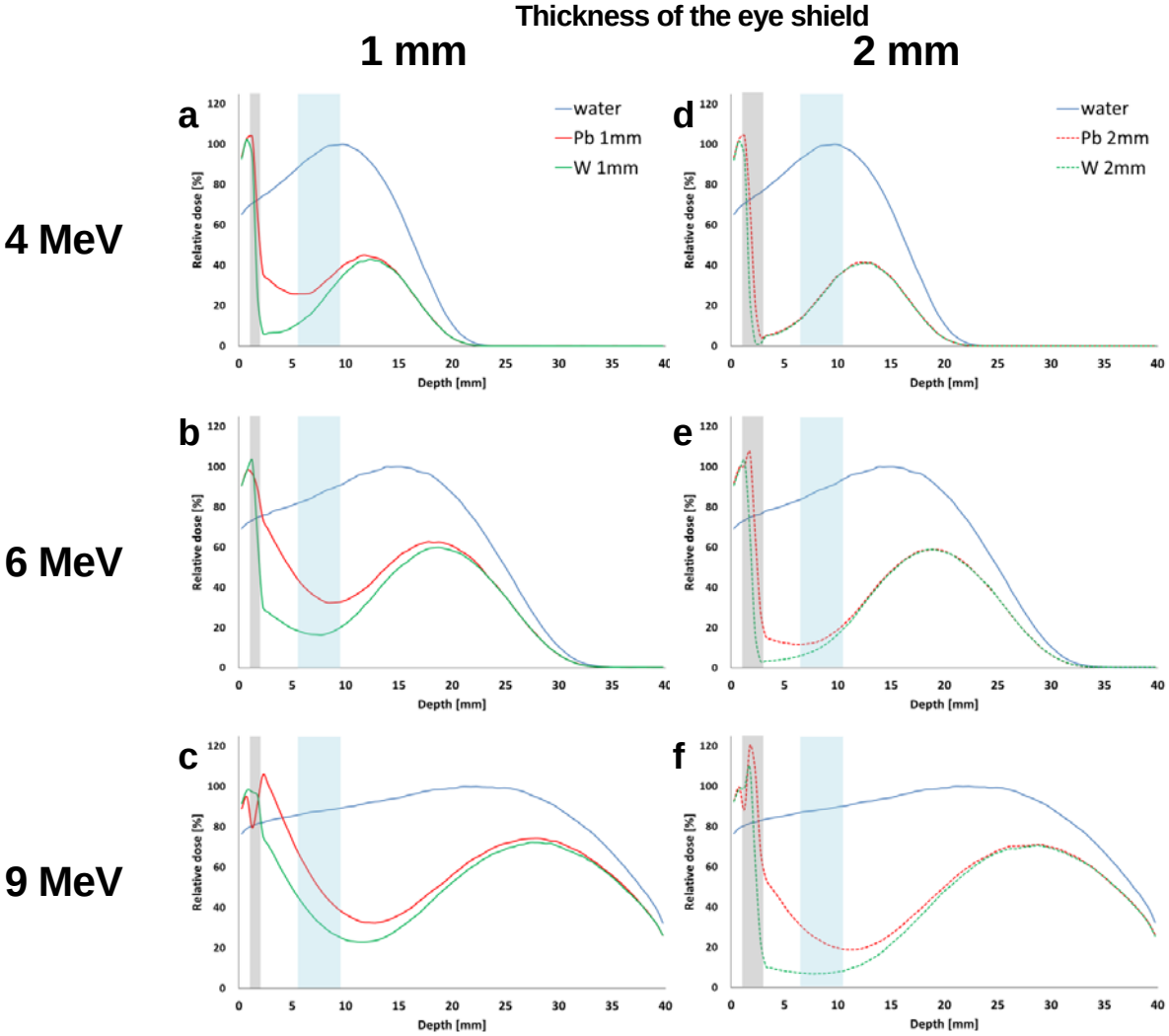


**Figure 3.** Central axis dose profile curves that were normalized by the maximum dose without the eye shield in the water phantom for three energies and four eye shields (two materials and two thicknesses). Gray background color represents an eye shield and blue background color represents lens. Cornea and anterior chamber are existed between eye shield and lens. The beam energies are 4 MeV for (a, d), 6 MeV for (b, e) and 9 MeV for (c, f). (a-c) is for 1 mm and (d-f) is for 2 mm for the thickness of eye shields.

**Table 1.** Maximum and mean lens dose for different eye shield cases for 4, 6, and 9 MeV.

| Material | Thickness (mm) | Energy (MeV) and lens dose (%) | | | | | |
|---|---|---|---|---|---|---|---|
| | | 4 | | 6 | | 9 | |
| | | $D_{max}$ | $D_{mean}$ | $D_{max}$ | $D_{mean}$ | $D_{max}$ | $D_{mean}$ |
| Lead | 1 | 37.5 | 30.2 | 42.2 | 35.5 | 65.1 | 51.0 |
| | 2 | 35.8 | 25.7 | 19.9 | 14.6 | 29.6 | 23.5 |
| Tungsten | 1 | 31.8 | 21.1 | 19.2 | 17.2 | 43.6 | 33.5 |
| | 2 | 35.8 | 25.2 | 17.9 | 11.1 | 8.0 | 7.2 |

**Table 2.** FDPF for different eye shield cases for 4, 6, and 9 MeV.

| Material | Thickness (mm) | Energy (MeV) 4 | 6 | 9 |
|---|---|---|---|---|
| Lead | 1 | 0.48 | 0.98 | 1.29 |
| | 2 | 0.07 | 0.20 | 0.65 |
| Tungsten | 1 | 0.09 | 0.40 | 0.92 |
| | 2 | 0.06 | 0.04 | 0.12 |

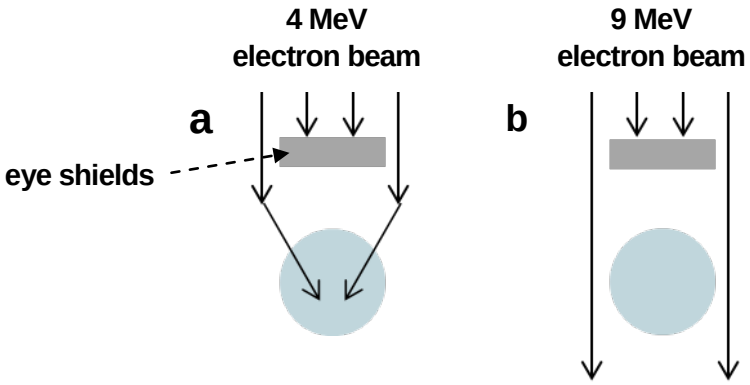


**Figure 4.** The difference in lateral scatter of electron due to beam energy. (a) It is in the presence of lateral scattering due to lower beam energy. (b) It is in the absence of lateral scattering due to higher beam energy.

**Table 3.** BSDF for different eye shield cases for 4, 6, and 9 MeV.

| Material | Thickness (mm) | Energy (MeV) 4 | 6 | 9 |
|---|---|---|---|---|
| Lead | 1 | 1.50 | 1.37 | 1.20 |
| | 2 | 1.50 | 1.39 | 1.26 |
| Tungsten | 1 | 1.49 | 1.37 | 1.24 |
| | 2 | 1.48 | 1.37 | 1.25 |

# DESIGNING PROTECTIVE STENTS FOR ELECTRON RELEASE FROM DENTAL RESTORATIONS IN EXTERNAL RADIOTHERAPY USING MONTE CARLO SIMULATION

**Masahide Saito, Noriyuki Kadoya, Suguru Dobashi, Ken Takeda, and Keiichi Jingu**

*Department of Radiation Oncology, Tohoku University School of Medicine,*
*Sendai 980-8574, Japan*
*e-mail: m.saito@med.tohoku.ac.jp*

**Abstract**

In external radiotherapy for head and neck cancer, it is possible that some patients have metal dental materials. In this situation, a critical problem is that electronic backscatter from the upstream surface of these materials may damage the surrounding soft tissue. The purpose of this study was to determine the impact of electronic backscatter from dental materials with high-energy external X-ray irradiation and also to determine the optimal thickness of a protecting device (PMMA) for preventing its effect by using EGS5 Monte Carlo simulation. First, four high-energy X-rays (4, 6, 10, and 15 MV) and five dental materials (three metals and two ceramics) of 1 x 1 x 0.2 $cm^3$ were used to investigate the impact of electronic backscatter from dental materials and also to investigate the correlation between these impacts and X-ray energies. Then, based on these results, optimal thickness of protective PMMA was investigated. Results of 6 MV and 10 MV, backscatter effects from the surfaces of dental materials (1 mm distance) caused increases of up to 132.1% and 134.6% (gold-silver-palladium alloy), and 141.7% and 146.2% (Metal-ceramic-gold alloy) of the simulation without dental material, respectively. Shielded with a 3 mm PMMA, these effects reduced to 101.4% and 104.4% (gold-silver-palladium alloy), and 102.5% and 106.7% (metal-ceramic-gold-alloy) respectively. The results showed that the impact of electronic backscatter was greater for materials with higher Z. The impact of electronic backscatter was also greater when X-ray energy was increased. Therefore, in order to protect soft tissue from the impact of electronic backscatter, it is necessary to make an optimal protective material according to patient-specific treatment.

## 1. Introduction

Due to the development of irradiation technology such as intensity-modulated radiotherapy (IMRT) [1] and volumetric modulated arc therapy (VMAT) [2, 3], it has become possible to reduce the dose to organs at risk (OAR) while increasing the dose to tumors. The development of these new techniques has resulted in increasing use of external radiotherapy for head and neck cancer. VMAT has been increasingly used due to its lower total MUs and comparable dose distribution [4, 5]. However, if there are metallic structures such as dental restorations in the radiation field, some critical problems may arise.

The first problem may occur during treatment planning. Metallic structures can severely attenuate diagnostic X-rays, and due to the occurrence of artifacts from metal dental materials, it becomes difficult to obtain accurate CT values [6]. Convolution/superposition dose calculation algorithms equipped in commercialized treatment planning systems (TPS) need to transform CT values to electron-density ratios. Therefore, artifacts from metal dental materials can make accurate dose calculation difficult. In order to prevent these effects, it is necessary to make a treatment plan avoiding the area containing metal dental materials as much as possible. However, a novel dose calculation algorithm that

solves the linear Boltzmann transport equation for fluence everywhere inside the volume of interest has recently been released [7] and has been shown to perform as well as Monte Carlo methods for dose calculation involving high-density volumes [8].

Another problem may occur during the actual treatment. When radiation is properly used, side effects cannot be completely eliminated because of the presence of multiple critical tissues and organs and the various pathways by which tumors spread [9]. However, if dental materials are included, a critical problem is that electronic backscatter from the upstream surface of these materials may damage the surrounding soft tissue. Additionally, because the above-mentioned convolution/superposition algorithms are not designed to deal with an atomic number (Z), the electronic backscatter effect from high-Z materials such as metal dental materials may be underestimated. Although the most reliable way is to remove the dental materials, protective devices can be used to protect the surrounding healthy tissue [9, 10]. It was reported that soft tissue could be effectively shielded with a PMMA stent of at least 3 mm in thickness in the case of 6MV X-ray [10]. However, such studies have been limited, and more dental materials and X-ray energies that are used in a clinical setting must be investigated.

The purpose of this study was to determine the impact of electronic backscatter from dental materials with high-energy external X-ray irradiation and also to determine the optimal thickness of a protecting device (PMMA) for preventing its effect by using EGS5 Monte Carlo simulation. This study was conducted with the assumption of external radiotherapy for the head and neck region, and we quantified the impact of electronic backscatter by using four X-ray energies and five dental materials.

## 2. Materials and Methods

### 2.1 Dental materials

Table 1 shows details of dental materials selected for this study. In clinical situations, two main types of dental materials (metals and ceramics) are used. In this study, three metal dental materials (titanium, gold- silver-palladium alloy (Castwell M.C.12, GC cop, Tokyo, Japan) and metal ceramic gold alloy (KIK, Ishifuku Metal Industry Co, Nagoya, Japan)) and two ceramics (zirconia and porcelain) were used. In Japan, 12%Au-Ag-Pd alloys such as Castwell M.C.12 are commonly used in clinical dental restorations because these alloys are covered by health insurance. The two metal alloy materials were high-Z and high physical density materials, and the two ceramics were used for comparison with these metals.

### 2.2 Geometries

A 30 x 30 x 30 $cm^3$ solid water phantom with a 1 x 1 x 0.2 $cm^3$ insert of dental material at 5 cm in depth in the central axis of the phantom was used (Fig. 1). Firstly, in order to investigate backscatter effects from dental materials, 5 dental materials shown Table 1 were used in the phantom. Secondly, a PMMA (physical density of 1.19 $g/cm^3$ and effective Z of 9.49) of 1 x 1x 0.2~0.6 $cm^3$ in size was set in front of two dental materials (KIK and Castwell M.C.12) in order to investigate protective effects of the PMMA device. The reason of selecting two metals was that these two materials were high-Z materials and were expected to have a great impact of electron release.

### 2.3 EGS5 Monte Carlo simulation

EGS5 Monte Carlo code was used in this study. Simulation was first done with four X-ray energies (4, 6, 10, and 15 MV) and then with two X-ray energies (6 MV and 10 MV, which are commonly used for the head and neck region). Photon beam spectra with linear accelerators of Varian Medical Systems (Palo Alto, CA) were used [11]. All beams were simulated in a 10 x 10 $cm^2$ field size and 100 cm source-to-surface distance (SSD) (Fig. 1). Additionally, each calculation was done using a dose grid with 1 mm resolution in the direction of depth with cut-off energies ECUT=0.521 MeV and PCUT=0.01 MeV and performed to 1% variance on the central beam.

# 3. Results

## 3.1 Dose profile curves included dental materials

Figure 2 and Figure 3 show dose profile curves of the central beam axis for four X-rays energies (normalized in max dose depth, called PDD). The dose profile curves in Figure 2 are the results of using three metal dental materials, and those in Figure 3 are the results of using two ceramics. Two specific features were seen from these profiles. One of the features was seen in the upstream surface of dental materials at 5 cm in depth of the phantom. The profile curves obtained by using metals show a sharp backscatter peak in that region, while those obtained by using ceramics show a small peak. Another feature was beam attenuation seen downstream of the dental materials, and this effect of metals was also greater than that of ceramics. These features were seen for all of the beam energy used in this study.

## 3.2 Backscatter effects from dental materials

Different analysis was carried out to determine backscatter effects from dental materials. Figure 4 and Figure 5 shows normalized dose profile curves for four X-ray energies. The relative dose of these profiles was normalized by eq. (1).

$$Relative\ dose = \frac{Dose_{heterogeneous}}{Dose_{homogeneous}} \times 100\ [\%] \quad (1)$$

The central axis of the profiles was the upstream surface of each dental material, and the plotted range was around 8 mm. Dose profile curves in Figure 4 are the results of using three metal dental materials, and those in Figure 5 are the results of using two ceramics, as in Figure 2 and Figure 3. As shown in Figure 3 (b) and (c), backscatter effects from the surfaces of dental materials (1 mm distance) caused increases of up to 113.5% and 114.7% (Ti), 132.1% and 134.6% (Castwell M.C.12), and 141.7% and 146.2% (KIK) of the simulation without a dental material, respectively. In the same manner, as shown in Figure 4 (b) and (c), the effects of inserting ceramics were increases of up to 106.5% and 106% (porcelain) and 119.5% and 121.2% (zirconia), respectively. Table 2 shows the relationship between X-ray energy and backscatter range for two metals that larger backscatter effects in this study. In Table 2, 0% is equal to the case of the simulation without a dental material. The backscatter range was larger X-ray energy. However, over-dose rates were below 10% at 4 mm distance of the surface of two metals.

## 3.3 Optimal thickness of PMMA

Based on the results of [3.2], optimal thickness of protective PMMA was investigated. Thickness of PMMA were used 2 mm – 6 mm. Table 3 shows over-dose rates of two metals for two X-ray energies using protective PMMA. The "over-dose rate" was evaluated at the point seen in the 1 mm upstream surface of PMMA and is shown as 0% in the case of simulation without a dental material. As shown in Table 3, in the case of each dental material, with PMMA of 3 mm in thickness, the over-dose rate was below 5% for 6 MV, and with 4 mm in thickness, the over-dose rate was below 5% for 10 MV. However, in more than 4mm, there was almost no change in the over-dose rate with greater thickness of PMMA.

In order to clarify the effect of the dose calculation grid, additional analysis of the dose calculation grid was done. Figure 4 shows a comparison of the results for a 1 mm grid that was used in this study and the results for a 0.2 mm grid that was used in an additional analysis (in the case of using 6 MV X-ray and inserting PMMA of 3 mm in thickness in front of Castwell M.C.12). On the surface of the dental material, the profile using the 0.2 mm grid shows a sharp backscatter peak (147.6%), while that using the 1 mm gird shows a small peak (125.4%). However, at a distance of 3 mm, there was almost no difference between the two profile curves.

## 4. Discussion

In this study, we evaluated the backscatter effect from dental materials using EGS5. For 6 MV X-ray, the backscatter effects on the surfaces of metal dental materials caused a maximum increase of up to 142.7% of the simulation without a dental material (KIK, 1 mm distance), while there was only a small for ceramics (increase up to 106.5% for porcelain). Thus, the results showed that the impact of electronic backscatter was greater for materials with higher Z. The impact of electronic backscatter was also greater when X-ray energy was increased. In external radiotherapy for head and neck cancer, it is possible that some patients have metal dental materials. This work must be beneficial for the clinical situation because we investigated some sorts of dental material (not only metals, but also ceramics) and X-ray energies (commonly used for head and neck cancer). However, more real situation should be investigated. For example, although we inserted dental materials at a depth of 5 cm in the central axis, an actual depth of a dental material might be different from this value. Additionally, the canceling effect by an opposing beam should also be investigated.

We also evaluated the optimal thickness of PMMA for preventing electronic backscatter effects. To reduce the effect to 5%, optimal thickness of PMMA was 3 mm (6 MV) or 4 mm (10 MV). These results are in accordance with the results of previous study showing that the use of a protective stent at least 3 mm thick, regardless of the restoration material used, effectively reduced the radiation overdose for 6 MV [9]. Additionally, our study revealed that the higher the X-ray energy was, the greater the thickness of the PMMA was required. Although the effect of the dose calculation grid was greater on the surfaces of dental materials, there was almost no difference of a distance of 3 mm. Therefore, our results for optimal thickness of protective PMMA are reasonable.

## 5. Conclusions

The purpose of this study was to determine the backscatter effect from dental materials by irradiating high-energy external X-ray irradiation and also to determine the optimal thickness of a protecting device (PMMA) for preventing its effect, using EGS5 Monte Carlo simulation. We showed a correlation between Z or X-ray energy and the impact of electronic backscatter. We also showed that the backscatter effect of dental materials could be effectively shielded with PMMA of at least 3 mm in thickness. However, in order to protect soft tissue from the impact of electronic backscatter, it is necessary to make an optimal protective material according to patient-specific treatment.

## References


1) S. Webb, Intensity Modulated Radiation Therapy (Institute of Physics Publishing, Bristol, UK, 2001).
2) Yu C X "Intensity-modulated arc therapy with dynamic multileaf collimation: an alternative to tomotherapy," Phys. Med. Biol. 40, 1435-1449 (1995).
3) Otto K. "Volumetric modulated arc therapy: IMRT in a single gantry arc," Med Phys, 35(1), 310-7 (2008).
4) Verbakel W F, Cuijpers J P, Hoffmans D, Bieker M, Slotman B J and Senan S "Volumetric intensity-modulated arc therapy versus conventional IMRT in head-and-neck cancer: a comparative planning and dosimetric study," Int. J. Radiat. Oncol. Biol. Phys. 74, 252-259 (2009).
5) Doornaert P, Verbakel W F, Bieker M, Slotman B J, and Senan S "RapidArc planning and delivery in patients eith locally advanced head-and-neck cancer undergoing chemoradiotherapy," Int. J. Radiat. Oncol. Biol. Phys. 79, 429-435 (2010).
6) Zhao S, Robertson D D, Wang G, Whiting B and Bae K T "X-ray CT metal artifact reduction using wavelets: an application for imaging total hip prostheses," IEEE Trans. Med. Imaging. 19, 1238-1247 (2000).
7) K. Bush, I. M. Gagne, S. Zavgorodni, W. Ansbacher, and W. Beckham "Dosimetric validation of Acuros® XB with

Monte Carlo methods for photon dose calculations," Med Phys, 38(4), 2208-2221 (2001).
8) S. A. M. Lloyd, W. Ansbacher "Evaluation of an analytic linear Boltzmann transport equation solver for high-density inhomogeneities," Med Phys, 40(1), 011707-1-5, (2013).
9) Kaanders JH, Fleming TJ, Ang KK, Maor MH, Peters LJ "Devices valuable in head and neck radiotherapy" Radiat Oncol Biol Phys 23(3), 639-645 (1992).
10) B Reitemeier at el, "Evaluation of a device for attenuation of electron release from dental restorations in a therapeutic radiation field," J Rrosthet Dent. 87, 323-327 (2002).
11) Daryoush Sheikh-Bagheria and D. W. O. Rogers, "Monte Carlo calculation of nine megavoltage photon beam spectra using the BEAM code," Med. Phys. 29, 391-402, (2002).

**Table 1.** Details of five dental materials used in this study.

| Material | Effective Z | Physical density (g $cm^{-3}$) | Composition (wt%) |
|---|---|---|---|
| porcelain | 12.5 | 2.9 | $SiO_2$ (65.5), $Al_2O_3$ (14.1), $K_2O$ (9.6), $Na_2O$ (6.5), CaO (1.8), $Li_2O$ (1.2), MgO (1.2) |
| titanium | 22 | 4.5 | Ti (100) |
| zirconia | 35.7 | 5.6 | $ZrO_2$ (100) |
| gold-silver-palladium alloy (Castwell M.C.12) | 52.8 | 11.5 | Ag (46), Pd (20), Cu (20), Au (12), Zn (0.6), In (0.6), Sn (0.6) |
| metal-ceramic-gold alloy (KIK) | 76.8 | 17.6 | Au (85.5), Pd (8), Pt (4), Ag (0.6), In (0.6), Sn (0.6), Ir (0.6) |

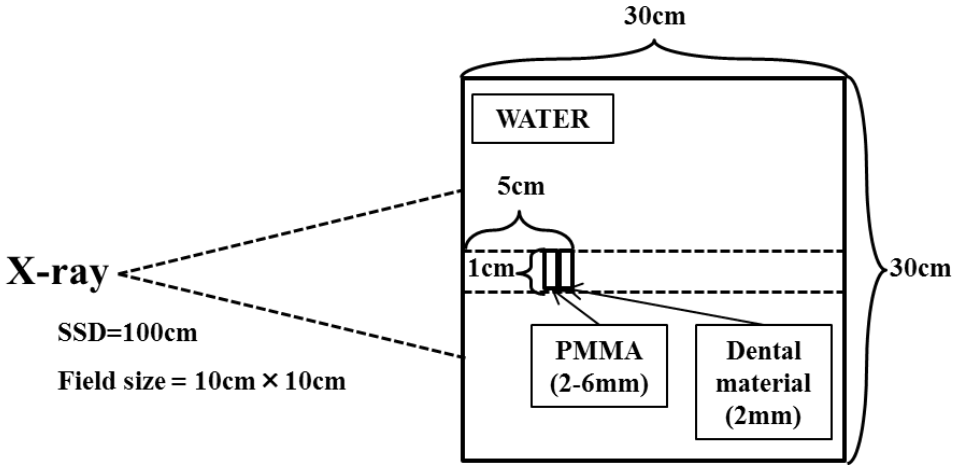


**Figure 1.** A schematic design of Monte Carlo simulation.

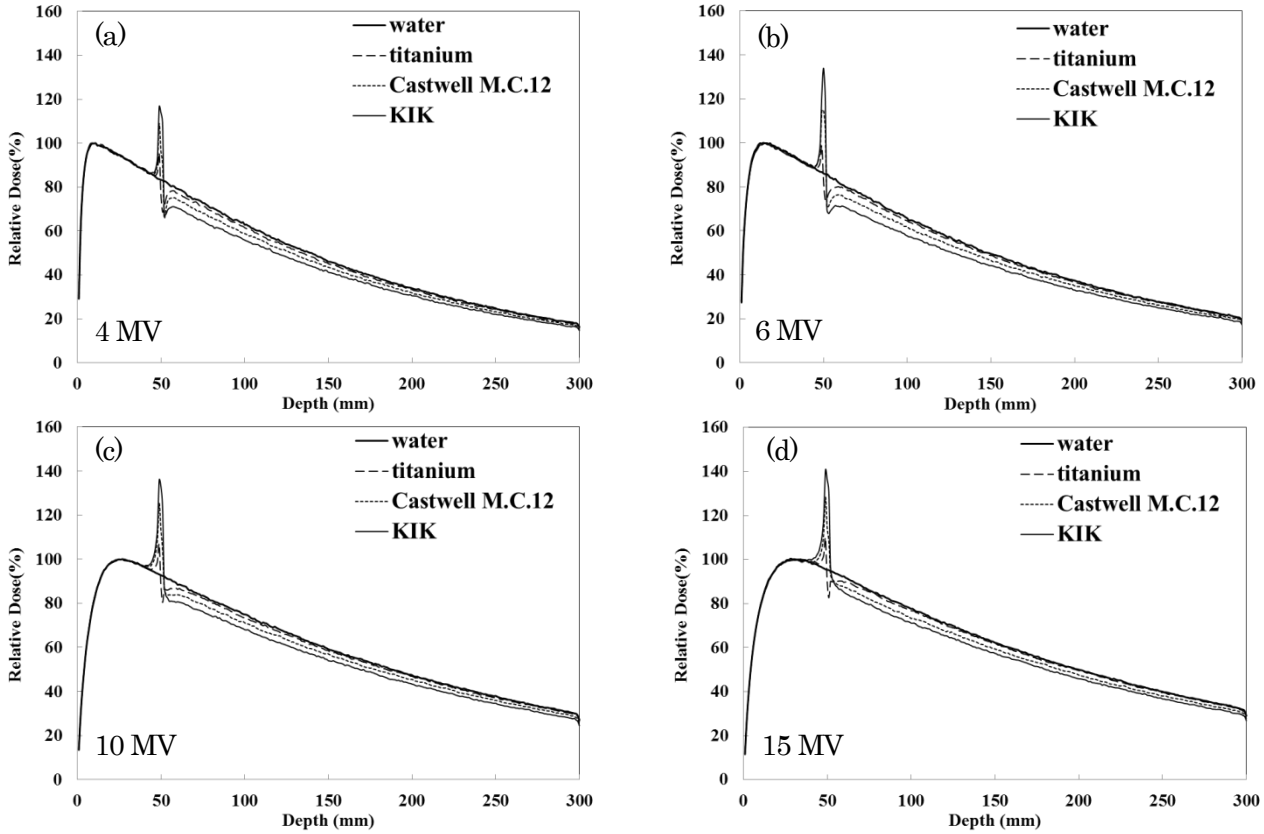


**Figure 2.** Dose profile curves of three metals for four X-ray energies.

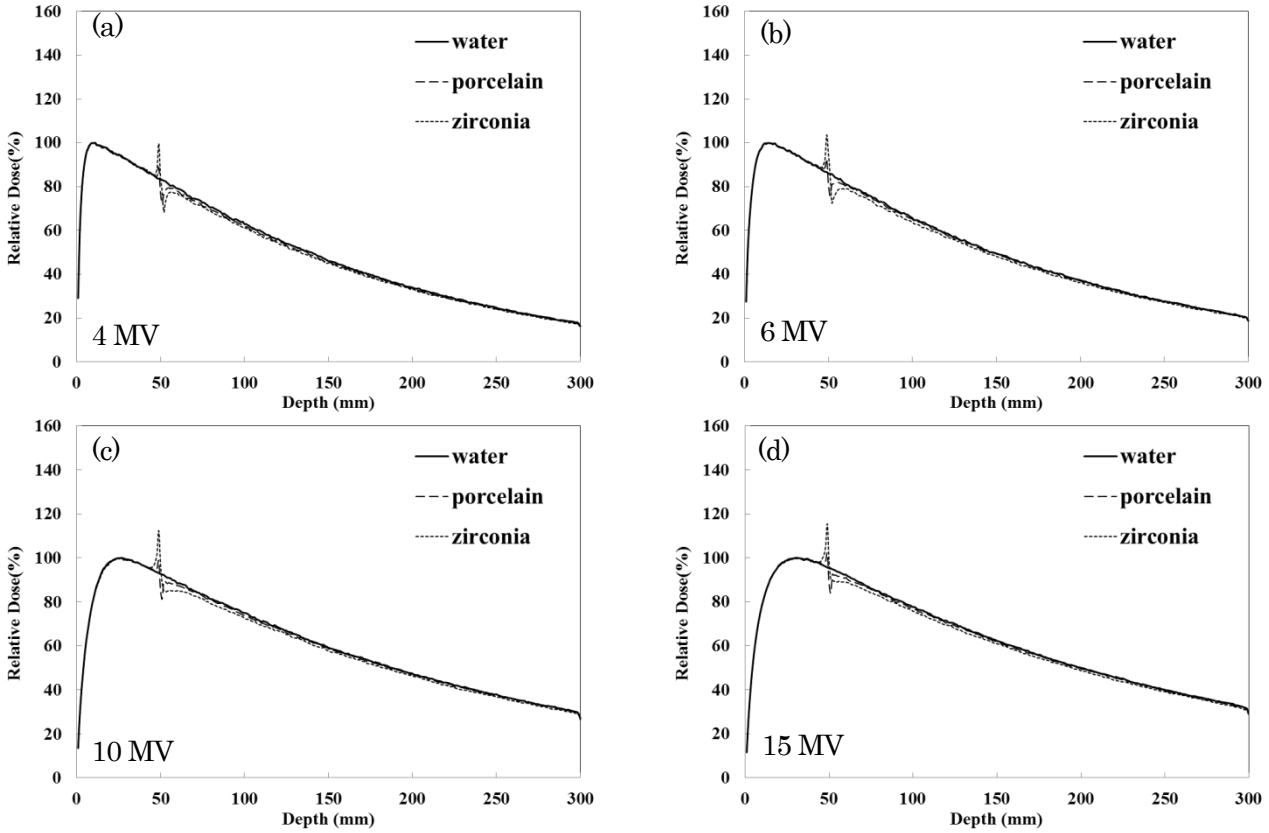


**Figure 3.** Dose profile curves of two ceramics for four X-ray energies.

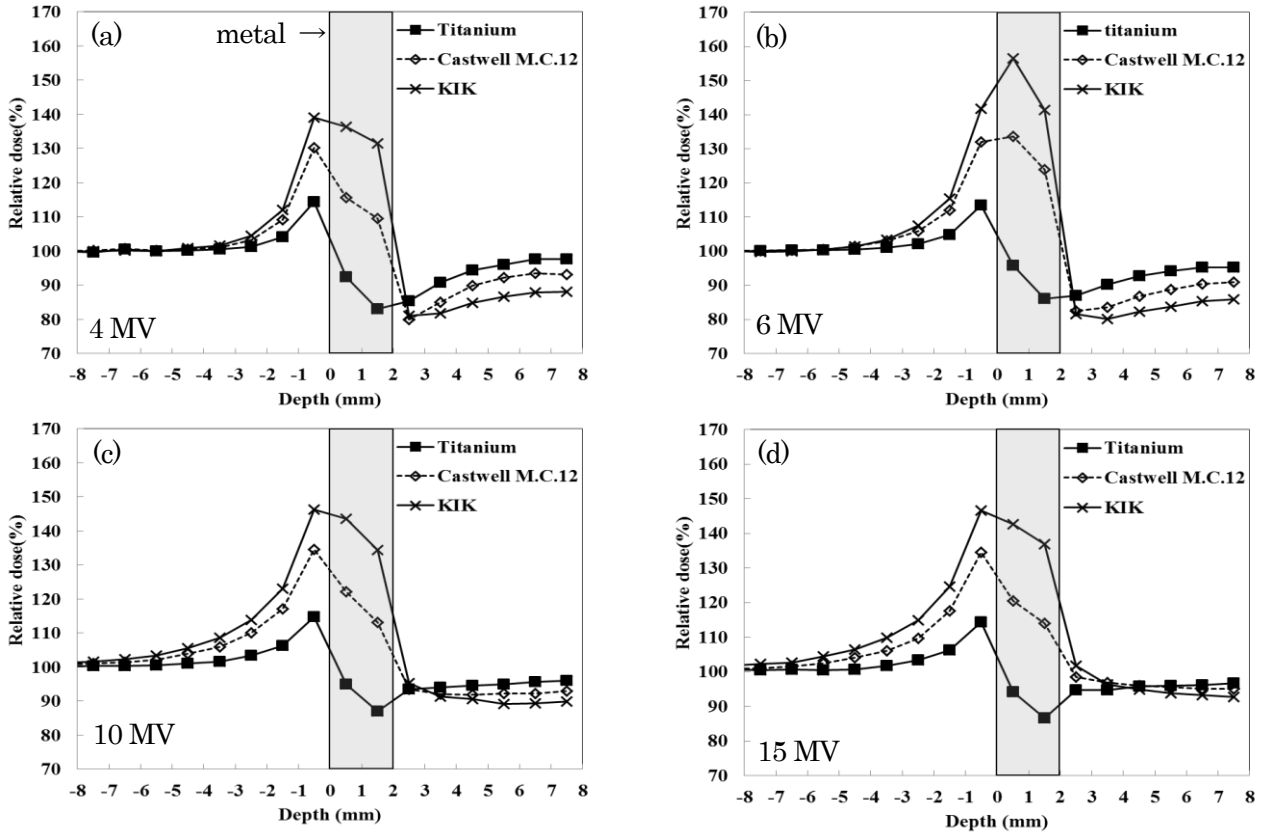


**Figure 4.** Normalized dose profile curves of three metals for four X-ray energies.

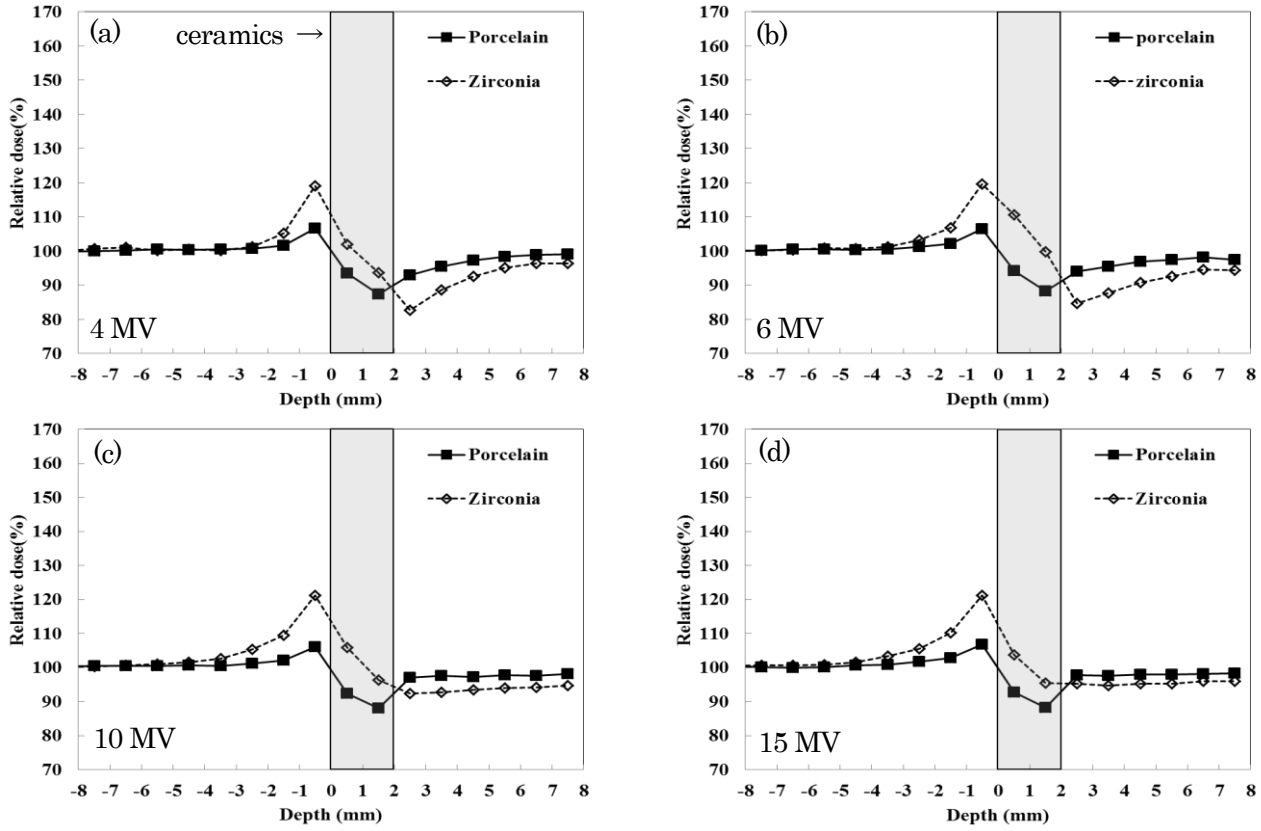


**Figure 5.** Normalized dose profile curves of two ceramics for four X-ray energies.

**Table 2.** The relationship between X-ray energy and backscatter range for two metals.

| Metal dental material | Distance from surface of metal dental material (mm) | Over-dose rate(%) | | | |
|---|---|---|---|---|---|
| | | 4MV | 6MV | 10MV | 15MV |
| KIK | 0 - 1 | 39.1 | 41.7 | 46.2 | 46.6 |
| | 1 - 2 | 12.0 | 15.4 | 22.9 | 24.6 |
| | 2 - 3 | 4.5 | 7.5 | 13.8 | 14.9 |
| | 3 - 4 | 1.6 | 3.3 | 8.6 | 9.8 |
| | 4 - 5 | 0.9 | 1.4 | 5.6 | 6.4 |
| | 5 - 6 | -0.1 | 0.5 | 3.5 | 4.4 |
| | 6 - 7 | 0.2 | 0.0 | 2.3 | 2.7 |
| | 7 - 8 | -0.1 | -0.2 | 1.6 | 2.3 |
| Castwell M.C.12 | 0 - 1 | 30.3 | 32.1 | 34.6 | 34.6 |
| | 1 - 2 | 9.1 | 12.0 | 17.0 | 17.6 |
| | 2 - 3 | 3.3 | 5.9 | 10.0 | 9.7 |
| | 3 - 4 | 1.0 | 2.9 | 5.9 | 6.1 |
| | 4 - 5 | 0.4 | 1.3 | 3.8 | 4.1 |
| | 5 - 6 | 0.2 | 0.5 | 2.1 | 2.5 |
| | 6 - 7 | 0.7 | 0.3 | 1.3 | 1.7 |
| | 7 - 8 | 0.1 | 0.0 | 1.1 | 1.1 |

**Table 3.** Protective effects of PMMA for electron release.

| Metal dental material | Energy of X-rays (MV) | Over-dose rate(%) | | | | |
|---|---|---|---|---|---|---|
| | | PMMA2mm | PMMA3mm | PMMA4mm | PMMA5mm | PMMA6mm |
| KIK | 6 | 6.0 | 2.5 | 0.3 | -0.4 | -0.5 |
| | 10 | 12.1 | 6.7 | 3.9 | 2.1 | 1.4 |
| Castwell M.C.12 | 6 | 4.4 | 1.4 | 0.3 | -0.2 | -0.7 |
| | 10 | 8.7 | 4.4 | 2.2 | 1.3 | 0.8 |

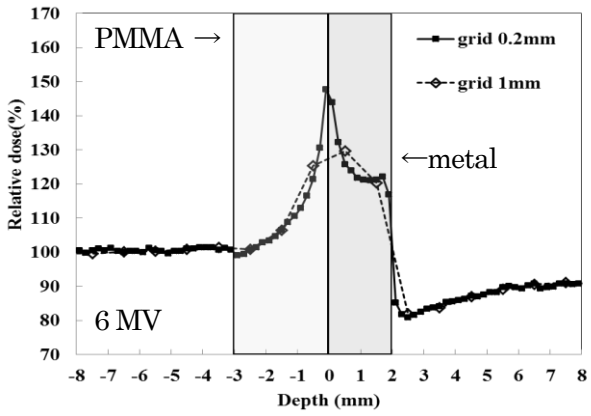


**Figure 6.** Dose profile curves for the comparison between 1 mm grid and 0.2 mm grid.

# EXAMINATION OF THE INFLUENCE OF NUCLIDE INFILTRATION ON AIR AND SURFACE RADIOACTIVITY CONCENTRATIONS ESTIMATED SIMULTANEOUSLY FROM PULSE HEIGHT DISTRIBUTION MEASURED BY NaI(Tl) SCINTILLATION DETECTOR

**J. Hirouchi[1], Y. Terasaka[1], S. Hirao[1], J. Moriizumi[1], H. Yamazawa[1], and Y. Kuwahara[2]**

*[1]Department of Energy Engineering and Science, Graduate School of Engineering, Nagoya University, Nagoya 464-8603, Japan*

*[2]Ibaraki Prefectural Environmental Radiation Monitoring Center, Hitachinaka 311-1206, Japan*

*e-mail: hirouchi.jun@h.mbox.nagoya-u.ac.jp*

**Abstract**

The influence of considering infiltration of nuclides on air and surface radioactivity concentrations estimated simultaneously from NaI(Tl) pulse height distribution was discussed. The activity concentration was determined by comparing the count rates at the full-energy peak ranges between observation and calculation with an electron-photon transport code EGS5. The concentration ratio of air to surface was determined by comparing the count rates at the energy range (120-180 keV). It was shown that the estimated air and surface activity concentrations were more reasonable by considering infiltration of nuclides.

## 1. Introduction

Radioactivity concentrations in environment are essential information for evaluating radiological consequences to the public and formulating proper countermeasures in a nuclear power plant accident. In the Fukushima Dai-ichi nuclear power plant (FDNPP) accident, however, it took a long time to obtain these data.

Pulse height distribution, which is one of essential information in an accident, was measured continuously from the early phase of the FDNPP's accident at many points including monitoring stations (MSs). Recently, several studies aimed at interpolating activity concentration data and providing rapidly the data, and estimated activity concentrations from pulse height distribution [1,2]. These studies reported that the estimated values were in good agreement with the in-situ measurements, indicating the applicability of these estimation methods to a situation where nuclides are distributed uniformly either in air or on a large open ground. However, Hirayama *et al.* [1] pointed out that the estimated concentrations with the method were unreasonable in a situation where nuclides exist both in air and on a ground.

In this study, therefore, the simultaneous estimation of air and surface activity concentrations from pulse height distribution was made. It is known that the ratio of count rate in the full-energy peak part to that in the low-energy part (< 500 keV) corresponding to scattered photons is different depending on location of nuclides. The ratio is smaller as the fraction of the amount of nuclides existing in air is larger, because the path length in air for gamma-ray emitted from nuclides existing in air is relatively longer than that on the ground, which causes the larger number of photons scattered by air. This fact implies that the count rate in the low-energy part can have information on location of nuclides. In this study, the count rate in the low-energy part was used for estimating the ratio of air to surface concentration. Nuclides deposited on the surface can infiltrate into the ground, causing the larger number of photons scattered by soil material. In

consequence, the ratio of count rate in the full-energy peak part to that in the low-energy part can change, and hence the estimated concentrations can vary by considering infiltration of nuclides. In this study, therefore, the influence of infiltration on estimated air and surface concentrations is also investigated.

# 2. Methods

## 2.1 Pulse height data

The data used in the analysis are pulse height distributions measured with 2″$\phi$×2″ NaI(Tl) scintillation detectors at eight MSs in Ibaraki prefecture, Japan, during the period from 14 to 31 March, 2011. The data were provided by Ibaraki Prefectural Environmental Radiation Monitoring Center. The temporal change of dose rate observed during the period is shown in Figure 1. As shown in Figure 1, the passages of some radioactive plumes are found on 15, 16, and 20-23 March. An example of observed pulse height distributions is shown in Figure 2. It is found in Figure 2 that the pulse height distribution observed on 14 March consist only of the gamma-rays emitted by natural radionuclides ($^{40}$K, $^{214}$Pb, $^{214}$Bi, and $^{208}$Tl) permanently occurring in soil, while that on 16 March consist of the gamma-rays emitted by some anthropogenic radionuclides in addition to the natural nuclides. In this study, the pulse height distribution observed on 14 March was used as the background, and was subtracted from the analyzed pulse height data to eliminate the contribution from the natural nuclides.

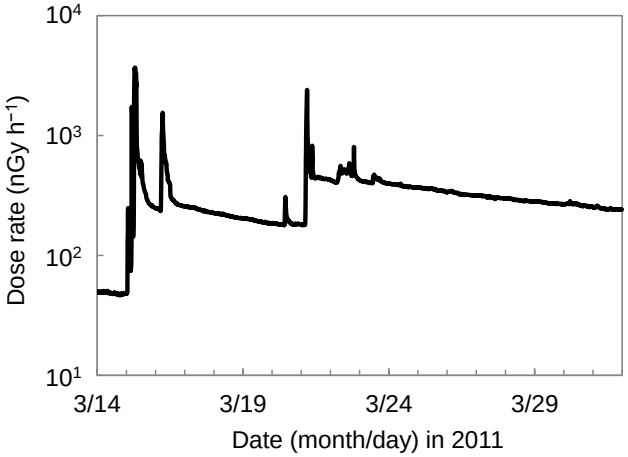


**Figure 1.** Temporal change of dose rate at the Muramatsu MS.

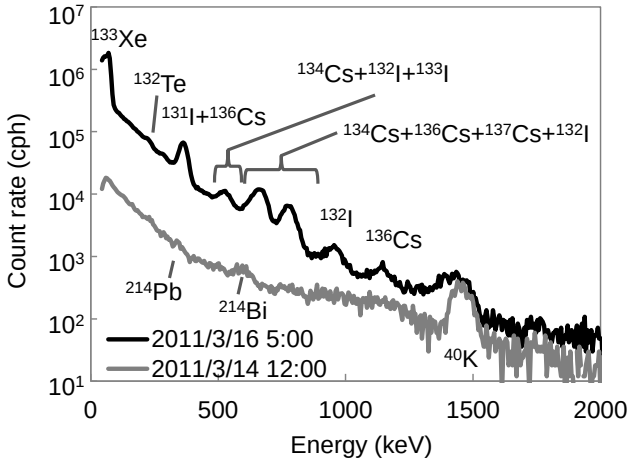


**Figure 2.** Example of observed pulse height distribution at the Muramatsu MS.

## 2.2 Calculation of pulse height distribution

According to our previous study [3], in this study, the estimation of air and surface activity concentrations was made by comparing count rates in the full-energy peak ranges between observation and calculation with an electron-photon transport. The details of the estimation method are described in the Section 2.3. Pulse height distributions of each nuclide per unit surface activity concentration were calculated with the Monte Carlo electron-photon transport code EGS5 [4]. To efficiently calculate the electron-photon transports, the technique developed by Namito *et al.* [5] was used, in which the geometries of the detector and source were exchanged. The calculation geometry consisted only of an air layer of 1 km thickness, a soil layer of 1 m thickness, and a 2″$\phi$×2″ NaI(Tl) scintillation detector, although there were buildings and/or surface undulations around MS in reality. The horizontal size of the calculation domain was 500 m × 500 m with the detector at the center, supposing a virtually infinite horizontal extent. The density of air was set to be $1.2\times10^{-3}$ g cm$^{-3}$. The soil composition and density were assumed to be pure $SiO_2$ and 1.6 g cm$^{-3}$. The detector was set at 3.5 m above the ground according to the field investigation. Pulse height distributions were calculated in the following two distributions of nuclides: Radionuclides existed only in air and were distributed uniformly in air; Radionuclides

existed only on or in the ground and the depth profile of the concentration was described by an exponential function,

$$C = C_0 \exp\left(-\frac{d}{\beta}\right) \tag{1}$$

where $d$ is depth in unit of g cm$^{-2}$, and $\beta$ is often called relaxation mass per unit area (g cm$^{-2}$).

## 2.3 Estimation of radioactivity concentration

In this study, the anthropogenic radionuclides selected for concentration estimation were $^{131}$I, $^{132}$I, $^{133}$I, $^{134}$Cs, $^{136}$Cs, $^{137}$Cs, $^{132}$Te, and $^{133}$Xe, which have high volatility, have large potential contribution to dose rate, and were detected in Ibaraki prefecture after FDNPP's accident. The main gamma-ray energies and their emission probabilities of the objective nuclides are listed in Table 1. Because there are eight nuclides for which concentrations are to be estimated, at least eight energy ranges are required. In addition, it is advantageous to select the energy ranges to which the number of contributing nuclides is as small as possible in order to reduce the estimation errors [3]. The energy ranges used in the present analyses are listed in Table 2. The width of each energy range was set to be twice the FWHM of corresponding peak.

The method of radioactivity concentration estimation is based on that described in our previous study [3]. The count rate $A_j$ in the $j$-th BIN consists of the contributions of unscattered and scattered photons from nuclides. This can be expressed as

$$A_j = \sum_i \left(\Gamma_{i,j} C_i\right) \tag{2}$$

where $C$ is the air or surface activity concentration, $\Gamma_{i,j}$ the count rate in the $j$-th BIN per unit air or surface activity concentration of nuclide $i$. $\Gamma_{i,j}$ was calculated with EGS5 described in the Section 2.2.

The air and surface activity concentrations $C$ of the objective nuclides were determined with a least-square method in which the square sum of relative differences of the count rates in each energy range between observation $A_{obs,j}$ and calculation $A_{cal,j}$,

$$\Delta = \sum_j \left(\frac{A_{cal,j} - A_{obs,j}}{A_{obs,j}}\right)^2 \tag{3}$$

was minimized. In this study, pulse height distribution averaged for ten minutes was used to estimate the air and surface activity concentrations during each 10-min period.

**Table 1.** Energies and its emission probabilities of gamma rays of the objective nuclides.

| Radionuclide | Energy in keV (emission probability in percent) |
|---|---|
| $^{131}$I | 284(6), 364(81), 637(7) |
| $^{132}$I | 506(5), 522(16), 630(13), 668(99), 670(5), 672(4), 727(5), 773(76), 812(6), 955(18), 1130(3), 1399(7) |
| $^{133}$I | 529(87) |
| $^{134}$Cs | 563(8), 569(15), 605(98), 796(85), 802(8), 1365(3) |
| $^{136}$Cs | 340(42), 819(100), 1048(80), 1235 (20) |
| $^{137}$Cs | 662(85) |
| $^{132}$Te | 228(88) |
| $^{133}$Xe | 81(38) |

**Table 2.** Energy ranges of BIN and corresponding nuclides.

| BIN No. | Energy range (keV) | Radionuclide |
|---|---|---|
| 1 | 65-95 | $^{133}$Xe |
| 2 | 210-250 | $^{132}$Te |
| 3 | 340-390 | $^{131}$I, $^{136}$Cs |
| 4 | 500-560 | $^{133}$I, $^{132}$I |
| 5 | 630-700 | $^{137}$Cs, $^{131}$I, $^{132}$I |
| 6 | 760-840 | $^{134}$Cs, $^{132}$I , $^{136}$Cs |
| 7 | 900-1000 | $^{132}$I |
| 8 | 1000-1100 | $^{136}$Cs |

### 2.4 Estimation of ratio of air to surface concentration

The comparison of pulse height distribution during the passage of a radioactive plume between observation and calculation under the condition that whole of deposited radionuclides exist on the ground ($\beta$ = 0) is shown in Figure 3. The calculated pulse height distribution was obtained by using the estimated surface activity concentrations in the EGS5 calculation. As shown in Figure 3, the calculated pulse height distribution in the full-energy peak parts is in good agreement with the observation, while in the low-energy part (< 500 keV) is evidently smaller. If part of nuclides was set to exist also in air, the count rate in the low-energy part would be calculated to be larger because of the larger number of photons scattered by air. In consequence, the calculated pulse height distribution would be in better agreement with observation.

In this study, to estimate simultaneously air and surface concentrations from pulse height distribution, the relation between the air concentration $C_{air}$ and surface one $C_{surface}$ was assumed to be a proportional relationship;

$$C_{air} = F \times C_{surface} \tag{4}$$

where $F$ was assumed to be independent of the objective nuclides except for $^{133}$Xe. This assumption indicates that the radionuclide composition of air concentration was assumed to be same as that of surface concentration except for $^{133}$Xe. Xe-133 was assumed to exist only in air because it is noble gas and does not deposit on the surface. An energy range was added to determine $F$, the width of which was set to 120-180 keV. The additional energy range consists only of scattered photons without unscattered photons. The air to surface concentration ratio $F$ was determined together with the concentrations of the objective nuclides with a least-square method described in Section 2.3, adding the energy range (120-180 keV).

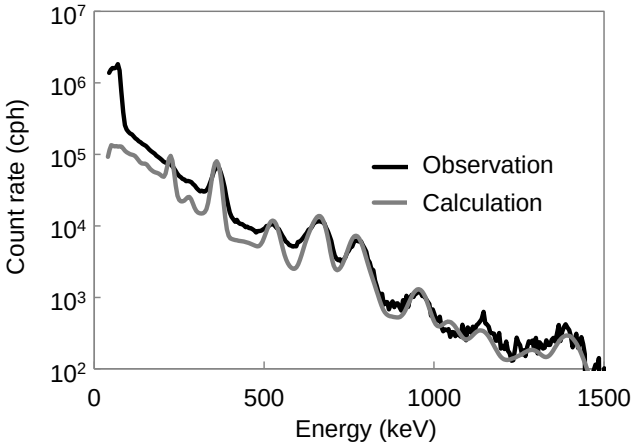


**Figure 3.** Comparison of pulse height distribution during the passage of a radioactive plume between observation and calculation under the condition that whole of deposited radionuclides exist on the ground ($\beta$ = 0) at the Muramatsu MS at 5 JST on 16 March, 2011.

## 3. Results and discussion

The temporal changes of estimated surface and air concentrations at the Muramatsu MS are shown in Figures 4 and 5, respectively. The influence of infiltration on estimated concentrations was similar among the objective MSs. The detailed discussion of temporal change of the estimated activity concentrations refers to our previous study [3]. The estimated surface concentrations with $\beta$ = 3 g cm$^{-2}$ are about three times larger than those with $\beta$ = 0 g cm$^{-2}$. The difference in estimated surface concentrations between $\beta$ = 0 and 3 g cm$^{-2}$ is smaller for nuclides emitting smaller gamma-ray energy, indicating that the radionuclide composition of the estimated surface concentrations is different depending on the relaxation mass per unit area $\beta$. The composition of the estimated surface concentrations is one of

important points to be discussed to clarify the reasonability of the values estimated with this method.

Especially, the composition of the estimated concentrations of $^{132}$Te and $^{132}$I should be discussed to clarify the reasonability of the values estimated with this method, which is largely different depending on the relaxation mass per unit area. The reason why is that the radioactive secular equilibrium between $^{132}$Te and $^{132}$I is attained within 1-day after those depositions because $^{132}$Te is the parent radionuclide of $^{132}$I and the half-life of $^{132}$Te ($T_{1/2}$ = 3.2 d) is much longer than that of $^{132}$I ($T_{1/2}$ = 2.3 h). The radioactive secular equilibrium between the estimated surface concentration of $^{132}$Te and $^{132}$I with $\beta$ = 3 g cm$^{-2}$ is found during the period from 17 to 20 March. After 22 March, the estimated surface concentration of $^{132}$Te is closer to that of $^{132}$I by considering infiltration of nuclides. These results indicate that the surface concentrations were estimated more reasonably by considering infiltration of nuclides.

During the periods without passage of radioactive plumes, the estimated air concentrations are expected to be zero. Nevertheless, the estimated air concentrations with $\beta$ = 0 g cm$^{-2}$ are not zero during these periods. On the other hand, those with $\beta$ = 3 g cm$^{-2}$ are zero during the period from 17 to 20 March, and were calculated to be more than 70% smaller than those with $\beta$ = 0 g cm$^{-2}$ after 22 March. These results indicate that the air concentrations were estimated more reasonably by considering infiltration of nuclides. The difference in the estimated air concentrations during the periods with passages of a radioactive plume between $\beta$ = 0 and 3 g cm$^{-2}$ is within 30% and is smaller than that during the other periods.

The influence of considering infiltration of nuclides on estimated air concentration is explained by comparing pulse height distribution between observation and calculation. The example of pulse height distributions during the periods without passage of radioactive plumes is shown in Figure 6. The calculated pulse height distributions were obtained under the conditions that nuclides existed only on the ground surface ($\beta$ = 0 g cm$^{-2}$) or only in the ground ($\beta$ = 3 g cm$^{-2}$). As shown in Figure 6, the calculated count rate in the low-energy part with $\beta$ = 0 g cm$^{-2}$ is about 30% smaller than the observation, while the difference in count rate between observation and calculation with $\beta$ = 3 g cm$^{-2}$ is within 5%, showing a good agreement between observation and calculation. In the case of $\beta$ = 0 g cm$^{-2}$, part of nuclides appear to exist in air to reproduce the observed pulse height distribution, resulting in the estimated air concentrations of more than 0 Bq m$^{-2}$. In the case of $\beta$ = 3 g cm$^{-2}$, on the other hand, whole of nuclides appear to exist on or in the ground because of the agreement of pulse height distribution between observation and calculation, resulting in the estimated air concentrations of 0 Bq m$^{-2}$. During the periods with passages of a radioactive plume, the fractional contribution from air concentrations to observed count rates was much larger than that from surface concentrations. Therefore, the influence of considering infiltration of nuclides on the estimated air concentrations during the periods was smaller than the other periods, and the difference in the estimated air concentration between $\beta$ of 0 and 3 g cm$^{-2}$ was within 30%.

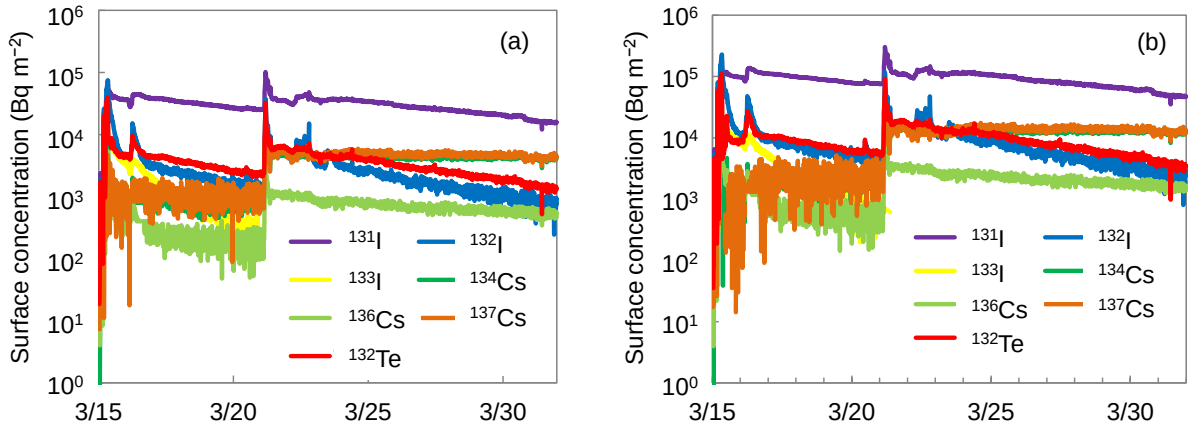


**Figure 4.** Temporal changes of estimated surface concentrations at the Muramatsu MS (a: $\beta$ = 0 g cm$^{-2}$, b: $\beta$ = 3 g cm$^{-2}$).

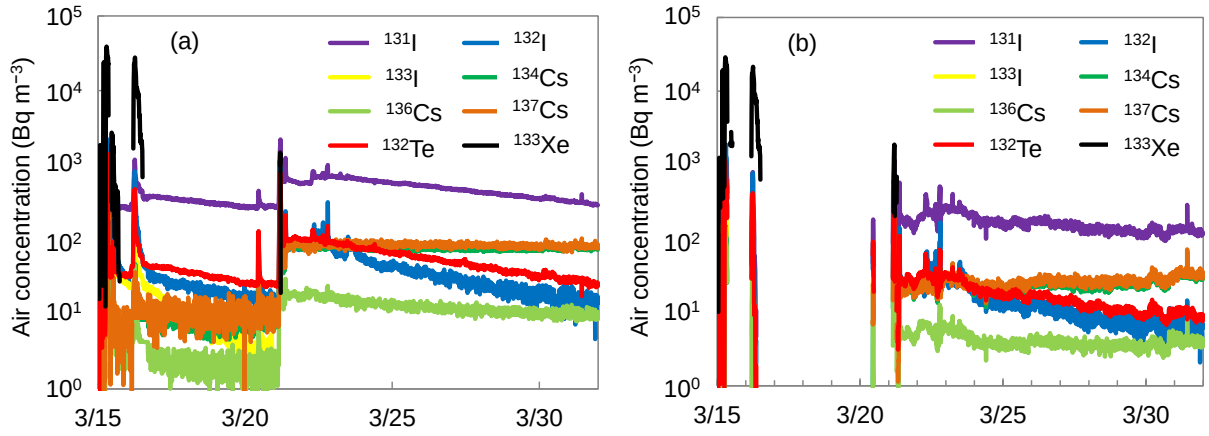


**Figure 5.** Temporal changes of estimated air concentrations at the Muramatsu MS (a: $\beta$ = 0 g cm$^{-2}$, b: $\beta$ = 3 g cm$^{-2}$).

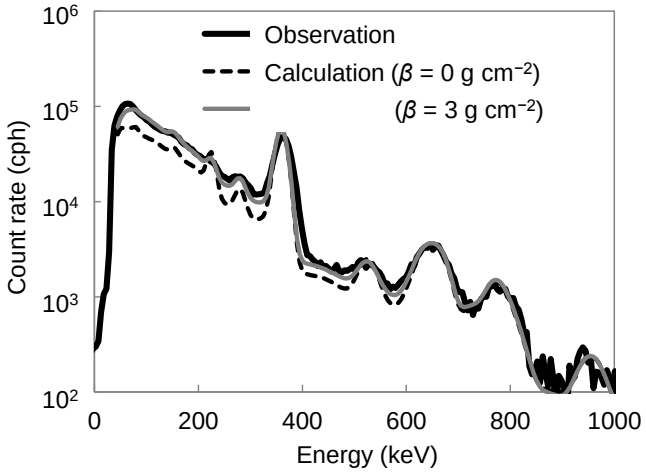


**Figure 6.** Comparison of pulse height distribution on 18 March between observation and calculation. The calculations of pulse height distribution were made under the condition that nuclides existed only on the ground surface ($\beta$ = 0 g cm$^{-2}$) and only in the ground ($\beta$ = 3 g cm$^{-2}$).

## 4. Conclusions

The influence of considering infiltration of nuclides on air and surface radioactivity concentrations estimated simultaneously from NaI(Tl) pulse height distribution was discussed. Considering infiltration of nuclides, the estimated surface concentrations were about three times larger. In addition, the estimated surface concentrations of $^{132}$Te and $^{132}$I were closer to each other, and the radioactive secular equilibrium between $^{132}$Te and $^{132}$I was found. The estimated air concentrations during the period without passage of radioactive plumes were closer to 0 Bq m$^{-2}$ by considering infiltration of nuclides, while those during the period with passages was slightly changed. These results indicate that the air and surface radioactivity concentrations were estimated more reasonably by considering infiltration of nuclides.

## Acknowledgments

The authors would like to thank the Ibaraki Prefectural Environmental Radiation Monitoring Center for its providing with the pulse height distribution, and supporting the land survey around the MSs. This work was supported by JSPS KAKENHI [Grant Number 24110002].

## References


1) H. Hirayama, T. Sanami, and Y. Namito, "Study of gamma ray spectrum at height of 1 m from radionuclide widely distributed on soil surface using egs5 monte carlo code," Trans. At. Energy Soc. Jpn. **12**(3), 222-230 (2013). [in Japanese].
2) S. Minato, "Application of a 60 × 60 response matrix for a NaI(Tl) scintillator to fallout from the Fukushima reactor accident," Radiat. Emergency Med. **1**(1-2), 108-112 (2012).
3) J. Hirouchi, H. Yamazawa, S. Hirao, and J. Moriizumi, "Estimation of surface anthropogenic radioactivity concentrations from NaI(Tl) pulse height distribution observed at monitoring station," Radiat. Prot. Dosim. (accepted)
4) H. Hirayama, Y. Namito, A. F. Bielajew, S. J. Wilderman, and W. R. Nelson, "The EGS5 Code System," KEK Report 2005-8, SLAC-R-730, High Energy Accelerator Reserch Organization (KEK), Stanford Linear Accelerator Center (SLAC) (2005).
5) Y. Namito, H. Nakamura, A. Toyoda, K. Iijima, H. Iwase, S. Ban, and H. Hirayama, "Transformation of a system consisting of plane isotropic source and unit sphere detector into a system consisting of point isotropic source and plane detector in Monte Carlo calculation," J. Nucl. Sci. Technol. **49**, 167-172 (2012).

# Analytical method for distribution of natural radionuclides after the FDNPP accident by aerial monitoring

**Y. Nishizawa[1], T. Sugita[2], Y. Sanada[1], T. Torii[1]**

*[1]Sector of Fukushima Research and Development, Japan Atomic Energy Agency, 2-2-2, Uchisaiwai-cho, Chiyoda-ku, Tokyo, 100, 8577, Japan*
*[2]Science System Laboratory Co. Ltd, 1342-6 Sumiyoshi, Kasama-shi, Ibaraki, 309-1716, Japan*
*[3]Corresponding author. e-mail: nishizawa.yukiyasu@jaea.go.jp*

**Abstract**

For a precise assessment of the distribution of radioactive cesium dispersed over a wide area, one must accurately evaluate the background radiation due to natural radionuclides. We have developed a new method that accurately evaluates the spatial distribution of the background radiation in areas contaminated by radioactive cesium. Using the data from aerial monitoring, we analyzed such distribution while excluding the effect of radioactive cesium. This method made it possible to evaluate not only the precipitation of radioactive cesium with quite well accuracy, but also the spatial distribution of the natural radionuclides all over Japan.

## 1. Introduction

Since 2011, MEXT (Ministry of Education, Culture, Sports, Science and Technology, Japan) have been conducting aerial monitoring to investigate the distribution of radioactive cesium dispersed into the atmosphere after the accident at the Fukushima Dai-ichi Nuclear Power Plant (FDNPP), Tokyo Electric Power Company.[1)] Distribution maps of the air dose rate 1 m above the ground and the concentration of deposited radioactive cesium on the ground are prepared using spectrum obtained by aerial monitoring. The radioactive cesium deposition is derived from its dose rate, which is calculated by excluding the dose rate of the background radiation due to natural radionuclides from the air dose-rate 1 m above the ground. The first step of the current method of calculating the dose rate due to natural radionuclides is calculate the ratio of the total count rate of areas where no radioactive cesium is detected and the count rate of regions with energy levels of 1,400 keV or higher (BG-Index). Next, calculate the air dose rate of radioactive cesium by multiplying the BG-Index and the integrated count rate of 1,400 keV or higher for the area where the radioactive cesium is distributed. In high dose-rate areas, however, the count rate of the 1,365-keV peak of $^{134}$Cs, though small, is included in the integrated count rate of 1,400 keV or higher, which could cause an overestimation of the air dose rate of natural radionuclides.

We developed a method for accurately evaluating the distribution maps of natural radiation dose rate by excluding the effect of radioactive cesium, even in contaminated areas. The natural radiation dose distribution throughout Japan has been measured by a variety of methods, which are used to measure the external radiation dose.[2)-4)] However, data obtained by these measurements are ‘‘spot’’ dose rate. To obtain ‘‘area’’ maps flights are at equal intervals to cover an area, including areas on the ground where access is difficult. This study reports on the natural radiation dose throughout Japan, using data with nearly uniform weighting and extremely high density.

## 2. Method for Evaluating Natural Radiation Dose Distribution

Aerial monitoring is carried out with a large NaI scintillation detector mounted on a helicopter that flies over the study area with a line spacing of 0.6-5-km (Fig. 1) and at a standard altitude of 300 m. From April 2011, when the monitoring started, until fiscal year 2013, eight series of measurements were taken within an 80-km radius from the FDNPP, four times in regions ranging from Iwate Prefecture to Ibaraki Prefecture, and once in the other prefectures.

The MMGC (man-made gross count) method, developed by the US Department of Energy,[5] is used to calculate the dose of natural radiation ($D_{nr}$), as seen in Eq. (1), where the parameter $Cs_{1400}$ is added to exclude the integrated count rate applied to the 1,400-keV or higher energy level of $^{134}Cs$:

$$D_{\mathrm{nr}} = (C_{1400} - \mathrm{BG}_{1400} - \mathrm{Cs}_{1400}) \times \mathrm{BGindex} \times \mathrm{HF}_{1400}/\mathrm{CD} \quad (1)$$

where $C_{1400}$ is the integrated count rate (cps) for 1,400-2,800 keV; $BG_{1400}$ is the integrated count rate (cps) for 1,400-2,800 keV ascribed to background cosmic radiation, radiation from peripheral equipment, and radon decay; BG-index is the BG-Index (i.e., the ratio of the total count rate for regions with no radioactive cesium precipitation and the integrated count rate for 1,400-2,800 keV); $HF_{1400}$ is the altitude correction coefficient for the integrated count rate for 1,400-2,800 keV; and CD is the dose rate conversion factor [cps/(μSv·h$^{-1}$)].

The Gaussian fitting method,[6] which assumes that the total absorption peak of gamma-rays of the scintillation detector has a Gaussian distribution, as seen in Fig. 2, was used to discriminate radioactive cesium. Complex peaks formed by 1,365 keV of $^{134}Cs$ and 1,461 keV of $^{40}K$ are expressed by Eq. (2), which assumes two Gaussian distributions:

$$S(i,j) = a + bE + c_i e^{-(E-E_i)^2/2\sigma_i{}^2} + c_j e^{-(E-E_j)^2/2\sigma_j{}^2} \quad (2)$$

where $E$ is gamma-ray energy (keV), $E_i$ is peak energy (keV), $\sigma^2$ is the peak variance (keV), $a + bE$ is the baseline, $c$ is the net peak count rate, and $i$ and $j$ are radionuclides of the complex peak. It was assumed that the average peak energy and peak variance remained constant during the flights so they were determined in advance using average data of the flihgt.[7] The pseudo-inverse was used to obtain $a$, $b$, $c_i$, and $c_j$ for every second and to calculate $Cs_{1400}$ using the contribution ratio of the energy level of 1,400 keV or higher where 1,365 keV $^{134}Cs$ is included in.

To set a low detection limit, the average velocity of the helicopter at 21 points was calculated for the integrated count rate of Eq. (1). Since the average velocity of the helicopter was about 50 m/s, the spatial resolution was 1 km. The natural radiation dose in regions where deposited radioactive cesium from the FDNPP might be detected was calculated using this method, while data for the air radiation dose rate 1 m above ground, obtained from an aircraft investigation of the radionuclide distribution for an environmental survey of the area around the FDNPP,[1] was used for other regions.

## 3. Distribution of Natural Radiation throughout Japan

The distribution of natural radiation, excluding the radiation from radioactive cesium, in the area around the FDNPP is shown in Fig. 3 (left panel), and the ratio of the dose rate of the excluded radioactive cesium to the dose rate of natural radiation is shown in Fig. 3 (right). The distribution of the excluded radioactive cesium trended in a northwesterly direction from the FDNPP, but the distribution of the natural radiation did not follow that trend. Fig. 4 compares the air dose-rate of the natural radiation acquired by *in situ* measurements using a germanium semiconductor detector with that obtained by the aerial monitoring in the Fukushima Prefecture. The ambient dose equivalent was converted to 0.82 of the air dose rate.[8] While there were some differences, the results corresponded well with those of measurements taken on the ground. Thus, we confirmed that radioactive cesium can be properly discriminated by the functional application method with two Gaussian distributions.

The left of Fig. 5 shows the results of a survey of the natural radiation distribution across Japan. The areas with relatively high air dose rate are affected by geology that contains high amounts of natural radionuclides, such as minerals like granite. The right of Fig. 5 is a geological survey map[9] color-coded to show areas of high radiation.[1] A comparison

of the left and right panels reveals similar distributions of natural and high radiation seen in the eastern part of Fukushima Prefecture and the eastern part of Niigata Prefecture, as well as in the western part of Saitama Prefecture and the western part of Nagano Prefecture. Therefore, we have considered that the radiation distribution in Japan can be evaluated as the distribution of natural radionuclides.

## 4. Discussion

The use of the functional application method, with the assumption of the presence of two Gaussian distributions, made it possible to discriminate the complex peaks of $^{134}$Cs and $^{40}$K and thereby evaluate the distribution of natural radiation, excluding radioactive cesium. One benefit of our functional application method is that the addition of a Gaussian distribution term to the equation makes it possible to discriminate two or more complex peaks. Another benefit is that the calculation can be done quickly since a pseudo-inverse method is used to evaluate the count rate of the peak areas. These two characteristics make it possible to discriminate radionuclides quickly at multiple locations. Thus, the functional application method is considered an effective means for determining the distribution of contamination immediately after an accident.

The ratio of the dose rate of natural radiation to the dose rate ascribed to the excluded radioactive cesium for our purpose had a maximum value of ~0.4. The monitoring of high dose-rate areas conducted in fiscal year 2013 showed radiation levels of tens of μSv/h or more,[10] indicating that deposited radioactive cesium had only a slight effect but the effect of natural radiation was significant. The data for the 80-km–radius area from the FDNPP were derived from measurements taken in November 2013, which was more than 2 years after the nuclear accident. Because of radioactive disintegration, the concentration of $^{134}$Cs was less than half the value measured immediately after the accident. Since the concentration of $^{134}$Cs was high immediately after the accident, the apparent intensity of the natural radiation was probably overestimated. The functional application method presented here excludes the effect of $^{134}$Cs, making it possible to evaluate the intensity of the natural radiation with quite well accuracy.

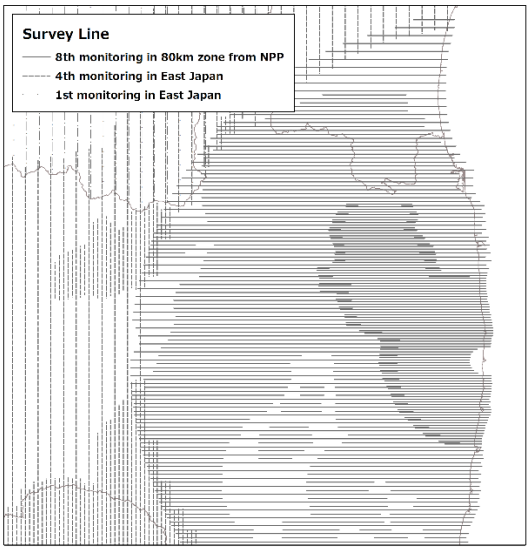


**Fig. 1.** Transverse line pattern of aerial monitoring.

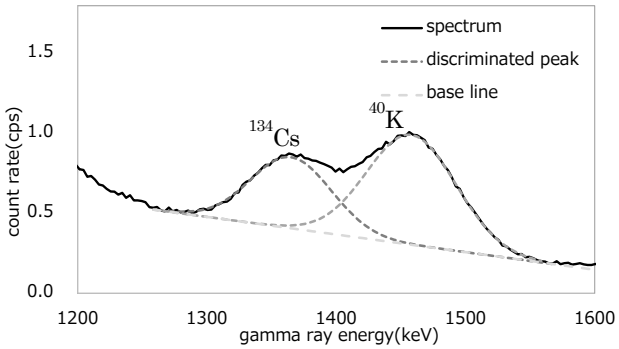


**Fig. 2.** Discrimination of the peaks of $^{134}$Cs and $^{40}$K using the functional application method.

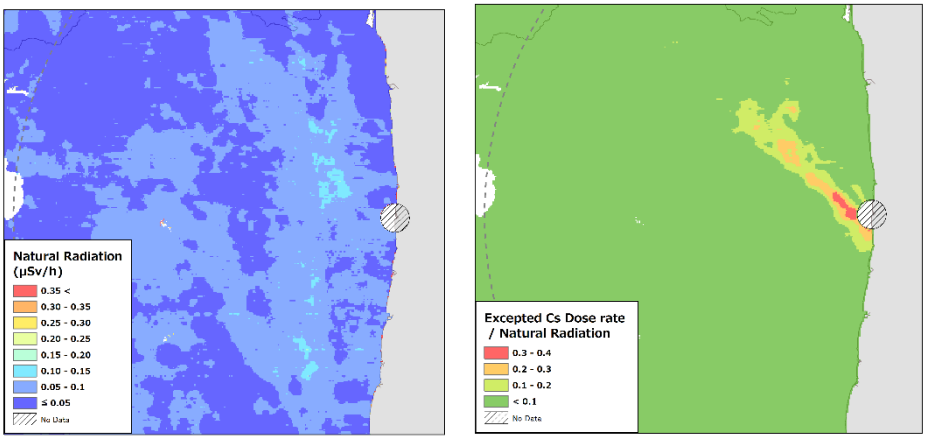


**Fig. 3.** (Left) Distribution of natural radiation near the FDNPP. (Right) Distribution of the ratio of the dose rate of natural radiation to the dose rate ascribed to excluded radioactive cesium around the FDNPP.

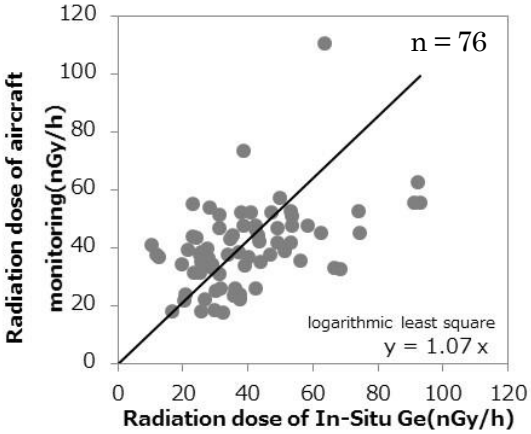


**Fig. 4.** Comparison of the dose rate of natural radiation obtained by aerial monitoring and that obtained on the ground by a germanium semiconductor detector.

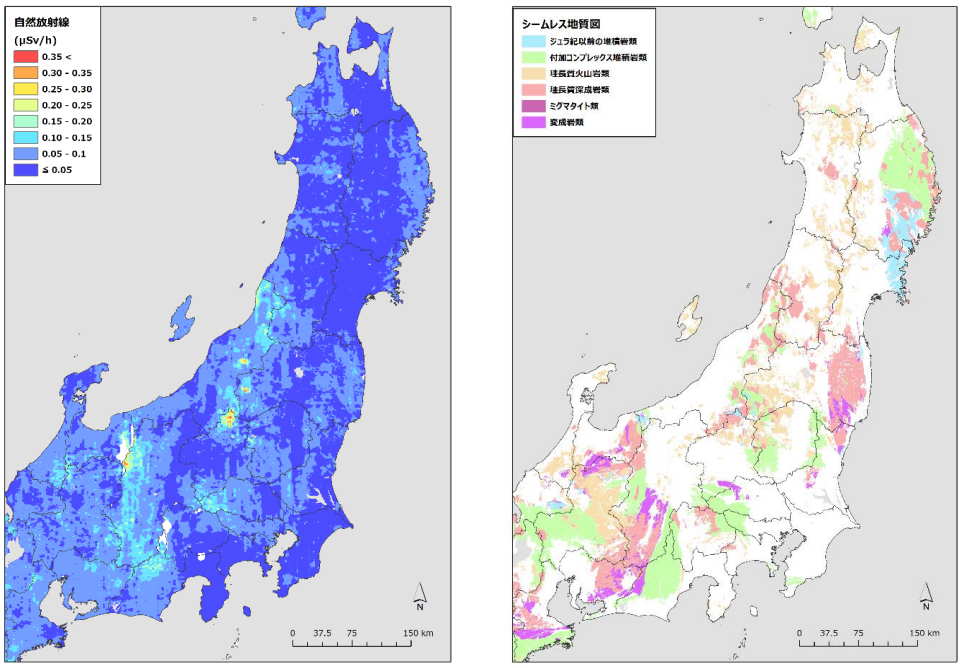


**Fig. 5.** (Left) Distribution of natural radiation. (Right) Geological map with a color code showing the geology containing a high level of radioactive substances (data from the Seamless Geological Map of Japan).

## References


1) T. Torii, Y. Sanada, et al., Radioactive Substance Distribution Status Survey Using Aircraft for Wide Area Environmental Monitoring, JAEA-Technology, 2012-036.
2) M. Shita, T. Sanada, K. Fujitaka, S. Minato, Dosage of Natural Radiation in Japan. Isotope News No. 706 (February 2013).
3) M. Furukawa, Natural Radiation Level of Japan Islands. J. Geogr. **102**, 868–877 (1993).
4) N. Imai, Natural Radiation Dose in Japan, the Geological Society of Japan, http://www.geosociety.jp/hazard/content0058.html, as viewed on August 25, 2014.
5) T. Hendricks, S. Riedhauser, An serial radiological survey of the Nevada test site, DOE/NV/11718-324, 1999.
6) Ministry of Education, Culture, Sports, Science and Technology, Gamma-ray Spectrometry Using Germanium Semiconductor Detector. (1992)
7) T. Torii, T. Sugita, C. E. Okada, M. S. Reed, D. J. Blumenthal, Enhanced Analysis Methods to Derive the Spatial Distribution of 131I Deposition on the Ground by Airborne Surveys at an Early Stage after the Fukushima Daiichi Nuclear Power Plant Accident. Health Phys. **105**, 192–200 (2013).
8) S. Moriuchi, M. Tsutsumi, K. Saito, Evaluation on Conversion Factors to Estimate Effective Dose Equivalent from Absorbed Dose in Air for Natural Gamma Radiations. Jpn. J. Health Phys. **25**, 121–128 (1990).
9) National Institute of Advanced Industrial Science and Technology, Seamless Geological Map of Japan, 1:200,000 scale, DVD version (2009).
10) Y. Sanada, Y. Nishizawa, et al., FY2013 Aerial Monitoring in Environs of Fukushima Dai-ichi Nuclear Power Plant (Consigned Study), JAEA-Technology, 2014-012.
11) H. Hirayama, Y. Namito, A. F. Bielajew, S. J. Wilderman, W. R. Nelson, The EGS5 Code System, SLAC Report 730 and KEK Report 2005-8 (2005), available at http://www.slac.stanford.edu/cgi-wrap/getdoc/slac-r-730.pdf.
12) Y. Namito, H. Nakamura, A. Toyoda, K. Iijima, H. Iwase, S. Ban, H. Hirayama, Transformation of a system consisting of plane isotropic source and unit sphere detector into a system consisting of point isotropic source and plane detector in Monte Carlo radiation transport calculation. J. Nucl. Sci. Technol. **49**, 167–172 (2012).

**Appendix 1: Consistency with Past Monitoring Results**

Data from the latest aerial monitoring was used to prepare the natural radiation distribution, but because the intensity of natural radiation does not fluctuate much throughout the year, the distribution should be the same as that prepared from past monitoring data. The natural radiation distribution prepared using data from the past three monitoring sessions (6th-8th) conducted within the 80-km-radius area from the FDNPP were compared. The natural radiation distributions from the 7th and 8th monitoring series are compared in Fig. A-1. Differences in the distribution between sessions were within 30% for most of the area measured. Fig. A-2 shows that there is good correlation among the three sessions, although the intensity of the distribution from the 6th monitoring session was slightly low. This confirmed that regardless which monitoring data were used to prepare the natural radiation distribution, we were able to obtain similar distributions.

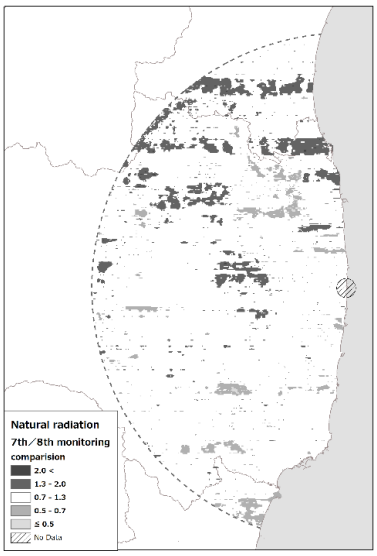


**Fig. A-1.** Comparison of natural radiation distribution from the 7th and 8th monitoring series within 80-km-radius area from FDNPP.

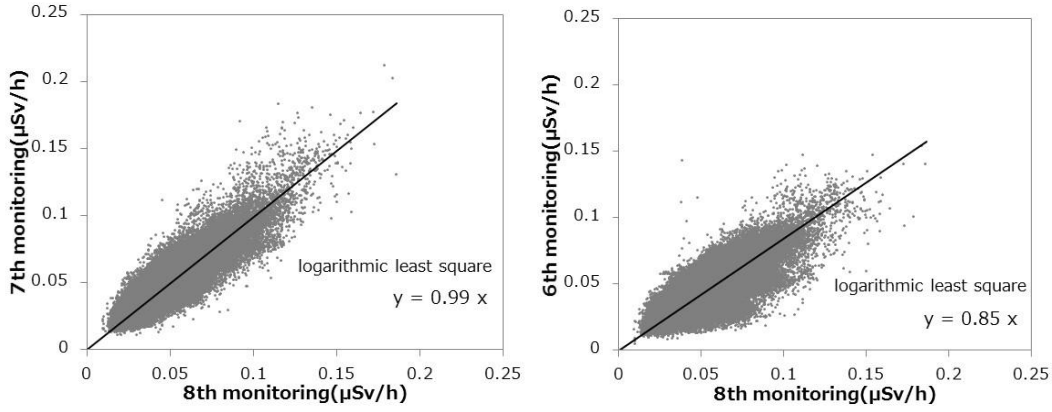


**Fig. A-2.** Effect of natural radiation distribution prepared from data of past monitoring sessions. (Left) Comparison of the 7th and 8th series. (Right) Comparison of the 6th and 8th series.

**Appendix 2: Effects of Fluctuation in the Concentration Ratio of Natural radionuclides on Evaluation of Natural Radiation**

The BG-Index (correction coefficient for deriving the total count rate of natural radiation from the integrated count rate of 1,400 keV or higher), defined by the evaluation equation for natural radiation, was considered a uniform value derived from the combination of data from the aerial monitoring by helicopter and the ground detector, as it was thought to be dependent on the gamma-ray shield by the helicopter and energy characteristics of the detector. Since the principal natural radionuclides such as the $^{40}$K, $^{238}$U, and $^{232}$Th series may have different values for the ratio (BG-Index) of the integrated count rate of 1,400 keV or higher to the total count rate for each isotope, we examined the potential need to change the BG-Index depending on the concentration ratio of natural radionuclides that varies from one area to another.

To investigate the relationship between the concentration ratio and the BG-Index of natural radionuclides, we looked into the distribution of the BG-Index with respect to measured area based on the relationship between the peak areas for each isotope obtained from the spectral data from our measurements, the peak area for each isotope, and the BG-Index. The count rate for the peak area of $^{40}$K was calculated using Eq. (2), while the count rate for the $^{238}$U series and the $^{232}$Th series were calculated using an equation with the Gaussian distribution put into a single term. The relationship between the peak area for each isotope and the BG-Index was calculated next using the electron and photon transport Electromagnetic Cascade Monte Carlo Code EGS5[11] to obtain the spectrum measured by the detector at an altitude of 300 m when the naturally occurring radioactive isotope was distributed uniformly in the ground. To improve the efficacy of the calculation, the calculation of the radiation flux near the detector and the calculation of the irradiation at the detector by using pre-calculation result as the radiation source were performed separately. The method for replacing the radiation source and the detector's surface was also used in the former case (see conceptual diagram in Fig. A-3).[12] The aluminum 7075A (3 cm), which is often used in the framework and exterior walls of helicopters, was installed below the detector to simulate measuring inside a helicopter to calculate radiation at the detector. The integration spectrum, derived from actual measurements over areas where there was no deposited radioactive cesium, was compared with the spectrum from the simulated system; the shapes of the spectra were similar, as seen in Fig. A-4, confirming the validity of the calculation system. These spectral data were used to calculate the ratio of the count rate of the peak area and the BG-Index for each isotope and multiplied the ratio by the count rate of the peak areas obtained from the actual measurements to arrive at the distribution of the BG-Index. The BG-Index obtained from aerial monitoring (8th monitoring series in Fukushima Prefecture and 4th series in eastern Japan) conducted in fiscal year 2013 had relatively small deviations, e.g., 6 and 7%, as shown in Table A-1. Since the effect of the fluctuation in the concentration ratio of natural radionuclides on the evaluation of natural radiation is small, the error caused by setting the BG-Index as a uniform value, combining the helicopter and the detector measurements, is considered small.

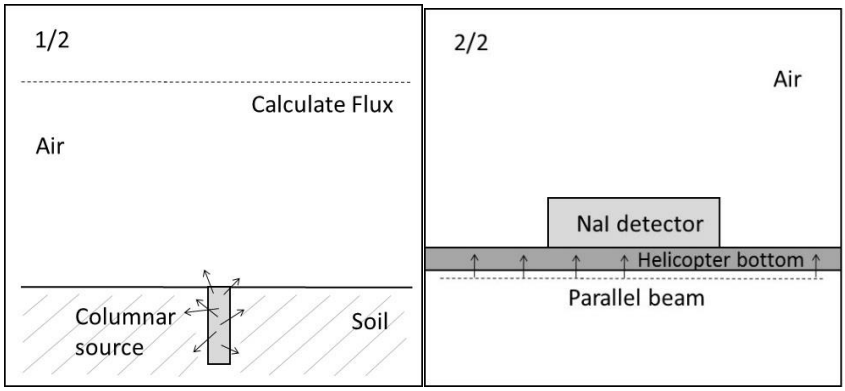


**Fig. A-3.** Calculation geometry. Step 1: calculate the flux of isotropic γ radiation from natural radionuclides near the detector. Step 2: calculate the spectrum of the detector when the result of the calculation from Step 1 is irradiated as a parallel beam.

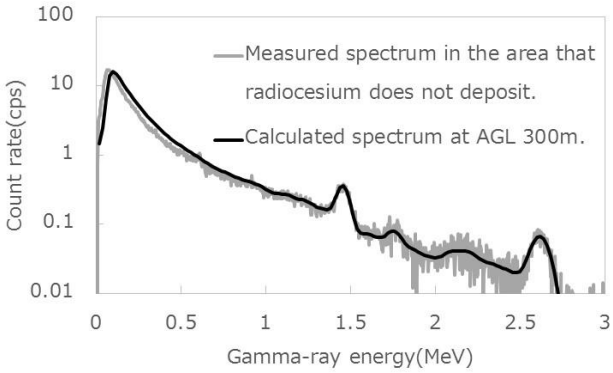


**Fig. A-4.** Comparison of the spectrum derived from measurements taken in areas where there was no deposited radioactive cesium and the spectrum calculated using a simulation system.

**Table A-1.** Distribution of BG-Index from monitoring Fukushima Prefecture and neighboring prefectures.

| Monitoring | System* | Average BG-Index | Relative deviation (%) |
|---|---|---|---|
| Fourth series of East Japan | System A | 42.1 | ±6.4 |
| | System B | 40.8 | ±7.2 |
| | System D | 40.6 | ±7.0 |
| Eighth series of Fukushima Prefecture | System A | 40.7 | ±7.0 |
| | System D | 41.1 | ±6.4 |

*The system is a combination of helicopter and detector

**Appendix 3: Comparison of Air Dose Rate at 1 m Above the Ground**

Aerial monitoring was also used to take measurements in areas that were sufficiently distant from the FDNPP and where no deposited radioactive cesium was found, and maps of the air dose rate at 1 m above the ground were prepared. Since the air dose rate at 1 m above the ground measured in areas without deposited radioactive cesium are ascribed to natural radionuclides, they were compared with the natural radiation distribution obtained by our method to check the validity of the natural radiation distribution. Aichi Prefecture was used for this comparison. The air dose rate at 1 m above the ground was calculated using the integrated count rate of the total energy. The frequency distribution of the ratio of the air dose rate at 1 m above the ground with respect to the natural radiation is shown in Fig. A-5. The average value of the distribution was close to 1 and the standard deviation was also small enough. This confirmed that the prepared natural radiation distribution was sufficiently accurate.

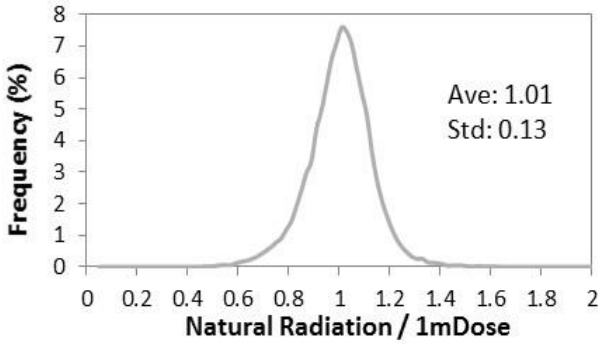


**Fig. A-5.** Frequency distribution of the ratio between natural radiation at areas where no deposited radioactive cesium was found and air dose rate at 1 m above the ground.